Chapter 4

Tracking System Performance

In order to extract results from the observed data it is essential to accurately model the detector in the Monte Carlo, which requires that the performance of the detector elements be well understood. Of particular concern for the subsequent analyses is the tracking detector system, namely the CDC, DCVD and SSVD. This chapter contains a study of the performance of the combination of the three tracking detectors. The performance of the detectors individually was discussed in Chapter 2.

The tracking system characteristics of primary importance in the following analyses are the

- impact parameter resolution, and
- track finding and reconstruction efficiency,

both of which are addressed in this chapter. The impact parameter resolution is of primary importance for determining the efficiency and purity of the enrichment method used for selecting $Z^0 \to b\bar{b}$ events. This method, the impact parameter significance tag, is discussed in Chapter 5 and its application to measure the hadronic branching fraction of the Z^0 to $b\bar{b}$ events in Chapter 6. The tracking efficiency is also important, particularly for the multiplicity measurements described in Chapter 7.

4.1 An Introduction to Track Impact Parameter

The *impact parameter* of a track is the distance of closest approach to some reference point, namely the distance perpendicular from a track's trajectory. In this case the reference point is the interaction point (IP) where the e^- and e^+ beams nominally collide.

4.1.1 Impact Parameter Definition

If a particle created at the IP lives for a time t, its decay length is then given by $l = \gamma\beta ct$, where $\beta = v/c$ (the particle's speed relative to the speed of light) and $\gamma = E/mc^2$ (the particle's energy divided by its mass). If this particle decays, then the impact parameter of the daughter with respect to the IP, as projected into the plane perpendicular to the beam axis (the xy plane), is given by

$$b = l\sin\psi\sin\phi = \gamma\beta ct\sin\psi\sin\phi. \quad (4\text{-}1)$$

In this equation, ϕ is the polar angle from the beam axis and ψ is the angle of the daughter direction with respect to that of the parent, as illustrated in Figure 4–1. Because the tracking detectors have primarily axial segmentation, in subsequent usage the terms 'impact parameter' (b) and 'decay length' (l) will refer to the projection of the three-dimensional lengths into the plane perpendicular to the beam axis.

An interesting feature of the impact parameter is that as the parent particle becomes highly relativistic, the impact parameter becomes insensitive to the parent particle's momentum. This is seen as the cancellation between the decay length,

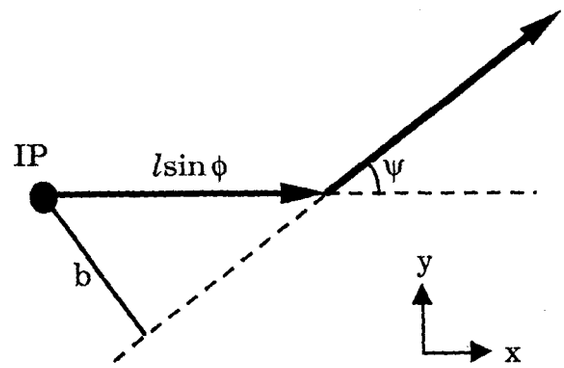

Figure 4–1 Definition of the variables involved in calculating impact parameters. The parent particle traveled a distance l and then decayed into a daughter which travels at an angle ψ from the parent's direction.

which increases with higher momentum, and the decay angle, which decreases with higher momentum. To illustrate this in the limit that the daughter particle's mass is small compared to its momentum in the parent's center-of-mass (CM) frame, consider a track which decays at an angle ψ_{cm} in the parent particle's CM frame. In the frame in which we observe the daughter particle, this corresponds to the angle ψ, given by

$$\sin\psi = \frac{\sin\psi_{cm}}{\gamma(1+\beta\cos\psi_{cm})} \; ; \; 0 < \psi_{cm} < \pi. \; ^{*} \tag{4-2}$$

This relation is a consequence of the fact that the daughter's momentum parallel to the parent's will be Lorentz boosted, whereas the transverse momentum is Lorentz invariant. Inserting this into the expression for b in Equation (4-1), the γ terms cancel, yielding

$$b \approx \frac{\beta ct \sin\phi \sin\psi_{cm}}{(1+\beta\cos\psi_{cm})} \approx c\beta t \sin\phi \tan\tfrac{1}{2}\psi_{cm} \; ; \; 0 < \psi_{cm} < \frac{\pi}{2}, \tag{4-3}$$

where the last expression is a further approximation assuming that $\beta \approx 1$ in the denominator.

The level to which the impact parameters of daughter tracks from B decays are insensitive to the B momentum at the Z^0 resonance can be seen in Figure 4–2. This figure shows, as a function of B hadron momentum, the average impact parameter divided by the proper decay length, $c\tau$, of the B hadron for all charged tracks from B decay. Also shown is the expected spectrum of B hadron momenta. Both of these were calculated by the LUND Monte Carlo at E_{cm} = 91 GeV.[†] From this example, one can see that at such high center-of-mass energy, the impact parameter of the daughter track is indeed only sensitive to the parent B hadron momentum for those tracks from the decay of the B's which received very little energy during the fragmentation process. Furthermore, because the fragmentation to B hadrons is quite hard, the number of tracks from these low momentum B hadrons is small. For example, only 23% of the tracks are from a B hadron of a momentum for which $\langle b/c\tau \rangle$ is below 0.9 of is high B momentum plateau.

* Equation (4-2) has been frequently noted without reference to the $p_{daughter} \gg m_{daughter}$ limit in the parent's rest frame. This may be a result of the fact that this has often been mentioned in the context of tagging leptons from B decay. In this case, a massless approximation is clearly valid for electrons due to their small mass, while the momentum spectrum, which will be harder for both muons or electrons than for hadrons from B decay, will further justify the equation's validity in semi-leptonic decays.

† See Chapter 3 for more information on the Monte Carlo used in this analysis.

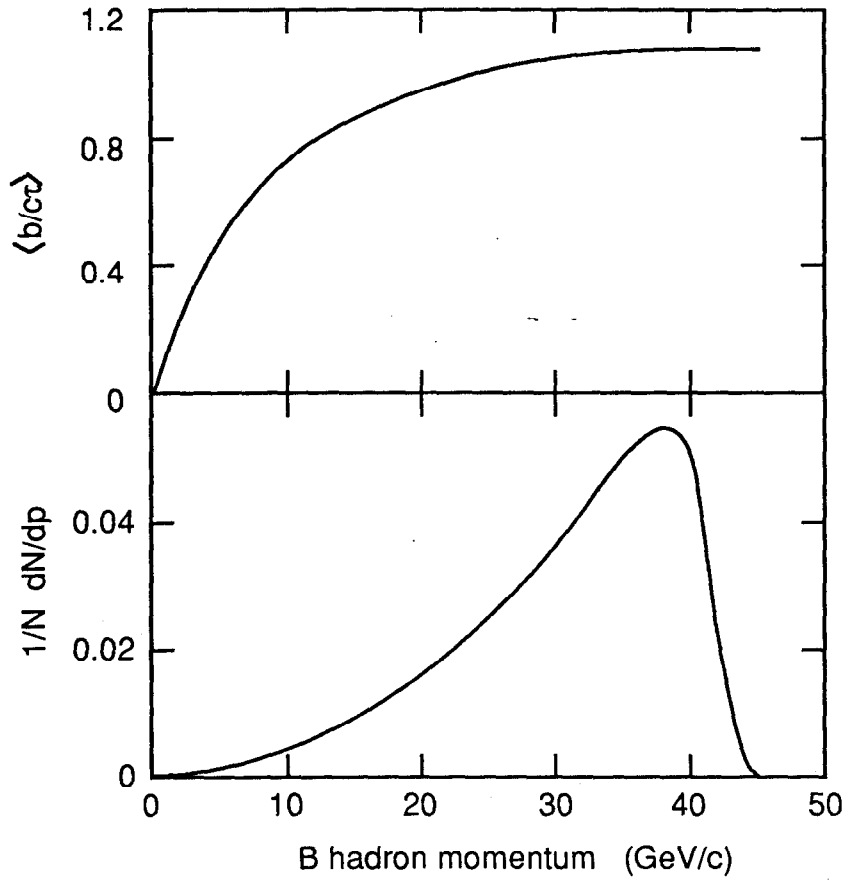

Figure 4–2 In the upper plot, the average of the impact parameter divided by the lifetime of the B hadron is shown as a function of the momentum of the B hadron. Below is the expected spectrum of B hadron momentum.

4.1.2 Impact Parameter Signing

Impact parameters can be made more useful if they are given an algebraic sign based upon the apparent origin of the track, particularly for heavy quark events. The sign applied will be negative if the track appears to come from behind the interaction point and positive otherwise. This definition is referred to as the *physically-signed impact parameter.* This method of applying an algebraic sign is useful because all of the B decay products are swept forward by the B's large boost into the hemisphere defined by the B direction for B hadrons with a momentum of at least 8 GeV/c. Because a majority of hadronic events have a general back-to-back jet nature, the first step is to determine the axis of the event, which approximates the direction of the original partons, as given by a event or jet axis. Since the event

axis is a good approximation for the B direction, the majority of the tracks from B decay will be given the same algebraic sign.

4.1.2.1 Event and Jet Axis Algorithms

The *thrust axis* is defined as the unit vector $\hat{T}$ which maximizes the thrust, T, defined as

$$T = \max\left(\frac{\sum_i \vec{p}_i \cdot \hat{T}}{\sum_j |\vec{p}_j|}\right), \tag{4-4}$$

where the sum of the momenta $\vec{p}_i$ is taken over all of the charged tracks. The value of the thrust varies from 0.5 in the case of a very isotropic event to 1.0 for an event with narrow back-to-back jets. A nice feature of the thrust axis is that because it depends linearly on momentum, it is *infrared safe*.[106] This means that the thrust will be unchanged if one particle decays into two collinear particles. This thrust axis can then be used to divide the event into two *thrust hemispheres* defined by the plane perpendicular to the thrust axis. In heavy quark events, the thrust axis approximates the direction of the heavy hadrons in the majority of the events. The angular difference between the thrust axis and the direction of the B hadrons is shown in Figure 4–3 as determined by the LUND Monte Carlo. It is seen that the thrust axis does reasonably approximate the actual B direction in most cases although there are broad tails. The source of these tails is primarily events in which either one or both of the B hadrons has fairly little energy, such as the case when a hard gluon has been radiated. This produces multi-jet events in which the B hadron momenta are not back-to-back and thus the thrust axis cannot accurately reconstruct the directions of both B hadrons.

The use of other event axes was also studied. In particular these were the sphericity axis and jet axes using two different algorithms: a scaled invariant mass algorithm[101] and a momentum cluster algorithm[107]. The sphericity axis unit vector $\hat{S}$ is defined by

$$S = \frac{3}{2}\min\left(\frac{\sum_i |\vec{p}_i \times \hat{S}|^2}{\sum_j |\vec{p}_j|^2}\right) \tag{4-5}$$

and, as it depends on the square of the momentum, will be more strongly affected by high momentum tracks. The value of the sphericity, S, will range from 0 for

narrow 2-jet events to 1 for events with an isotropic distribution of tracks. Unlike the thrust axis, it's quadratic dependence on the momentum means that it is not co-linear safe. Despite these differences, the sphericity axis yielded results which are virtually the same as those for the thrust axis.

The cluster algorithm YCLUS starts with each of the particles being considered to be a jet and then combines these, beginning with the pairs that will yield the smallest value of the parameter $y \equiv m_{ij}/E_{vis}$, the ratio of the invariant mass to the total visible energy. This process continues until all pairs have y larger than some value y_{cut} which typically ranges from 0.02 to 0.10. The LCLUS algorithm similarly begins with each particle being considered its own jet. It then combines these beginning with that pair with the smallest value of

$$D = \sqrt{\frac{2|p_i|^2|p_j|^2(1-\cos\theta_{ij})}{(|p_i|+|p_j|)^2}}, \tag{4-6}$$

until all of the jets are above a cut-off, D_{join}. This cut-off was tuned at E_{cm} = 30 GeV to be 2.5 GeV, and scales to a value of 7.9 GeV at 91 GeV.[62] Both of the jet algorithms more accurately reconstructed the B hadron direction than did

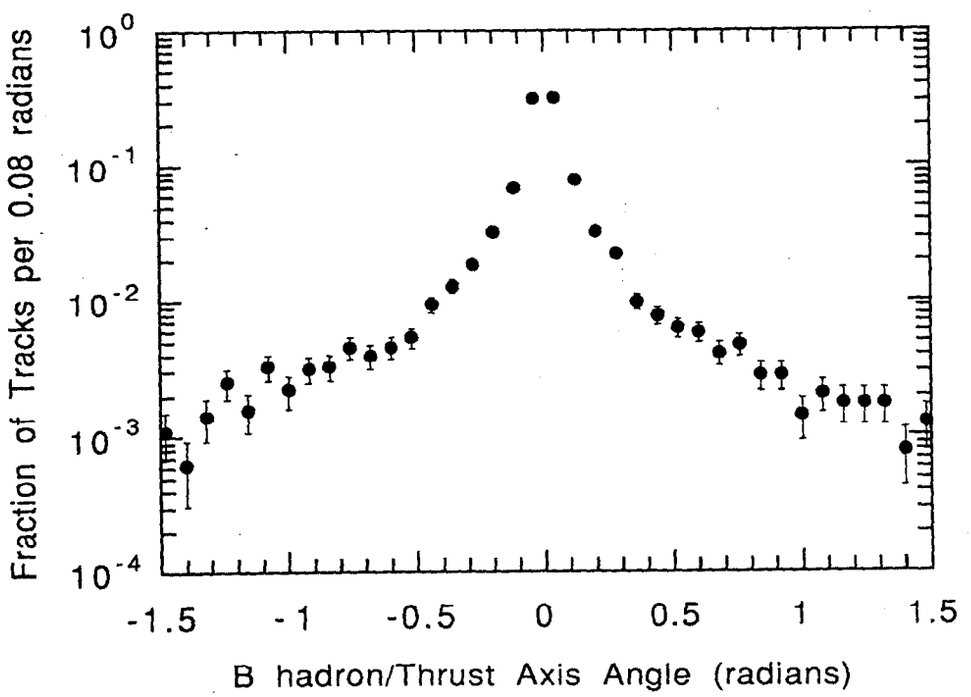

Figure 4–3 Angular separation between the thrust axis and the B hadron directions as determined by the Monte Carlo.

the thrust or sphericity axes. This is to be expected as a significant fraction of events have hard gluon radiation. However, these events retrieved from the tail of the B hadron direction/thrust axis distribution by using a jet algorithm will be those in which the B had fairly low momentum. As a result, the decay products will also have low momentum which will make them more difficult to use in identifying $b\bar{b}$ events and thus there is negligible change in the tag characteristics. (See the next chapter for a discussion of the tagging method.)

4.1.2.2 Determination and Analysis of the Impact Parameter Sign

The sign of the impact parameter is determined in the following manner: if the track crosses the thrust axis in the same thrust hemisphere as the track, then $b > 0$, otherwise $b < 0$. This is illustrated in Figure 4–4. This definition is useful because all of the B decay products are swept forward by the B's large boost into the hemisphere defined by the B direction for $p_B > 8$ GeV. Since the B direction is fairly well approximated by the thrust axis, the majority of the tracks from B decay will have $b > 0$.

Negative impact parameter tracks will come from a number of sources. In all types of hadronic events, the impact parameters of tracks from the IP will be smeared due to the finite resolution of the detectors. This will result in the typical Gaussian-like distribution around $b = 0$. There are also a number of other

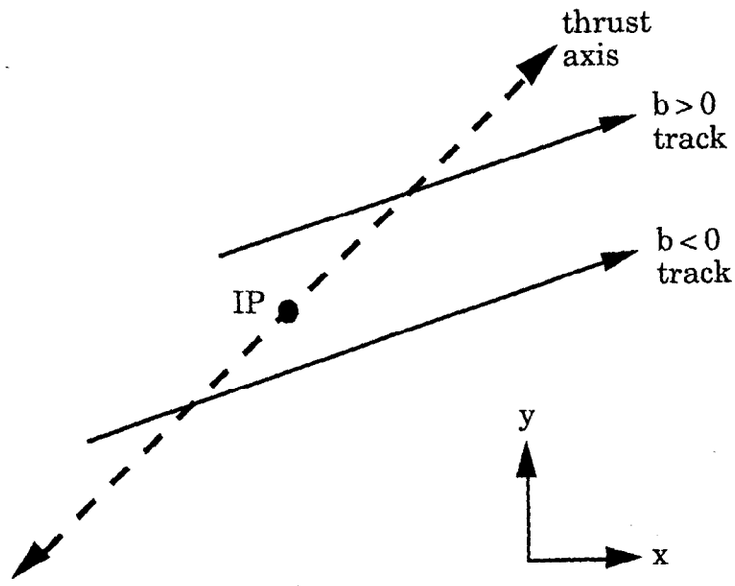

Figure 4–4 The method for assigning an algebraic sign to the track impact parameters using the event thrust axis is illustrated here.

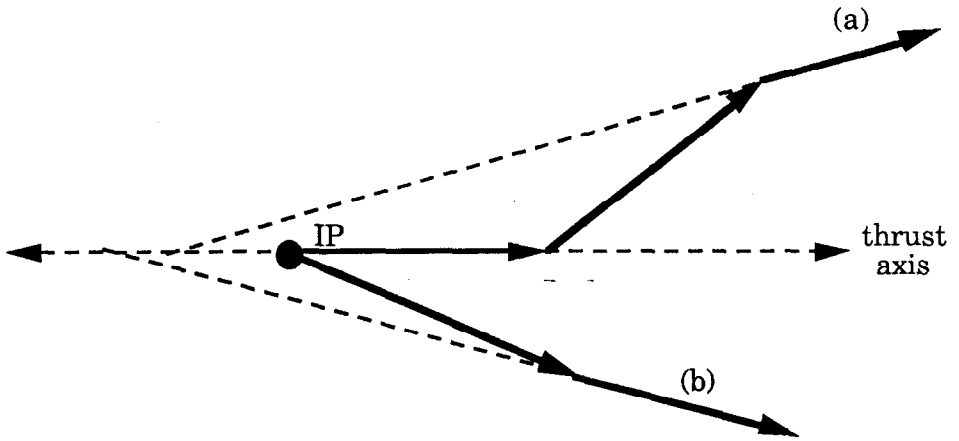

Figure 4–5 Some of the mechanisms for tracks from a long-lived parent being assigned a negative impact parameter when using the thrust axis to determine the sign: (a) tertiary decays, and (b) a misalignment between the thrust axis and the parent particle.

possibilities for generating negative impact parameter tracks particularly for tracks resulting from the decay of long-lived particles (bottom, charm and strange-flavored hadrons). As illustrated in Figure 4–5, these sources include:

- actual backward going tracks, which should be only a few, as most of the decay products will be swept forward along the parent's direction;
- secondary decays such as $B \rightarrow D \rightarrow X$ where the lifetime of the second generation particle (*i.e.* the D) allows the decay vertex at which the daughter X is produced not to lie on the B direction;
- instances in which the thrust axis and parent direction are not well aligned, for instance $b\bar{b}$ events with a hard radiated gluon or tracks from K_s^0 decay.

The level to which each of these contribute for the particles from B hadron decay at the Z^0 can be quantified using the Monte Carlo. Figure 4–6(a) shows the generated impact parameters with respect to the actual IP, for tracks from prompt B decay,* where the actual B-direction has been used to apply the impact parameter sign. Thus the only source of the negative impact parameter tracks are actual backward going decays which are indeed a small fraction (2.1%). A fairly small result is expected, because as pointed out earlier, only tracks from the few very low momentum B hadrons can decay into the hemisphere opposite the B direction. As shown in Figure 4–6(b), when all of the tracks from B decay are included, such as

* In this context, "prompt B decay tracks" are those tracks resulting directly from a B decay, and not from subsequent decays (of a D or K, for instance). This latter set of tracks will be referred to as the "non-prompt B decay tracks."

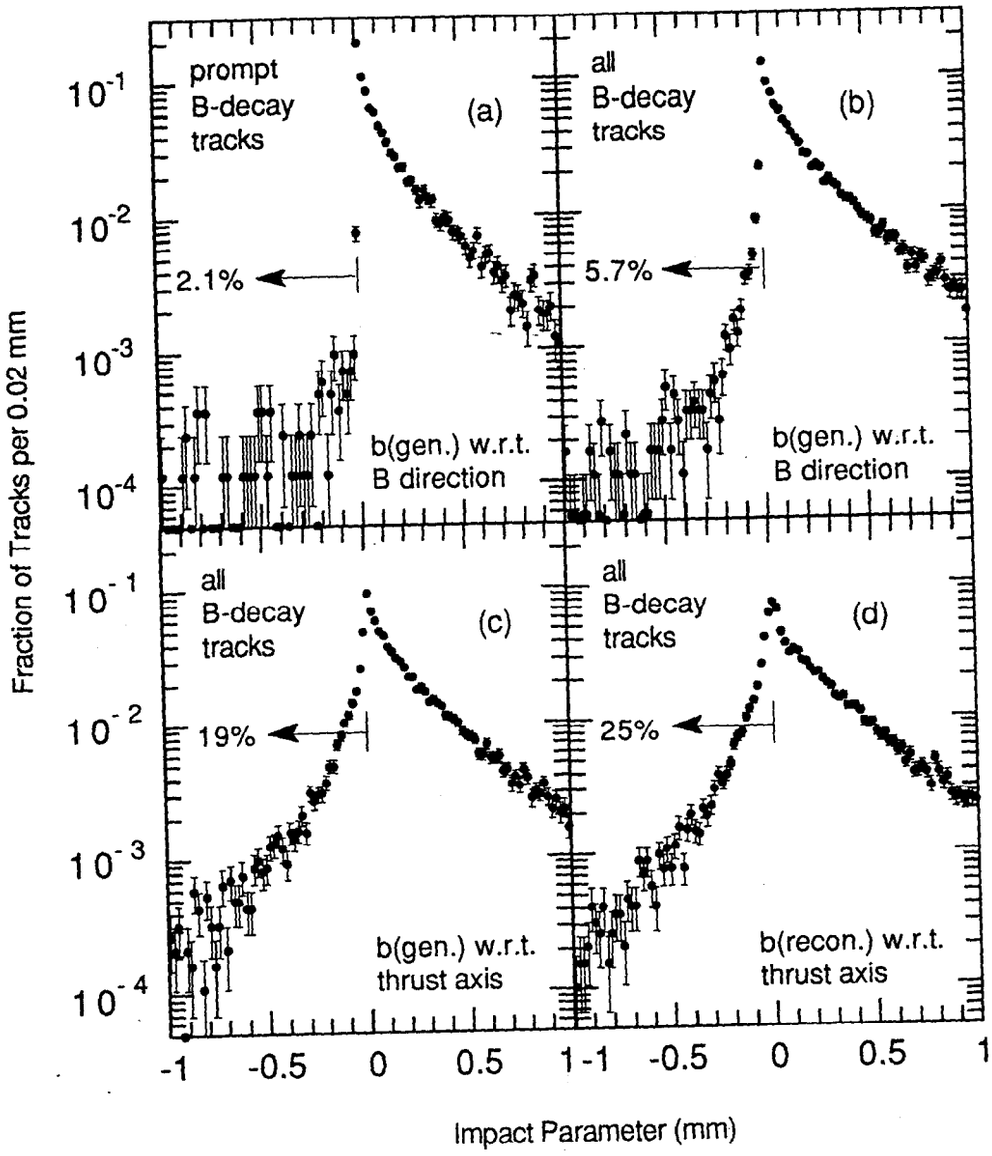

Figure 4–6 These plots illustrate the level that various effects contribute to producing negative impact parameters for tracks from B decay: (a) the impact parameters of the *generated* prompt B decay tracks using the B hadron direction to determine the sign; (b) impact parameters for all of the generated tracks from B decay (including tertiary decays such as $B \rightarrow D \rightarrow X$); (c) impact parameters of the generated tracks which are signed using the thrust axis; (d) the impact parameters of the *reconstructed* tracks, again using the thrust axis. The thrust axis used is that determined with the reconstructed tracks. The tracks used in these plots were all reconstructed by the tracking algorithms and are required to have passed a series of track quality cuts (see Section 4.4 on page 128).

tracks from a tertiary D decay vertex, the fraction of the tracks which are given negative impact parameters using the actual B direction is still small (5.7%), but slightly larger than the fraction in prompt B decay. This increase in the fraction of negative impact parameter tracks is the consequence of the fact that tracks from tertiary decay vertices may have negative impact parameters, as illustrated in Figure 4–5. To observe the effects of using the thrust axis instead of the B direction to sign the impact parameters, Figure 4–6(c) shows the generated impact parameters for all tracks from B decay, now using the thrust axis found with the reconstructed tracks. The effect is to double the fraction of tracks with negative impact parameters to 21%. Finally, the effect of detector resolution is included by using the impact parameter reconstructed with the tracking algorithms from the full detector simulation. The reconstructed impact parameter is also with respect to an IP which is determined for each event using a fit of these reconstructed tracks (see Section 4.2 on page 123). These detector effects show the level to which fluctuations of a track's impact parameters cause them to be assigned a negative impact parameter, as illustrated in Figure 4–6(d). The effect of the detector resolution produces slightly more $b < 0$ tracks, causing a total of 25% of the tracks from B decay to be assigned negative impact parameters. There is another interesting effect, which is the narrower central peak compared with the other distributions. This is an artifact of the use of the event-by-event fit IP, which will tend to pull towards the small impact parameter tracks which are included in the fit.

The effects of this impact parameter signing method on the different flavors of events is illustrated in Figure 4–7 which shows the distribution of reconstructed impact parameters. For *uds* events, this distribution has a generally Gaussian shape, with only slight tails from strange particle decays (K_s^0 and Λ). In contrast, $c\bar{c}$ events have a more asymmetric distribution due to the finite lifetime of charmed hadrons, although the positive tail is significantly larger for $b\bar{b}$ events owing primarily to their longer lifetime. Both of the heavy quark events have a significant fraction of their tracks which are from the primary vertex, such as those from fragmentation, which form a central core to the distribution.

4.1.3 Impact Parameter Resolution

Because of the finite resolution of any tracking detector, the measurement of the impact parameter for a track will have associated with it some level of uncertainty.

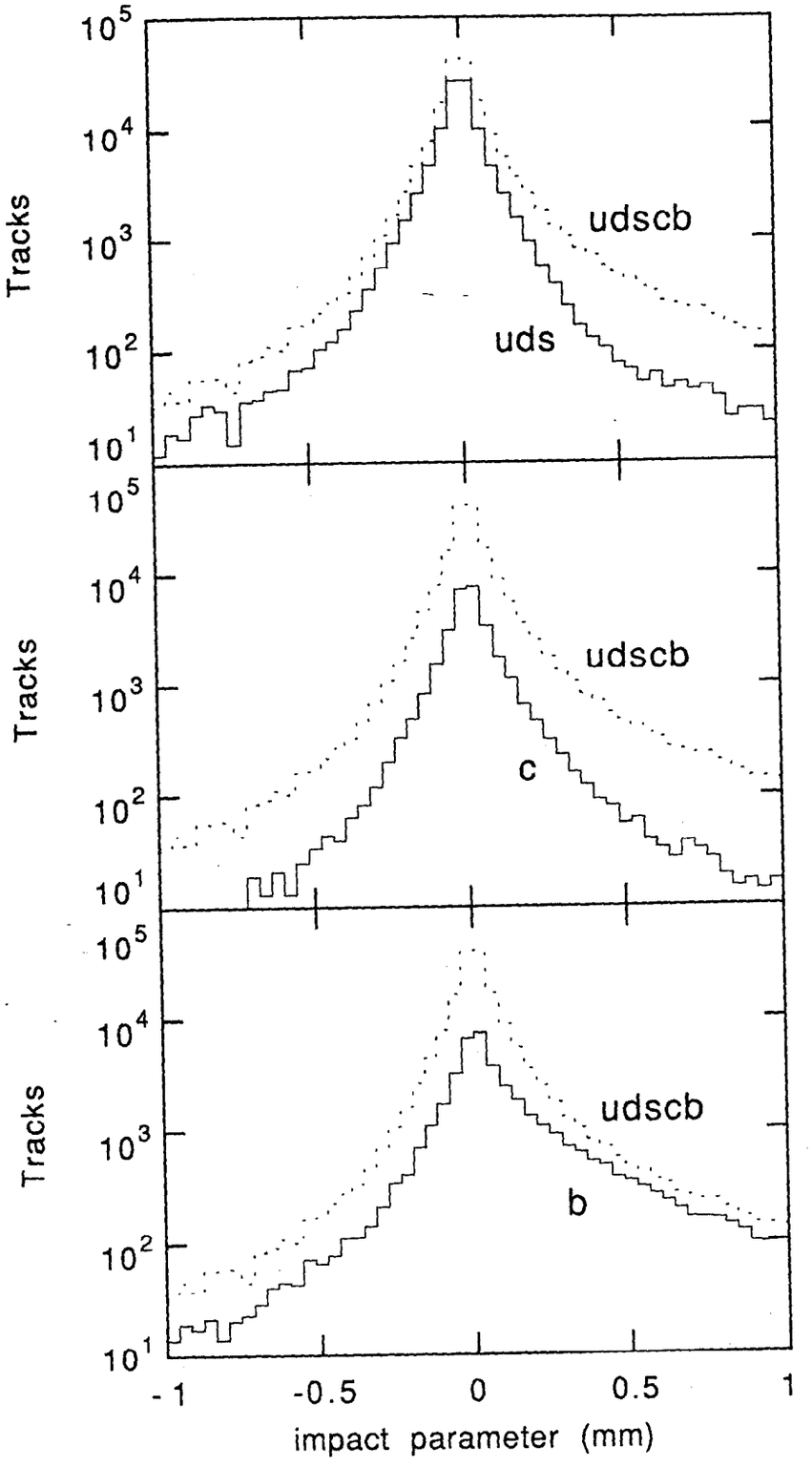

Figure 4–7 The reconstructed impact parameter distributions for different flavors of events as predicted by the Monte Carlo.

Understanding the impact parameter resolution function is important in order to properly model the detectors by the Monte Carlo simulation.

The impact parameter resolution has contributions from two primary sources: the resolution of the measured track extended to its point of closest approach to the IP, σ_{TR}, and the uncertainty in the actual interaction point, σ_{IP}, which is discussed in Section 4.2. The impact parameter resolution is thus related to the sum in quadrature of these two terms,

$$\sigma_b \propto \sqrt{\sigma_{TR}^2 + \sigma_{IP}^2}. \tag{4-7}$$

The uncertainty of the track measurement can be expressed in terms of two components, one which represents the intrinsic detector resolution, σ_{int}, and a second which accounts for the multiple Coulomb scattering of low momentum tracks, σ_{ms}. The resulting relation is

$$\sigma_{TR}^2 = \sigma_{int}^2 + \sigma_{ms}^2. \tag{4-8}$$

4.1.3.1 Intrinsic Resolution Term

For tracking detectors which are composed of a series of n equally spaced position measurements of resolution, σ_0, extending from an inner radius of r_i and to an outer radius of $L + r_i$ from the IP, the intrinsic resolution is given by

$$\sigma_{int} = \frac{\sigma_0}{\sqrt{n}} \sqrt{1 + 3\frac{n-1}{n+1}\left[\frac{L+2r_i}{L}\right]^2}. \tag{4-9}$$

One can see several trends from this expression which can in general be extrapolated to more complicated detector systems where such a straightforward expression can not as easily be obtained. First, the track resolution varies essentially as $n^{-1/2}$ which would of course be expected from statistics, so it is beneficial to have many position measurements. Second, the best resolution is achieved by minimizing the inner radius, r_i, and maximizing the lever arm, L.

Equation (4-9) is not valid for the entire detector system containing detectors of widely varying resolution and spacing, particularly with the advent of silicon vertex detectors which usually have only a few layers of very high position resolution. As is the case for the Mark II, when a silicon detector is used in conjunction with lower

resolution outer detectors one can imagine that the intrinsic resolution may roughly be expressed as

$$\sigma_{int}^2 = \sigma_0^2 + (r_0\sigma_\varphi)^2 \tag{4-10}$$

where σ_0 and r_0 are the average position resolution and radius of the silicon detector and σ_φ is the angular resolution of the outer tracking detectors which provide an accurate angular measurement for most tracks. As will be discussed latter, for very low momentum tracks, the best measurement of the angle is made within the SSVD itself.

4.1.3.2 Multiple Scattering Resolution Term

At low momentum, the measurement accuracy of a track is limited by the multiple Coulomb scattering as it passes through the material in the beam pipe and the detectors. If, as was the case in the past, the beam pipe and inner wall of the vertex detector were the dominant source of material, then the multiple scattering contribution to the track resolution would be

$$\sigma_{ms} = \frac{r_{pipe}}{\sin\theta} \cdot \Phi_{ms}(\vec{p}, x_{pipe}) \tag{4-11}$$

where, r_{pipe} is the beam-pipe/inner wall radius, θ is the dip angle to the beam axis and Φ_{ms} is the related to the width of the scattering angle distribution for a track of momentum $\vec{p}$ and beam pipe thickness of x_{pipe} (see Figure 4–8)

In general, this multiple scattering angular distribution is well described by the Molière theory which has been investigated in numerous papers[104] and is incorporated into the Monte Carlo detector simulation (see Section 3.4 on page 102). In order to develop some intuitive feel for the effects multiple scattering, an approximate formalism can be used. For small-angle scattering however, the angular distribution is roughly Gaussian in nature. Thus it has become commonplace to approximate the angular distribution as a Gaussian distribution of width Φ_{ms}. This width was first approximated as[108]

$$\Phi_{ms} = \frac{E_c}{\beta c p}\, z\sqrt{\frac{x}{X_0}}, \tag{4-12}$$

where E_c is a constant with units of energy, p, βc and z are the momentum, speed and charge of the particle, x is the material thickness and X_0 is the radiation length of the material. (A radiation length is defined as the "mean distance over which a high energy electron loses all but $1/e$ of it's energy by bremsstrahlung"[25] and very

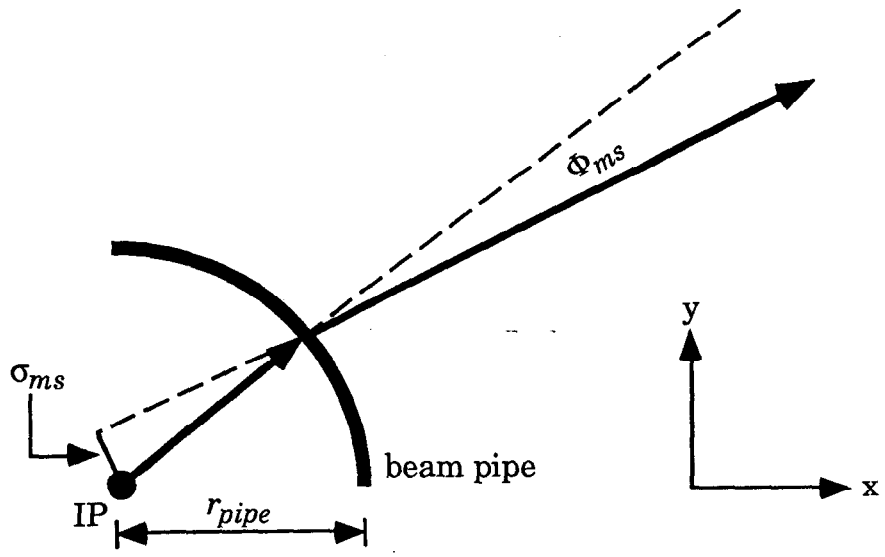

Figure 4–8 A simplified view of multiple scattering where the dominant source of scattering is the beam pipe/inner detector wall before the detectors. The amount of additional error in the measurement of impact parameter due to this scattering is the product of the rms scattering angle, Φ_{ms}, and the distance from the IP, $r_{pipe}/\sin\theta$ where θ is the dip angle.

roughly depends on the atomic number of the material from which the particle is scattering as Z^{-2}.)

Later it was shown that the width of the scattering angle distribution could be much better approximated by an additional dependence on the material thickness which led to a new formula:[109]

$$\Phi_{ms} = \frac{E_c}{\beta cp}\, z\sqrt{\frac{x}{X_0}}\left[1 + C\ln\frac{x}{X_0}\right]. \tag{4-13}$$

The most recent determination of the constants for Equation (4-13) has been done in Reference [110] and yields

$$\Phi_{ms} = \frac{13.6\text{MeV}}{\beta cp}\, z\sqrt{\frac{x}{X_0}}\left[1 + 0.038\log\frac{x}{X_0}\right] \tag{4-14}$$

Upon comparison to Molière theory, it is seen that this width is the same as the width of the central 98% of the Molière distribution to an accuracy of 11% for a range of scatterer thicknesses of $10^{-3} < x/X_0 < 100$ for all Z.

In the cylindrical geometry of the Mark II, the amount of material through which a track traverses varies with the polar angle as $x_0/\sin\theta$ where x_0 is the

thickness of that layer. Thus, the resulting contribution of the multiple scattering to the track extrapolation resolution can be written by substituting this last equation into Equation (4-11),

$$\sigma_{ms} = r_{pipe} \cdot \frac{13.6\text{MeV}}{\beta cp\,(\sin\theta)^{3/2}}\, z\sqrt{\frac{x_0}{X_0}}\left[1+0.038\log\frac{x_0/\sin\theta}{X_0}\right]. \tag{4-15}$$

This illustrates the general dependence of the multiple scattering term on the track momentum and direction,

$$\sigma_{ms}(p,\theta) = \frac{\sigma^{o}_{ms}}{p\,(\sin\theta)^{3/2}} \tag{4-16}$$

where the weak dependence of the logarithmic term on $\sin\theta$ has been ignored and it is assumed that $\beta \approx 1$.

4.1.3.3 Total Track Resolution

The Mark II tracking detector system is actually more complex than the models presented in the previous two sections, but the results of these models will provide some guidance when working with the real system. In particular, the track resolution is expected to have the form

$$\sigma^2_{TR} \approx \sigma^2_{int} + \left[\frac{\sigma^{o}_{ms}}{p\,(\sin\theta)^{3/2}}\right]^2 \tag{4-17}$$

which was derived assuming all of the scattering comes from the beam pipe or first measurement layer. In actuality, there is substantial scattering material throughout the detectors. Thus, the calculation of σ_{TR}, from the error matrix of the track, as determined by the track fitting programs (see Chapter 2) will be more complex than Equation (4-17). Different approaches are taken to include the effects of multiple scattering in this fit. In the CDC and DCVD, multiple scattering is accounted for both by allowing a kink in the track fit between the chambers and with a correction term to account for material in the tracking volume, as derived by Gluckstern[61]. This correction is not strictly valid in our case, as it is derived for detectors with equally spaced layers of equal spatial resolution, but it nonetheless works satisfactorily. In the SSVD, the multiple scattering is handled properly by its inclusion in the covariance matrix for the full track fit.[73]

Figure 4–9(a) shows the calculated track resolution at the distance of closest approach to the IP as a function of $[p\,(\sin\theta)^{3/2}]^{-1}$ for a collection of Monte Carlo

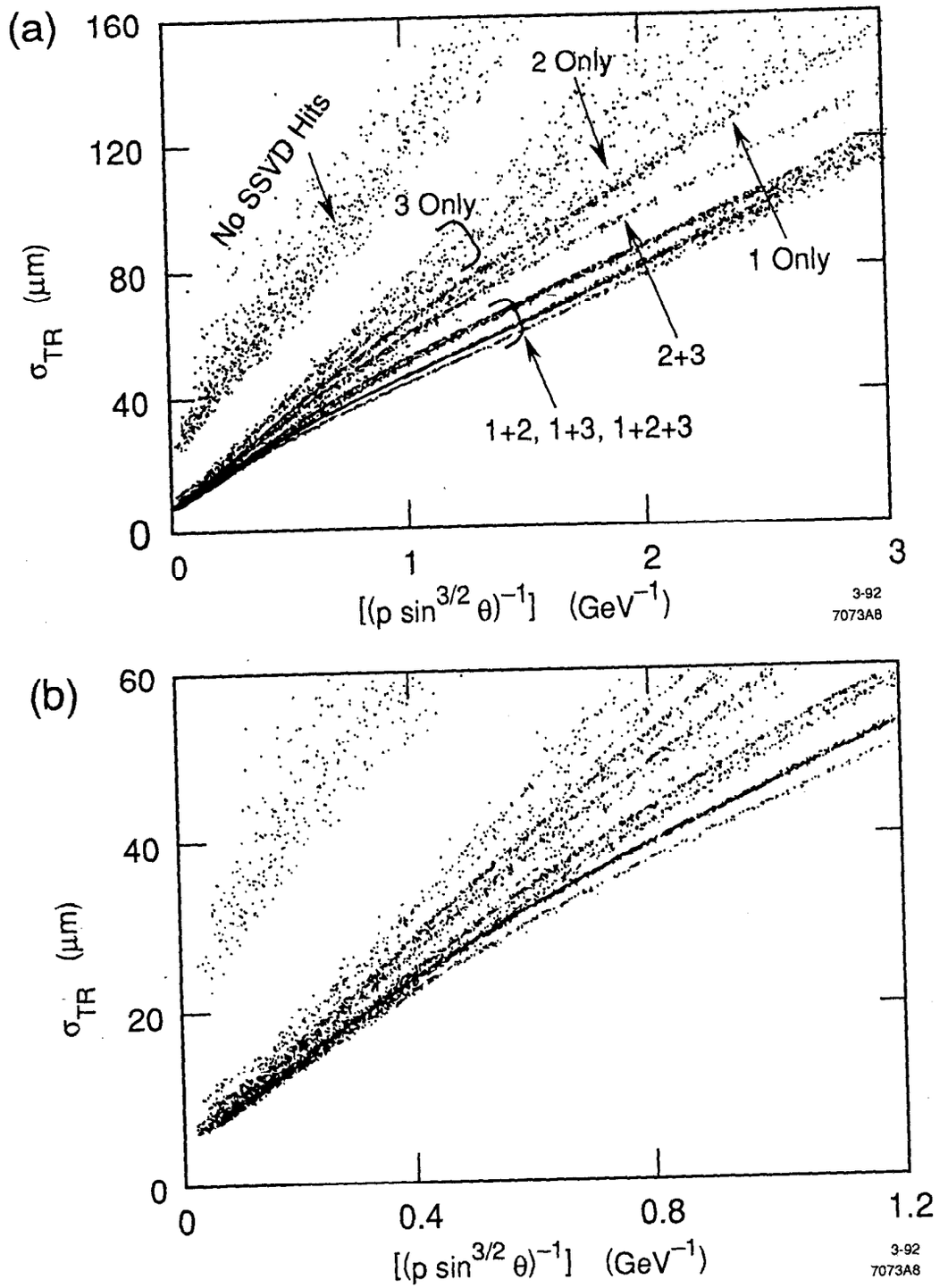

Figure 4–9 The calculated impact parameter resolution of the full CDC, DCVD and SSVD tracking system is shown as a function of the track momentum. These points were calculated for a collection of Monte Carlo tracks using the position measurements determined with data for each detector.

tracks using the position resolution measurements discussed in Chapter 2. The tracks included in this figure must have passed a general series of cuts, most importantly that there be at least 25 (15) position measurements in the CDC (DCVD). The tracks with no found SSVD position measurements are clustered in the upper left of the plot, namely they have the worst resolution for a given momentum. This is due primarily fact that the track must be extrapolated back toward the IP over a longer distance and through more scattering material. Those tracks with only one position measurement in the SSVD are to the right of the CDC/DCVD-only tracks and are separated by the layer in which the SSVD hit occurred, again due to the same argument as above. These tracks with no more than one SSVD position measurement have their impact parameter determined in essentially the same manner as high momentum tracks: the angle of the track is determined by the CDC and DCVD while the track is fixed to a point near the IP essentially by the SSVD or DCVD, depending on whether a SSVD hit was found. The resolution for each combination of hits is spread over fairly broad bands because of the various combinations of CDC and DCVD hits as well as the polar angle of the track.

Tracks with two or more hits in the SSVD have even better resolution, as can be expected, and separate clearly into bands depending on the combination of the three SSVD layers which have position measurements on the track (*i.e.* 1+2, 1+3, 2+3 or 1+2+3). What is different about the low-momentum track resolution determined for these tracks is that the polar angle of the track is determined almost solely by the SSVD. This is because the scattering material between the SSVD and DCVD degrades the extrapolation of the track from the CDC and DCVD as the track momentum is lowered, until at momenta lower than 2-3 GeV, the SSVD can itself measure the angle of the track better than the CDC and DCVD, despite its very small lever arm. As the track momentum increases, the effect of multiple scattering is diminished and the greater lever arm of the outer chambers provides a better angle determination. Graphically this can be seen in Figure 4–9(b). The slope of the resolution dependence on the momentum is shallower at low momentum than at larger momentum where the angle information from the CDC and DCVD becomes useful, providing a better measurement of the track.

4.2 Interaction Point Determination

Recall that the impact parameter resolution as given in Equation (4-7), contains contributions from the track measurement accuracy as well as the knowledge of the

interaction point. A particularly advantageous feature of the SLC is the very small size of the beam spots at the interaction point, where the beams have a diameter of less than 5 microns. In contrast, a storage ring typically has significantly larger beam spots. In the case of LEP, these are about 20 microns in the vertical plane and 150–200 microns in the horizontal plane. Although the beam spots are less than 5 microns in diameter, the knowledge of their position with respect to the tracking [112]detectors must still be determined. While instrumentation in the SLC final focus provides some information as to the relative position of the beams, the determination of the absolute beam position necessitates using Z^0 events. As described below, this is done using hadronic events and fitting for a vertex using a subset of the tracks which best match to this vertex. The resulting fit vertex position can either be applied on an event-by-event basis or as an average over groups of events. This latter option is discussed in Section 4.7.

4.2.1 Interaction Point Finding Algorithm

The interaction point finding algorithm involves building up a vertex by sequentially adding tracks to the vertex fit which have the highest probability of having originated in a common point. Specifically, the algorithm begins with the four tracks that have the smallest impact parameters to a seed interaction point location. The four combinations of three of these tracks are then fit to a vertex in the xy plane and the χ^2 probability for those tracks to form a vertex calculated. The combination with the largest probability is then taken as the initial vertex to which other tracks will be added.

To add more tracks to the vertex, each of the remaining tracks is individually fit to a vertex with the three tracks found in the initial vertex fit and the χ^2 probability of that vertex calculated. The additional track which yields a vertex of the largest χ^2 probability is then permanently added to the vertex. The process is then repeated with the remaining tracks, individually fitting a vertex with each additional track and the tracks already assigned to the vertex, then again permanently keeping the track with the highest χ^2 probability in the vertex. The process of adding tracks to the fit vertex is then terminated when none of the additional tracks yield a vertex of a χ^2 probability greater than 0.01.

Using all detected tracks as candidates for the vertex, as will be standard when using an event-by-event determined vertex, the resulting fit vertex typically has an error ellipse with a semi-major axis (σ_x) of 30–60 μm and a semi-minor axis (σ_y) of 5–15 μm, for an aspect ratio of roughly 5:1. The direction of the semi-major axis is

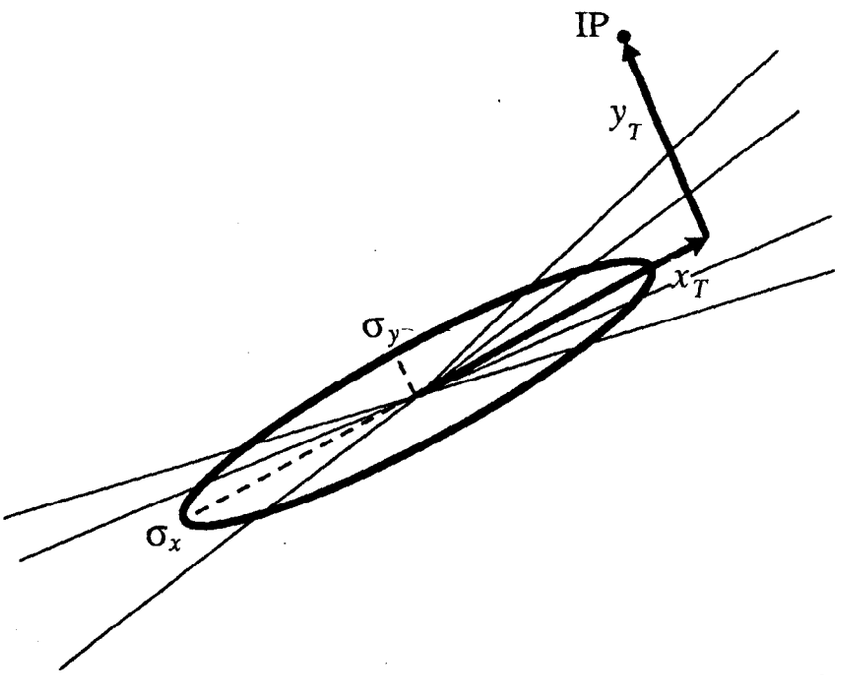

Figure 4–10 Definitions of the variables used in studying the interaction point fit results.

usually fairly parallel to the thrust axis. On average, about 60–70% of the detected tracks are used in vertex, which is about 14 tracks in the data. In $b\bar{b}$ events, about one fewer tracks are, on average, are included in the vertex fit. The fraction of the tracks from a B hadron decay which are included in the fit decreases roughly linearly from about 68% for a decay length less than 1 mm to about 55% for a decay length of about 10 mm. This level to which these tracks affect the fit is discussed below. This algorithm successfully finds an interaction point location with three or more tracks for all events which pass the event selection cuts (see Section 4.3).

Useful quantities to use in studying the vertex fit results are the distance perpendicular (y_T) and parallel (x_T) to the major axis, between the fit and assumed vertex position. These variables are illustrated in Figure 4–10. Expected distributions for y_T as calculated by the Monte Carlo are shown by event flavor in Figure 4–11. It can be seen that the y_T distribution for $c\bar{c}$ events is only slightly wider than that for *uds* events and neither has very significant non-Gaussian tails. The $b\bar{b}$ events have a notably broader y_T distribution than *uds* or $c\bar{c}$ events. A wider distribution for $b\bar{b}$ events would be expected for a number of reasons. First, on average, fewer tracks are included in the fit vertex in $b\bar{b}$ events than in *udsc* events. Furthermore, a broader tail might also be expected as there will be some

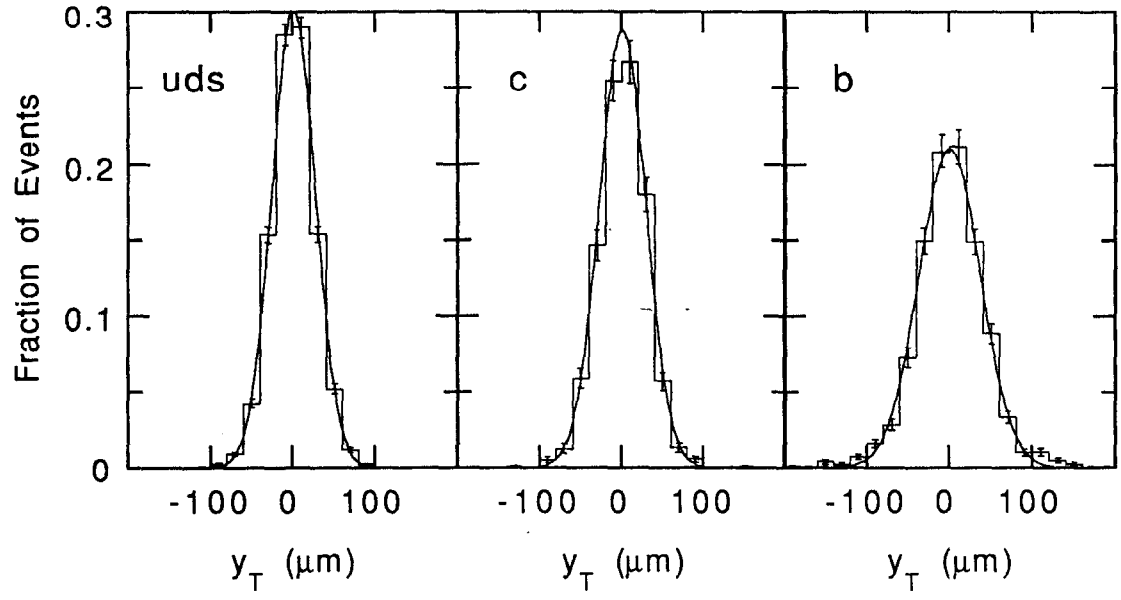

Figure 4–11 *Monte Carlo predictions of y_T distributions for different flavors of events with 25 μm of IP motion in the Monte Carlo. All events which pass the event selection cuts (see Section 4.3) are included in these plots.*

instances where the fitting algorithm found a secondary vertex rather than the primary one, particularly when the B hadrons decay with a short lifetime. These effects combine to make the y_T distribution ~40% wider than that for the lighter quark species. However, the lack of a very large tail indicates that in the vast majority of the events, the vertex finding algorithm is doing quite well even in multi-vertex events. The distributions between the actual and found vertex along the major axis of the error major axis of the error ellipse, x_T, shown in Figure 4–12. As is the same for the y_T distribution, the x_T distribution is broader for the $b\bar{b}$ events, in this case by about 20%.

It is interesting to note that the error assigned to the vertex ellipse underestimates the actual error with which the vertex is determined. This can be seen when the Monte Carlo is studied with no generated IP motion. The average error along the minor axis is 12 μm while the y_T distribution has a Gaussian fit width of 18 μm and a standard deviation of 26 μm. The source of this discrepancy and the non-Gaussian tail is largely due to tails in the impact parameter distribution which are not accounted for in the impact parameter resolution assigned to a given track. These impact parameter tails and the treatment of them in the Monte Carlo will be discussed later in Section 4.5.

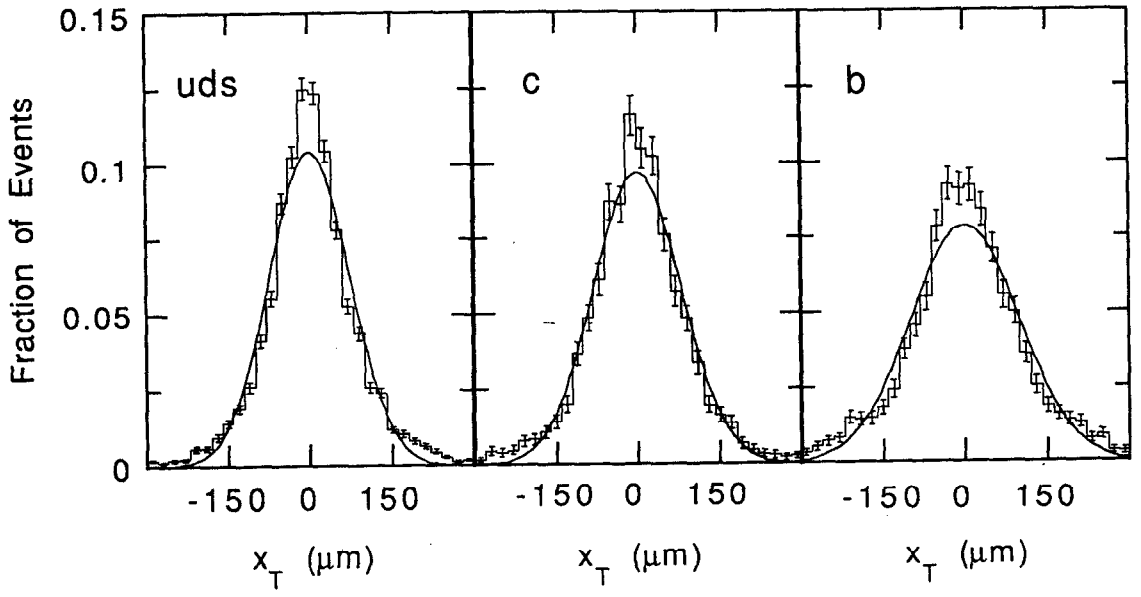

Figure 4–12 Monte Carlo predictions of x_T distributions for different flavors of events with 25 μm of IP motion in the Monte Carlo. All events which pass the event selection cuts (see Section 4.3) are included in these plots

4.3 Event Selection Cuts

The event selection cuts first require that the event pass a standard set of cuts which select hadronic events and reduce the background from e^+e^-, $\mu^+\mu^-$, $\tau^+\tau^-$ events and random background events. These cuts are:

- At least 7 tracks must be in the nominal fiducial volume. Specifically, these tracks must satisfy the following four minimal requirements.
  1. The calculated angle of the track with respect to the beam axis must satisfy $|\cos\theta| < 0.8$ such that the tracks are well inside the active regions of the tracking detectors.
  2. The projection of the track's momentum into the plane perpendicular to the beam axis, p_{xy}, must be greater than 0.150 GeV/c.
  3. The distance of closest approach in the z-direction of the track to the nominal interaction point must satisfy $|z_m| < 15$ mm.
  4. The number of hits associated with the track in the CDC tracking must be at least 25 of the 72 possible.

- The sum of the observed charged and neutral visible energy must be at least half of the center-of-mass energy, where charged tracks are assigned the mass of a pion. Specifically, this requirement is

$$E_{vis} = \sum_{i}^{n_{ch}} \sqrt{p_i^2 + m_\pi^2} + \sum_{i}^{n_{neu}} E_i \; > \; 0.5 E_{cm}.$$

These cuts select 80.0% of the hadronic events with a very small non-hadronic background of less than 0.1%. In the 1990 data sample, 220 events pass these cuts.

An additional cut was made to ensure that the events are oriented in the central region of the detector where the tracking detectors are located:

- The angle of the thrust axis calculated using the charged tracks which pass the above cuts only, must satisfy $|\cos\theta_{thrust}| < 0.7$.

This cut reduces the event-to-event fluctuations with negligible loss of statistical power in the analyses to be discussed later. After this cut, the event-selection efficiency is 70.4%, and in our data sample 196 events remain.

4.4 Vertex Quality Track Cuts

Once hadronic events are found, a subset of the tracks within these events are selected whose impact parameter resolution will be thoroughly studied. These *vertex quality* tracks will later be used to tag $b\bar{b}$ events. Initially, it is required that each track pass the four minimal track cuts used in the event cuts. Additionally, a track must satisfy the following requirements that ensure accurate impact parameter determination:

5. The number of hits found on the track in the DCVD must be at least 15 of 32 possible.
6. Similarly, the number of hits found in the track in the SSVD must be at least 1 of 3 possible.
7. The error on the extrapolation of the track back to the interaction point including multiple scattering, σ_{TR}, must be less than 200 μm.

To reduce the number of tracks with large impact parameters which come from non-$b\bar{b}$ sources, in particular those from K_s^0 or Λ decays, multiple Coulomb scattering and nuclear interactions, it is also required that:

8. The impact parameter of the track, with respect to an interaction point which is fit on an event-by-event basis, must satisfy $|b| < 2$ mm.

A total of 2330 tracks in the 220 events pass the cuts which select hadronic events, and 2176 tracks in the 196 events pass all of the event selection cuts (namely the hadronic cuts and the cut on the polar angle of the thrust axis) are found in the 1990 data sample. To maximize the statistical power, the former sample of tracks will be used to study the impact parameter resolution. Table 4–1 gives the fraction of tracks remaining after each cut is applied in order, as estimated by the Monte Carlo.

track cut	% passed
1. $\|\cos\theta\| < 0.8$	92.8%
2. $p_{xy} > 0.15$ GeV	87.0%
3. $\|z_m\| < 15$ mm	79.`%
4. $N_{CDC} \geq 25$	78.9%
5. $N_{DCVD} \geq 15$	62.9%
6. $N_{SSVD} \geq 1$	56.4%
7. $\sigma_{TR} < 200$ μm	55.5%
8. $\|b\| < 2$ mm	52.3%

Table 4–1 The fraction of the reconstructed tracks passing each of the multiplicity track quality cuts for events which pass the hadronic event cuts, but not necessarily the additional cut on the thrust axis dip angle.

4.5 Impact Parameter Resolution Studies

With the above set of high quality tracks defined, it is essential to understand their impact parameter well, since this serves as the basis of the tagging algorithm to select a sample of predominantly $b\bar{b}$ events. This is the case because the Monte Carlo will be used to predict the tagging efficiencies, and thus understanding and properly modelling the impact parameter resolution are critical to an accurate detector simulation.

The impact parameter resolution can be studied in a number of ways, including the use of cosmic rays, lepton pair events and hadronic events. While the first two can provide a straightforward method for determination of the resolution, the use of hadronic events poses some difficulties. In particular, it is these events which will be used in the subsequent analyses of the $Z^0 \rightarrow b\bar{b}$ fraction and the $b\bar{b}$ event

multiplicity both of which use a tag to identify $b\bar{b}$ events which is based on the track impact parameter. Thus, care must be taken not to allow the resolution studies to be biased by assumptions about the quantities to be measured. The primary method used to achieve this independence relies on the use of the physically signed impact parameter, which causes the tracks from B decay and other long lived hadrons to have predominantly positive impact parameters, whereas the tracks from the primary decay vertex will be smeared equally to have positive and negative impact parameters by the finite detector resolution (see Section 4.1.2). Hence, using only those tracks with $b < 0$ will significantly reduce the dependence of the resolution on the tracks from B decay. The level to which this is achieved is discussed later in Section 4.5.3.

4.5.1 Intrinsic Resolution

To study the intrinsic performance of the tracking detector system it is desirable to use high momentum tracks which are insensitive to effects from multiple scattering.

4.5.1.1 Cosmic Ray Events

High energy cosmic ray events provide a good source of events for the study of intrinsic resolution by fitting the two halves of the cosmic ray separately and then looking at the *miss distance*, namely the difference between the extrapolation of the two halves of the track back to the center of the detector. Extensive use was made of cosmic rays by the CDC and DCVD. However, the SSVD electronics are operated in a pulsed mode and thus its livetime is too small to accrue a useful number of cosmic events. A distribution of the miss distance as measured by the CDC and DCVD for cosmic rays with a momentum of at least 15 GeV is shown in Figure 4–13. The Gaussian fit to this distribution gives a width of 55 μm which corresponds to an error on the track resolution of $\sigma_{TR} = 55/\sqrt{2} = 39\ \mu m$. This is about 60% higher than would be expected by calculating the expected resolution using the measured local resolutions for the detectors (as discussed in Sections 2.2.2.5 and 2.2.3.8) presumably due to systematic effects. Although this demonstrates the possibility for improved resolution for these two detectors, this resolution is more than adequate to locate the position measurements on the SSVD for the final impact parameter determination in Z^0 events.

4.5.1.2 Intrinsic Resolution in Hadronic Events

To study the intrinsic performance of the detectors in the hadronic data, a subset of the tracks were chosen which passed the vertex quality track cuts as

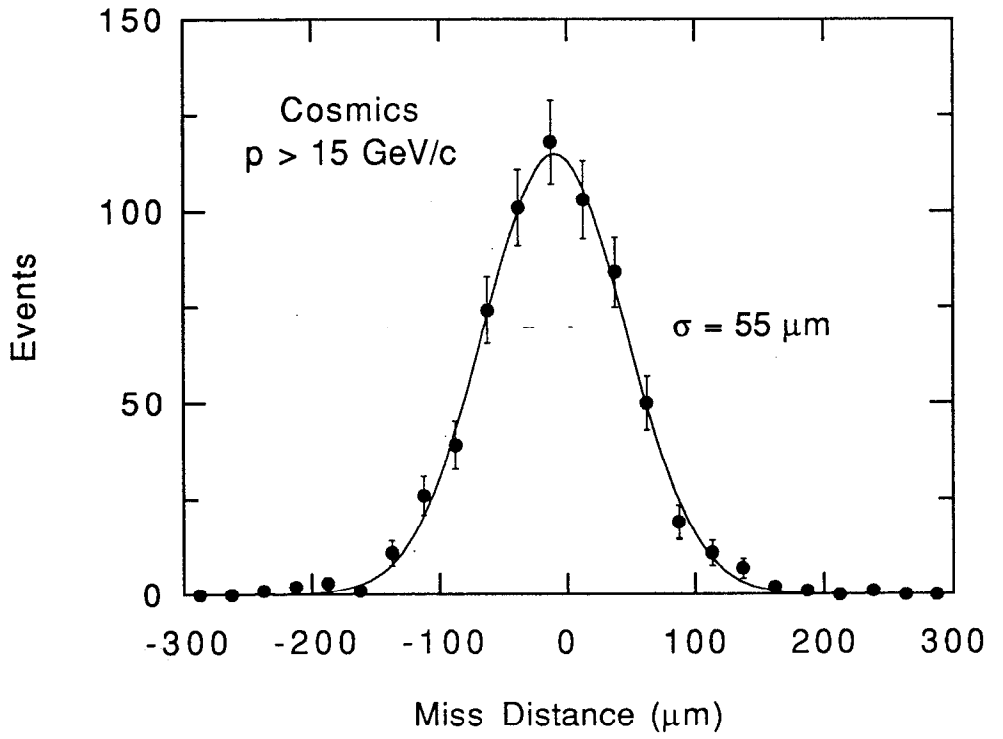

Figure 4–13 The distribution of the miss distance for high momentum cosmic ray events where each half of the track was fit separately. The curve is a Gaussian fit to the data points with a 55 μm width.

described in Section 4.4 and have an extrapolated track error, σ_{TR} calculated to be less than 25 μm. These tracks were chosen as they are virtually unaffected by multiple scattering and provide a well-measured sample of tracks.

The quantity just to study these tracks is the impact parameter significance,

$$S \equiv \frac{b}{\sigma_b}, \tag{4-18}$$

where the form used to calculate the impact parameter resolution for the full tracking system is composed of three terms,

$$\sigma_b \equiv \sqrt{\sigma_{TR}^2 + \sigma_{IP}^2 + (15\ \mu m)^2}. \tag{4-19}$$

As discussed previously, σ_{TR} is the error due to the track fit as extrapolated back to its distance of closest approach to the IP, and σ_{IP} is the error due to uncertainty in the IP position. The third term of 15 μm can be attributed to the remaining uncertainty in the alignment of the SSVD* resulting from the limited statistics

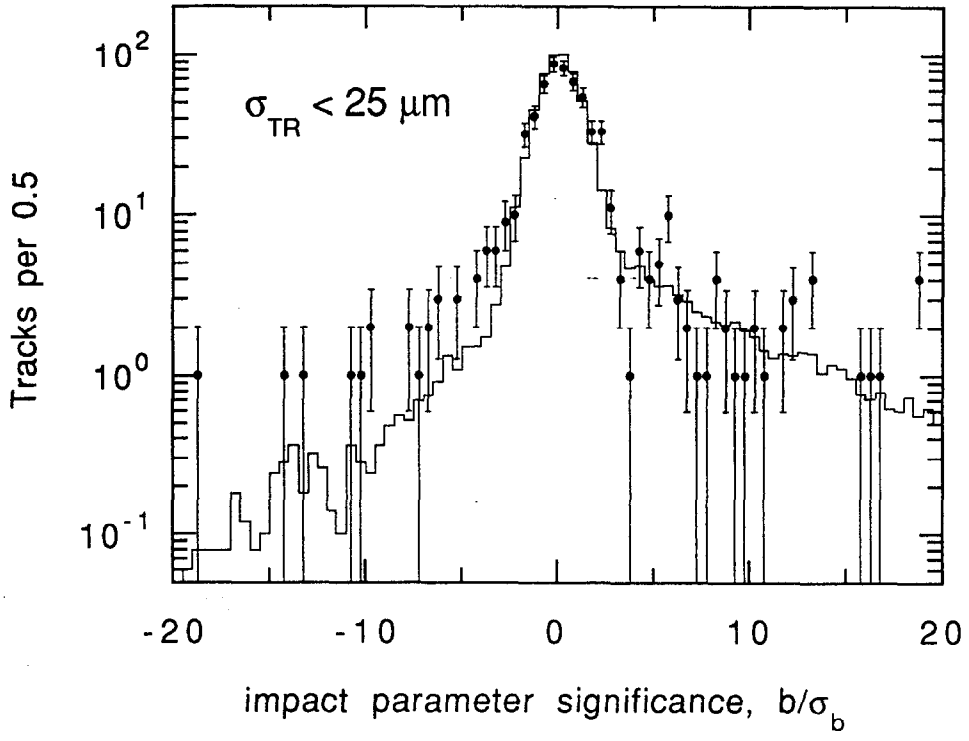

Figure 4–14 The impact parameter significance for data (points) and Monte Carlo (line) tracks with a calculated $\sigma_{TR} < 25$ μm.

available. This value was determined using the Monte Carlo to test the alignment algorithms with many data sets equal in size to our 220 events.

Figure 4–14 shows a comparison of impact parameter significance for the high precision tracks ($\sigma_{TR} < 25$ μm) between the 604 data tracks and a Monte Carlo sample. In this plot and the others in this section, the impact parameter is calculated with respect to a vertex which is determined on an event-by-event basis. In these resolution studies, the interaction point location is fit separately for each track, and in each fit the track in question is omitted from the fit. This is done to reduce correlations resulting from a track being used in the fit for the interaction point location which in turn is used to calculate the impact parameter of that track. Comparing only the left side of these distributions, which will be used to study the resolution fairly independently of the contribution of tracks from B decays, it is clear that the Monte Carlo underestimates the resolution of the detectors.

A concerted effort was made to determine the source or sources of this systematically degraded resolution and despite finding and accounting for

* See Section 2.2.4.4 on page 77 for information on the SSVD alignment.

numerous sources of lower resolution, there remained a notable difference between the observed impact parameter significance distribution and that predicted by the Monte Carlo. It is certainly possible, and indeed likely, that with a larger data set the detector performance would be better understood and the data/Monte Carlo brought into agreement by accounting for the individual sources of lower resolution. However, given as that is not the case, the next best solution is to modify the Monte Carlo track impact parameters after they have been determined to obtain agreement with the data. As described below in more detail, the impact parameters of the Monte Carlo tracks are indeed smeared to better match the data and these b-smeared tracks are used in the subsequent analyses in Chapter 6, "The Branching Fraction to Bottom Quarks" and in Chapter 7, "The Multiplicity of Bottom Quark Events". However, the amount of smearing has only a minor affect on the results of these analyses, with the case of no additional smearing being included in the systematic error determination.

Without a particular systematic effect to explain the difference between the data and Monte Carlo tracking performance, the remaining option was to apply additional smearing to the impact parameters of the Monte Carlo tracks randomly. The form of the additional smearing was the sum of two Gaussian probability functions, P_G, where the second is only applied to a randomly selected subset of the tracks. Mathematically this is

$$\mathrm{b} \rightarrow \mathrm{b} + P_G(\sigma_{core}) + \Theta(\mathrm{f}_{tail}) \cdot P_G(\sigma_{tail}), \tag{4-20}$$

where $\mathrm{f}_{tail} \in [0, 1]$ and $\Theta(x)$ is a random function which is 1 for the fraction x of the samples and 0 otherwise. The first Gaussian function accounts for a slightly broader central core in the Monte Carlo impact parameter significance distribution compared to the data, while the second adjusts the tail region just beyond this central peak.

In order to determine optimal amounts of smearing to add to the Monte Carlo tracks, several methods were investigated for quantifying the comparison between the data and Monte Carlo impact parameter significance distributions. These methods included a fit to a functional form which typically consisted of a Gaussian central core and an additional term to account for the non-Gaussian tails. A particular form which worked quite well was

$$N(S = \mathrm{b}/\sigma_{\mathrm{b}}) \propto (1-f)\, e^{-S^2/(2\alpha^2)} + f e^{-|S|/\beta}. \tag{4-21}$$

The fit parameters, the widths of the Gaussian central core (α), the tail (β) and the tail fraction (f), can then be compared for fits done on distributions from the data and Monte Carlo. Reference [73] contains a thorough analysis of this same data set using this method. Although the results in this reference are consistent with other methods, great care must be taken in fitting low statistics data, where fluctuations and bins with no entries can be problematic for least-squares fits.

A comparison of the data and Monte Carlo distributions can also be made without assuming any particular functional form or binning for the data tracks. To make these comparisons, the negative side of the Monte Carlo impact parameter significance distribution was normalized and used as a probability distribution of tracks having a particular impact parameter significance. To reduce the effects of low statistics in the tails of this Monte Carlo distribution, variable bin sizes were used to ensure that each bin had at least 100 entries.* Thus, the probability of each track in the data having a particular negative impact parameter significance can then be calculated and used to find a total probability for the comparison of the data and Monte Carlo distributions. Two methods of computing a probability were investigated for making this comparison.

- The multinomial probability, an extension of the familiar binomial probability, gives the probability of getting a given distribution for an assumed parent distribution. The multinomial probability has the form,[111]

$$P_{mult}(n_1, n_2, n_3 \cdots ; p_1, p_2, p_3 \cdots) = \frac{N!}{\prod_{bin\ i} n_i} \cdot \prod_i (p_i)^{n_i} \tag{4-22}$$

  where the n_i and p_i are the number of data tracks and the Monte Carlo probability of a track being in bin i, and $N = \Sigma n_i$ is the number of tracks.

- The log-likelihood, $\boldsymbol{L}$, which for a given set of data tracks is given by

$$\log \boldsymbol{L} = \log \prod_{track\ j}^{N} p(S_j) = \sum_{bin\ i} n_i \log p_i \tag{4-23}$$

  where j is the index of the data tracks, i is the index over the bins and p is the Monte Carlo probability.

* Twelve bins were used to cover the range $-20 < b/\sigma_b < 0$, and these had lower edges of –20, –8, –6, –5, –4, –3.5, –3, –2,5, –2, –1.5, –1, –0.5

Both methods yield similar results for the optimal amount of additional impact parameter smearing, and so the latter is chosen as the standard definitions of the confidence intervals for a log-likelihood will be useful later.

A range of different smearing was investigated, employing the core-and-tail smearing as described by Equation (4-20) and varying the width the core and tail smearing Gaussians and the fraction of tracks which are smeared by the tail term. Using the log-likelihood comparison, the combination of smearing which makes the Monte Carlo best match the data is that with the maximum log-likelihood. Table 4–2 shows the resulting log-likelihood differences between the combination of smearing with the maximum log-likelihood and that of the other possible combinations. The best data/Monte Carlo agreement is for an impact parameter smearing of

10 μm to all tracks and 100 μm to 10% of the tracks selected randomly.

Figure 4–15 illustrates the effect of this impact parameter smearing on the high precision tracks used for the data/Monte Carlo comparison. Note that the agreement is significantly improved, particularly in the tail region immediately beyond the central core. Also shown in Table 4–2 are the combinations of smearing which are 1σ and 2σ allowed, namely they are <0.5 and <2.0 units of log-likelihood different than the maximum likelihood point. It should be noted that the other measurements[73] of the optimal additional smearing do indeed fall with the 2σ contour for this analysis.

While working well for most of the tracks, the double Gaussian form as used above to provide additional smearing for the Monte Carlo has little effect on the far tail region of the impact parameter significance (beyond about –10) for the high precision tracks. With the above smearing already applied, a very broad additional Gaussian smearing was applied randomly to a fraction of the tracks to investigate a possible range of the far tail smearing. Using the same techniques as used previously, it was found that a small quantity of additional smearing is allowed, and the limits on this smearing are given in Table 4–3. However, the case of no additional far tail smearing is preferred and thus none of this far tail smearing will be used except for placing systematic limits.

4.5.1.3 Lepton Pair Events

Lepton pair events ($e^+e^- \rightarrow e^+e^-$ or $\mu^+\mu^-$) are particularly useful for studying intrinsic detector performance as the produced leptons have energies very nearly

$\sigma_{TR} < 25$ μm	Fraction of tracks with tail smearing							
Width of tail smearing	0%	5%	10%	15%	20%	25%	30%	35%
	0 μm core smearing							
0 μm	9.72	9.72	9.72	9.72	9.72	9.72	9.72	9.72
25 μm	9.72	8.21	6.67	5.23	4.37	3.72	3.79	
50 μm	9.72	6.35	3.55	2.11	1.45	1.43	1.50	2.57
75 μm	9.72	4.56	1.89	0.65	0.63	1.23	3.49	
100 μm	9.72	3.93	1.41	0.90	1.91	4.21	6.71	
150 μm	9.72	4.46	2.59	3.55	6.20	9.46		
200 μm	9.72		4.13	6.18	9.42			
	5 μm core smearing							
0 μm	8.27	8.27	8.27	8.27	8.27	8.27	8.27	8.27
25 μm	8.27			4.68	3.45	3.70		
50 μm	8.27		2.92	1.47	1.02	1.15	1.55	
75 μm	8.27	3.84	1.51	0.53	0.79	1.932	4.23	
100 μm	8.27	2.72	0.50	0.37	1.78	4.13		
150 μm	8.27	4.98	2.54	3.42				
200 μm	8.27							
	10 μm core smearing							
0 μm	5.06	5.06	5.06	5.06	5.06	5.06	5.06	5.06
25 μm	5.06			2.16	1.95			
50 μm	5.06		1.76	1.15	1.57	1.64		
75 μm	5.06	1.76	0.38	0.32	1.35	2.30		
100 μm	5.06	2.35	0	0.47	2.42			
150 μm	5.06	3.15	2.14	3.96				
200 μm	5.06		4.52	7.23				
	15 μm core smearing							
0 μm	3.24	3.24	3.24	3.24	3.24	3.24	3.24	3.24
25 μm	3.24							
50 μm	3.24		2.18	2.44	3.46			
75 μm	3.24		2.31	1.36				
100 μm	3.24	1.99	1.09	1.72				
150 μm	3.24	2.34	2.25					
200 μm	3.24							

Table 4–2 The difference between the log-likelihood for the combination with the maximum log-likelihood (10 μm of core and 10% of the tracks with 100 μm tail smearing) and that with other combinations. The optimal smearing is shaded, while the 1σ and 2σ allowed combinations are bordered by the thick and thin lines.

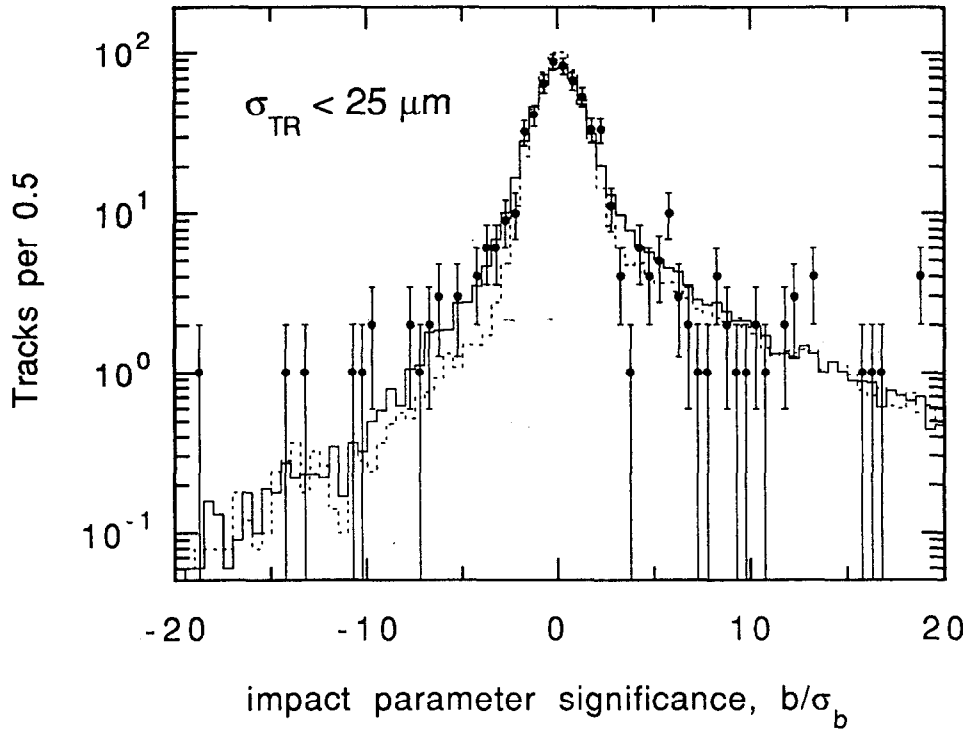

Figure 4–15 The impact parameter significance for the data (points), the unsmeared Monte Carlo (dashed line) and the Monte Carlo with the optimal smearing (solid line) for tracks with a calculated $\sigma_{TR} < 25$ μm.

Width of far tail smearing	maximum allowed fraction of tracks	
	1σ	2σ
250 μm	0.8%	2.2%
500 μm	0.4%	1.3%
1000 μm	0.3%	1.0%
2000 μm	0.3%	0.8%

Table 4–3 Maximum fraction of tracks smeared by a given Gaussian width which are allowed at the level of 1σ and 2σ by the log-likelihood comparison of the data and Monte Carlo tracks with $\sigma_{TR} < 25$ μm.

that of the beam energy, the miss distance measurement is independent of the IP position and the events are free of errors caused by nearby tracks as can be the case

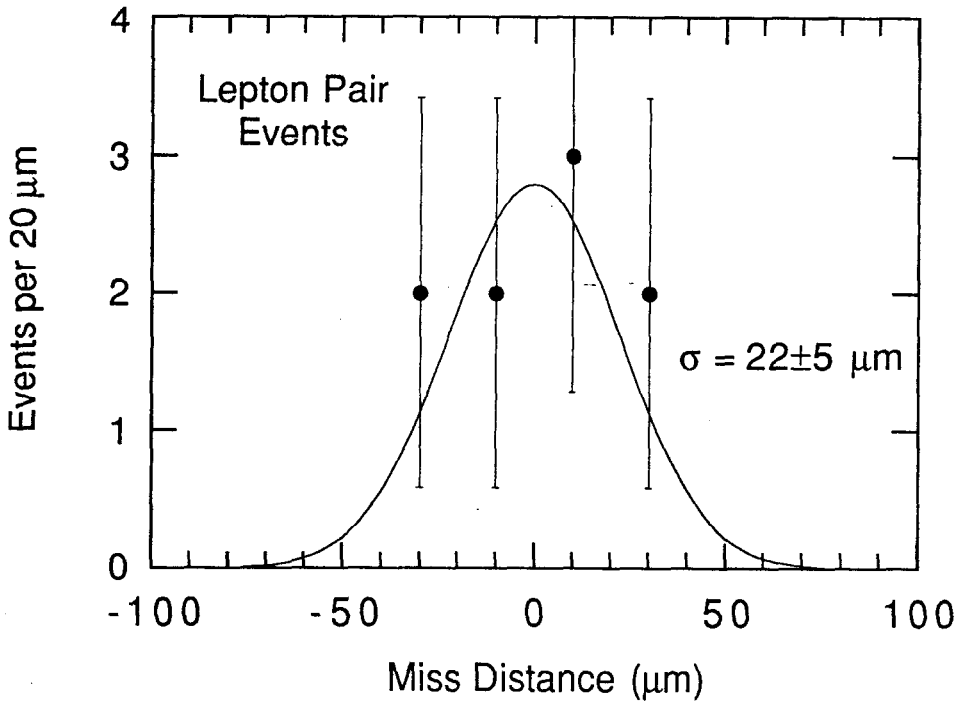

Figure 4–16 The miss distance distribution for the 9 good e or μ pair events.

in hadronic jets. These could, in sufficient number, provide a good measure of the tracking resolution. In the 1991 data sample, there are 21 events which are identified as potential lepton pair events. Applying the standard vertex quality track cuts, as described in Section 4.4, leaves 14 events. In order to remove 1+1 prong τ events, a further requirement is made that each track have a total measured momentum of no less than 3σ below the beam energy. With the Mark II transverse momentum and dip angle resolution, this cut is typically on the order of 35 GeV. A distribution of the miss distance for these 9 remaining lepton pair events is shown in Figure 4–16. The width found by fitting the miss distance distribution to a Gaussian function is 22±5 μm. The default Monte Carlo predicts the width of the miss distance distribution to be 11 μm. With the additional impact parameter smearing as evaluated using high resolution hadronic tracks in the previous section, the Monte Carlo predicts a width of 28 μm, which is consistent with the value observed in the data.

4.5.2 Multiple Scattering-Limited Resolution

The impact parameter resolution for low momentum tracks will be dominated by the amount of scattering material present in the detectors. Thus, proper

Sample of tracks with $100 < \sigma_b < 200$ μm	Gaussian fit σ	standard deviation
MC with Gaussian scattering	1.07	1.56
MC with Molière scattering	1.13	1.67
Data (478 tracks)	1.15±0.05	1.66±0.05

Table 4–4 The fit Gaussian width, σ, and the standard deviation for the Monte Carlo (MC) and data distributions of the impact parameter significance b/σ_b are given for various samples. The Monte Carlo samples were generated using the two methods of applying multiple scattering to the tracks in the detector simulation, a Gaussian distribution and the Molière theory. Note that these were calculated using only the tracks with negative impact parameters.

modeling of the resolution in the multiple scattering-limited regime essentially requires tuning the material in the Monte Carlo to reflect the actual amount of material in the detectors. To do this without being too sensitive to the intrinsic detector resolution or the uncertainty in the IP location, only tracks with a large calculated resolution, $100 < \sigma_{TR} < 200$ μm, were used. Starting with the nominal thicknesses for the various layers, and reasonable estimates of their uncertainties, the thicknesses used in the detector simulation were varied and the resulting distributions of the impact parameter significance distributions, b/σ_b, were compared to those observed in the data.

A major improvement in the agreement between the observed distribution and the Monte Carlo was achieved by implementing Molière Scattering Theory in place of a simpler Gaussian approximation for multiple Coulomb scattering in the detector simulation (see Section 3.4, "Detector Simulation," on page 102). This improvement is reflected in the impact parameter significance distribution of tracks generated using these two methods. As shown in Table 4–4, the results using Molière scattering caused a marked improvement in the data and Monte Carlo agreement compared with the Gaussian formula. Using the Molière scattering in the Monte Carlo generation and the optimally tuned materials, the impact parameter significance distribution for those tracks with $\sigma_{TR} > 25$ μm, namely those not used for the determination of the additional smearing, is shown in Figure 4–17. The agreement for these tracks is also good.

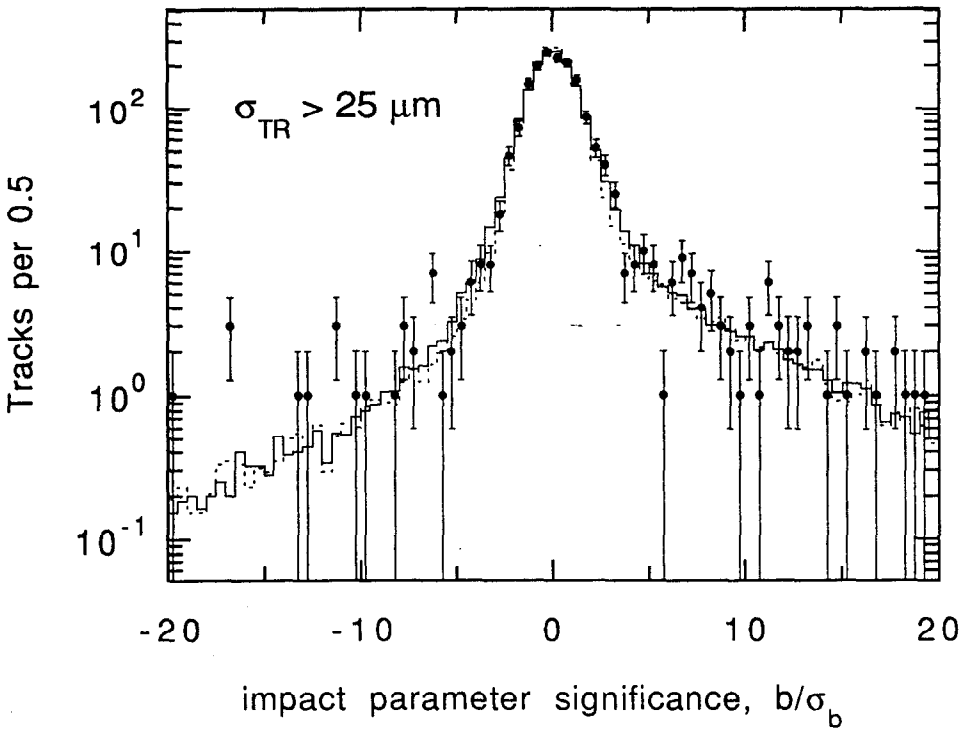

Figure 4–17 The impact parameter significance for the data (points), the unsmeared Monte Carlo (dashed line) and the Monte Carlo with the optimal smearing (solid line) as discussed in Section 4.5.1 for tracks with a calculated σ_{TR} > 25 μm.

4.5.3 Impact Parameter Resolution Checks

In this section, several effects are investigated which have the potential to alter the resolution as measured in the preceding sections. In general, these are effects which will contribute asymmetrically to the impact parameter significance distribution, and because only one side of the distribution (namely that with negative impact parameter tracks) is studied for determining the resolution, asymmetries will not be detected. Applying an algebraic sign to the impact parameter using the thrust axis can cause tracks from long-lived parents to be signed incorrectly for a number of reasons including:

- the Z^0 hadronic branching fraction to $b\bar{b}$,
- the alignment of the thrust axis with the parent B direction, and
- the effects from scattering and particle production in the detector material.

An effect which is of particular concern regarding the asymmetric distribution of positive and negative impact parameter tracks is the variation of the resolution determination due to an incorrect assumption for the value of F_b, the hadronic

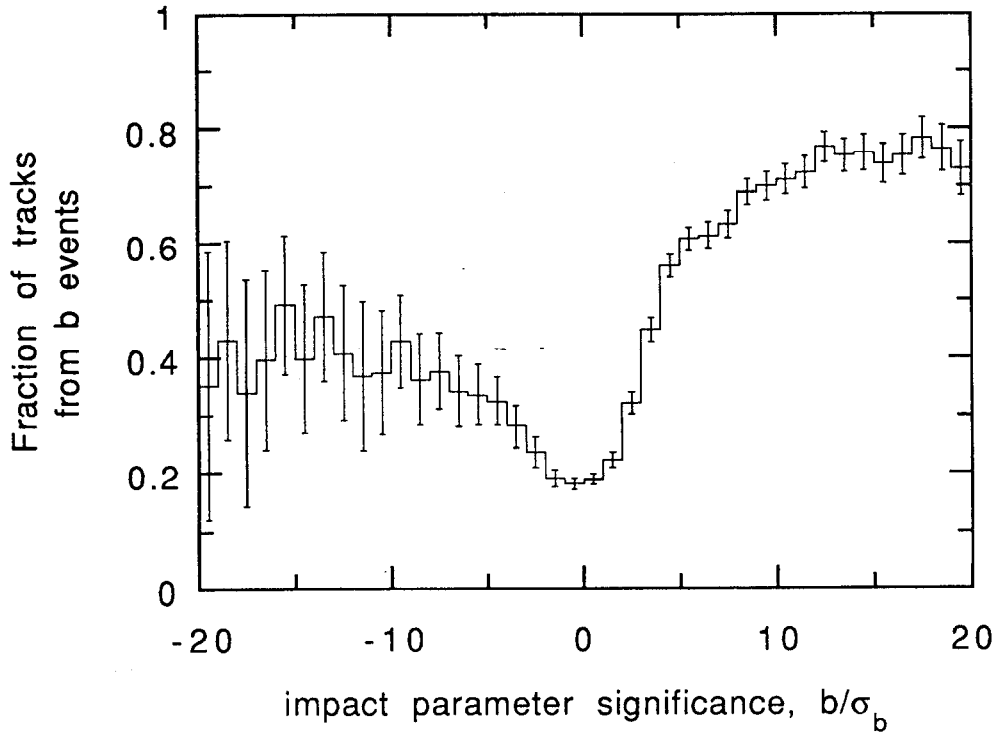

Figure 4–18 Fraction of reconstructed tracks which are from b events as a function of the impact parameter significance.

branching fraction of the Z^0 to $b\bar{b}$ events. This is important because the tracks from B decays will naturally contribute to the impact parameter significance distribution asymmetrically, and the level to which they contribute relative to other presumably symmetric sources can affect the resolution measurement. As F_b is going to be one of the quantities measured in the following analyses, it would also be advantageous for the measured resolution to be insensitive to F_b in order to avoid an iterative solution. It is interesting to note that the reconstructed tracks from $b\bar{b}$ events comprise about 35% of the tracks with large negative impact parameter significance ($b/\sigma_b < -5$), whereas they are only ~23% of the total number of tracks (see Figure 4–18). The level to which the choice of F_b affects the resolution measurement was studied in the Monte Carlo by varying F_b from its nominal value of 0.217 by ±25% and ±50% and repeating the data/Monte Carlo log-likelihood comparison that was used to study the resolution in Section 4.5.1. It is observed that a ±25% variation of F_b does not change the optimal amount of additional required impact parameter smearing (namely 10 μm for all tracks and 100 μm on a random subset of 10% of the tracks) and a ±50% variation changes the optimal smearing within the 1σ allowed region (see Table 4–2 on page 136). Similarly, no

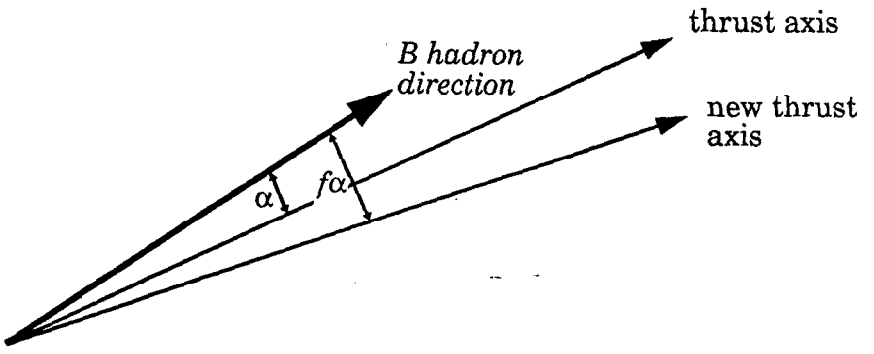

Figure 4–19 Changing the thrust axis by some fixed angular fraction, *f*, from the *B* hadron direction.

change beyond the 1σ region was seen in the amount of far tail impact parameter smearing which is preferred, even with a ±50% change in F_b.

Another mechanism by which the impact parameters can be signed asymmetrically is due to the level at which the thrust axis properly approximates the direction of the *B* hadrons. To investigate this with the Monte Carlo, the angle between the thrust axis and the *B* hadron direction, α, was varied separately for each hemisphere by some fraction, *f*, of the original angle, thus broadening or narrowing the angular distribution (see Figure 4–19). It follows that a value of $f = 1$ leaves the thrust direction unchanged, whereas $f = 0$ causes the *B* hadron direction to be used for signing the track impact parameters. As above, the resulting Monte Carlo impact parameter significance distributions for tracks with $\sigma_{TR} < 25$ μm were then compared to the data and the range of tolerable differences determined using the log-likelihood comparisons as discussed in Section 4.5.1. Table 4–5 shows the results of varying *f* over a broad range, from using the *B* direction to sign the impact parameters to broadening the distribution by a factor of three. The log-likelihood difference is given between the default Monte Carlo thrust axis determination ($f = 1$) and the variously modified thrust axes. The results indicate that the determination of the impact parameter resolution is quite insensitive to how well the thrust axis approximates the *B* direction, as the 1σ range varies almost from the thrust axis perfectly reproducing the *B* direction to the thrust axis approximating the *B* direction twice as poorly as predicted by the Monte Carlo.

It is also possible to generate asymmetric impact parameter distributions for tracks which are scattered or produced in the material of the detectors, through such processes as multiple scattering, pair production, and elastic and inelastic

fractional change in the B-$\hat{T}$ angle (f)	log-likelihood difference $\log(L_{f=1}) - \log(L_f)$
0	0.54
0.5	0.14
1.0	0
1.5	0.10
2.0	0.29
3.0	0.70

Table 4–5 The sensitivity of the resolution determination to the level at which the thrust axis reproduces the *B* hadron direction, given in terms of a log-likelihood comparison of the Monte Carlo with various *B* direction/thrust axis distributions and the data.

nuclear scattering.[73] The mechanism by which these asymmetric tails develop is illustrated in Figure 4–20. Looking along the direction of the track, the half of the scatters that go to the left of the original track (region I) will all be assigned a positive impact parameter according to the algorithm for applying a sign to the impact parameter as described in Section 4.1.2.2. The half of the scatters which go to the right of the original track will predominantly be assigned a negative impact parameter (region II). However, when they scatter at a fairly large angle the impact parameter again becomes positive (region III), and it is this region which can cause an asymmetry.

The use of the high precision tracks ($\sigma_{TR} < 25$ μm) to study the resolution minimizes the contributions to the asymmetry from multiple scattering and pair production tracks. The level of asymmetry is also reduced by the 2 mm impact parameter cut, which means that only tracks which are within 2 mm of the thrust axis as they pass through the scattering material can contribute. For $\sigma_{TR} < 25$ μm tracks, about 49% of the tracks fall within 2 mm of the thrust axis at the radius of the first scatterer, the beam pipe (25 mm). To gauge the level of this effect, note that only 1.7% of all high precision tracks cross the thrust axis beyond 25 mm from the IP.* For better clarity, a cut is used to remove tracks too near the thrust axis, as the angular resolution of these tracks can cause them to cross the thrust axis far from

* In just this one case are the positive impact parameter tracks used in this study of resolution, and here it is only to qualitatively examine the size of these asymmetric tails and *not* to make any determination of the resolution.

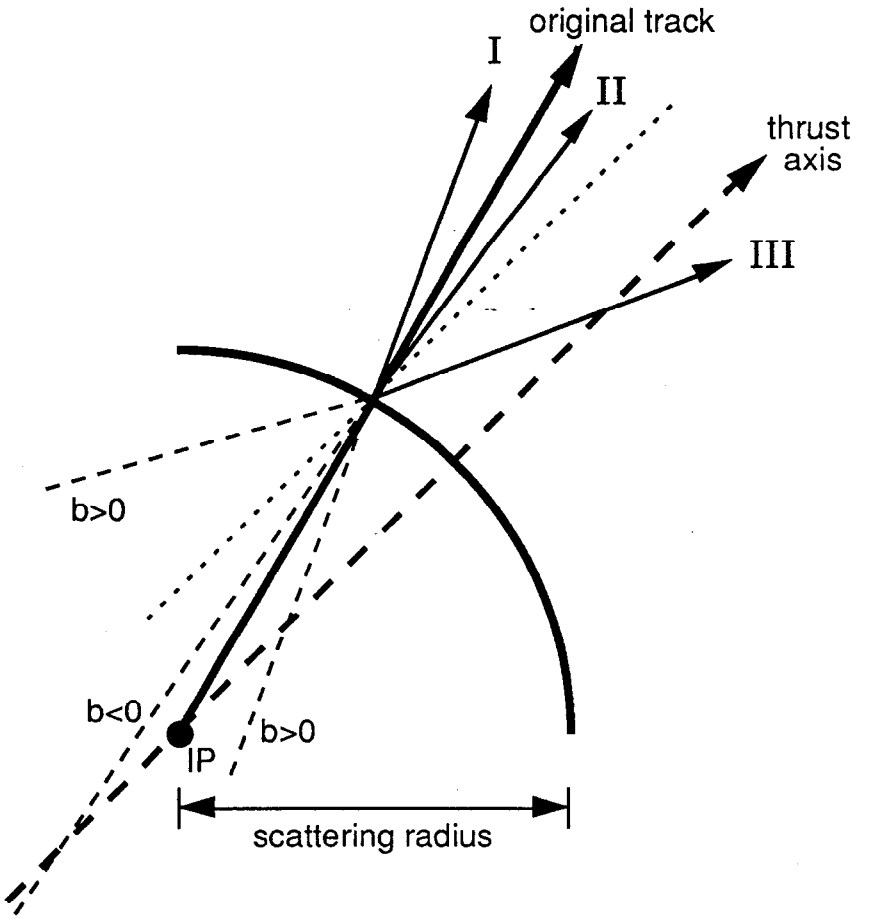

Figure 4–20 The source of an impact parameter sign asymmetry which results from scattering and production mechanisms. The asymmetry will come from region III in which the impact parameter is given a positive sign.

the IP. If a subset of the high precision tracks which fall between 0.15 and 2 mm of the thrust axis at a 25 mm radius are chosen, it is found that now only 2 of these 279 tracks cross the thrust axis beyond a 25 mm radius. The Monte Carlo would predict a consistent value of 1.6 tracks. Finally, even if the impact parameter signing definition is modified to symmetrize tracks from these sources by assigning a negative impact parameter to all of those tracks which cross beyond the beam pipe radius, the resulting optimal impact parameter smearing required for data/ Monte Carlo agreement is unchanged.

4.6 Tracking efficiency

The track finding efficiency of the CDC has been studied extensively in the past[62] and has been measured to be >99% for isolated tracks at PEP and is

estimated to be >95% efficient for tracks with $p_{xy} > 0.15$ GeV/c in hadronic jets at the SLC (see Section 2.2.2, "The Central Drift Chamber," on page 36). The Monte Carlo simulation of the CDC has been tuned to accurately reproduce the hit efficiencies observed in the data and it is believed that within a fiducial volume of $p_{xy} > 0.15$ GeV/c and $|\cos\theta| < 0.8$, the simulation is accurate to within ±1%.

The efficiency with which tracks pass the full vertex quality track cuts (particularly the required number of position measurements in the DCVD and SSVD) is also crucial. As with the CDC, the single hit efficiencies have been tuned in the Monte Carlo to reproduce those observed in the data. In the sample of 196 events which will be used in subsequent analyses, 66.4±1.9% of the 3276 tracks were found by the CDC and passed a set of basic quality cuts: $p_{xy} > 0.15$ GeV/c, $|\cos\theta| < 0.8$, $|z_m| < 15$ mm, $N_{CDC} \geq 25$ and $|b| < 15$ mm.* Of these, 2176 tracks pass the remainder of the vertex quality track cuts (see Section 4.4), which require $N_{DCVD} \geq 15$, $N_{SSVD} \geq 1$, $\sigma_{TR} < 200$ μm, and a tighter impact parameter cut, $|b| < 2$ mm. This corresponds to 66.4±1.9% of the CDC quality tracks passing the additional vertex track requirements. The Monte Carlo predicts an efficiency of 68.3% which is consistent with the data. Thus, the limit to which the efficiency is understood and modelled correctly is the sum in quadrature of the contribution from the CDC track finding efficiency and the uncertainty from the additional constraints of the vertex detector cuts, which yields ±2.3%.

As a check, another way to place limits on the track finding efficiency is by using the well-measured average total charged multiplicity from the Mark II[113] and the four LEP[114][115][116][117] experiments. The average of these multiplicity measurements is 20.94±0.20 tracks per event. The efficiency is measured for two cases,

1. vertex quality track cuts, and
2. CDC only track cuts, as described above.

In order to use the world average measurement of the multiplicity, the reconstructed multiplicity measured in each case must be corrected to the equivalent produced multiplicity using constants determined by the Monte Carlo. Table 4–6 shows the measured and corrected multiplicities for each of the above two cases, and in each case the corrected multiplicity agrees well with the world average multiplicity. The level to which one can limit the track finding efficiency

* These are essentially the same track cuts as used in the $b\bar{b}$ event multiplicity analysis, where it is particularly important to understand the tracking efficiency. (see Section 7.2.1, "Multiplicity Track Quality Cuts," on page 194).

Track Cuts	measured multiplicity	corrected multiplicity
1. vertex quality	11.10±0.31	20.34±0.57
2. CDC only	16.71±0.35	20.90±0.44
World Average		20.94±0.20

Table 4–6 Measured and corrected multiplicities for tracks which pass the vertex quality cuts and a reduced set of cuts which do not require vertex detector information on the track. The corrections applied to our measured multiplicities use the same convention as the world average, so these values can be directly compared. Except for the world average, the errors are statistical only.

using these results depends on the uncertainty in the world average (1.0%) and the uncertainty in the measured multiplicity (2.1% for the CDC only track cuts, and 2.8% for the vertex quality track cuts). Thus the uncertainty can be measured to an accuracy of 2.3% for the CDC only cuts and 2.9% for the vertex quality track cuts. That our corrected values are within these tolerances indicate that our tracking efficiency is indeed correct as modelled by the single hit efficiencies in the Monte Carlo.

4.7 Average Interaction Point

As mentioned in Section 4.2, one can either use an interaction point which is determined for each event separately, as is done in the preceding impact parameter resolution analysis, or use an interaction point which is the average over a series of events. The former approach is used in the majority of this analysis, but use of an average IP provides a useful check.

To determine the average interaction point in the data, only a subset of the events will be used. These events are selected as those with a particularly good vertex fit. To implement this, only tracks which pass the vertex quality cuts (see Section 4.4) are considered when forming the vertex. Then the resulting vertex is required to have:

1. at least 7 vertex quality tracks in the vertex;
2. at least 70% of all vertex quality tracks in the vertex; and
3. a minor axis of the vertex error ellipse of less than 20 μm.

These cuts reject the $b\bar{b}$ events more substantially than *udsc* events, thus reducing the uncertainty from the multi-vertex nature of $b\bar{b}$ events. The Monte Carlo predicts that 84% and 77% of *uds* and $c\bar{c}$ events which passed the event selection cuts will have a vertex fit which meets these criteria, whereas only 44% of $b\bar{b}$ events pass.

The average IP position is then determined for the Z^0 data using the fit vertex position (x_{fit}, y_{fit}) by finding the quantities c_x and c_y which center distributions of

$$(x_{fit} - x_{SLC} - c_x)/\sigma_{x,fit} \text{ and } (y_{fit} - y_{SLC} - c_y)/\sigma_{y,fit}.$$

In the above expressions, $\sigma_{x,fit}$ and $\sigma_{y,fit}$ are the projections of the vertex fit error ellipse onto the x and y axes, and the parameters x_{SLC} and y_{SLC} are information from the SLC instrumentation such as the corrector magnets and beam position monitors which provide information regarding relative shifts of the beam position. To investigate the motion of the beam position, one can use the variable y_T which, as discussed in Section 4.2, is the distance from the fit vertex to the nominal IP in the direction perpendicular to the major axis of the ellipse. This distribution for data events in which the vertex has been well fitted according to the above requirements is shown for the data in Figure 4–21. The Gaussian width of this distribution is 26±1.5 μm, and it lacks any significant non-Gaussian tails.

With the additional impact parameter smearing as discussed in previous sections and no motion of the interaction point, the Monte Carlo predicts a y_T distribution of 17 μm in the width. By adding different amounts of Gaussian motion to the beam position in the Monte Carlo, and assuming this motion to be the same in both the x and y directions, it is found that a Gaussian of width 20±3 μm produces a y_T distribution with the same width as that observed in the data. As a check of possible systematic effects which might result from the various cuts imposed in this study, the above analysis was repeated allowing all tracks, not just the vertex quality tracks, to be fit to the vertex. Furthermore, no vertex quality requirements were applied. In this case, an IP smearing of between 16 and 20 μm was found to provide the best data/Monte Carlo agreement, which is in agreement with the above value.

Instead of comparing the displacements of the fit vertices, one can look directly at the impact parameter significance distributions to determine the motion of the interaction point. To do this, the same log-likelihood comparison techniques were employed as were used previously in the study of the impact parameter resolution (see Section 4.5.1 on page 130). Again using the high precision tracks, namely those

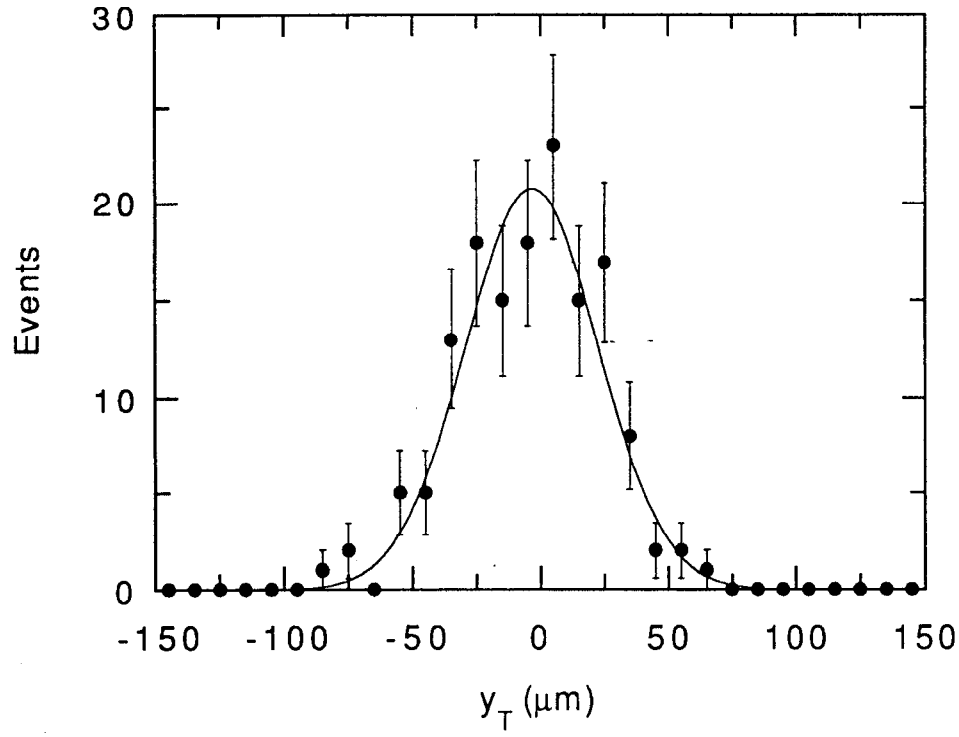

Figure 4–21 The y_T distribution for 145 data events with a well fit vertex (see vertex quality requirements on page 146), and a Gaussian fit to these points. The standard deviation of the data is 28 μm and the fit σ is 26 μm.

with $\sigma_{TR} < 25$ μm, the distribution of b/σ_b observed in the data was compared to the Monte Carlo distribution with different amounts of Gaussian IP motion. The additional impact parameter smearing found necessary in Section 4.5.1 is included in the Monte Carlo impact parameters for this comparison. The data/Monte Carlo comparison indicates that the most favored amount of IP motion is 25 μm and the 1σ and 2σ error on this are ±3 and ±7 μm. The impact parameter significance distributions for the data and the Monte Carlo with no IP motion, and with 25 μm of Gaussian IP motion are shown in Figure 4–22, both for the high precision tracks and the remainder of the tracks, which naturally are less affected by the IP motion.

The two methods of determining the motion of the IP give reasonably consistent results. From studying the y_T distribution it is evident that a Gaussian distribution aptly describes the motion of the IP. Given this, comparing the data and the Monte Carlo distributions of both y_T and b/σ_b demonstrate that a Gaussian distribution with a width of about 20–25 μm adequately describes the observed motion of the interaction point. The uncertainty in the IP motion will be a source of systematic error to measurements which rely on the use of track impact parameters (in the

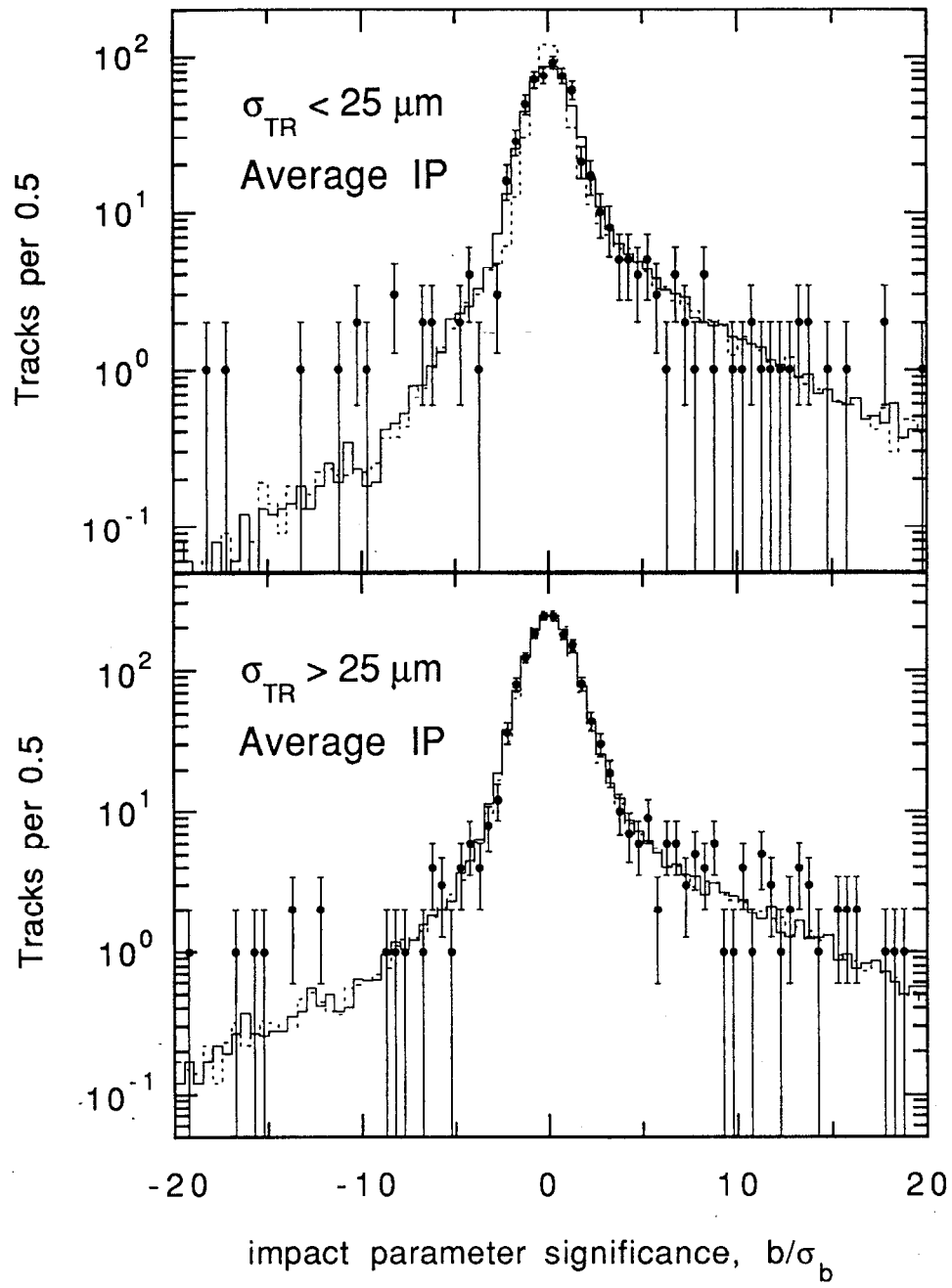

Figure 4–22 Impact parameter significance for the data (points), the Monte Carlo with no IP motion (dashed line) and the Monte Carlo with 25 μm of IP motion (solid line). All Monte Carlo tracks have had their impact parameters smeared by 10 μm for all tracks and 100 μm for 10% of the tracks as discussed in Section 4.5.1.

case of the hadronic branching fraction to $b\bar{b}$ events it would be about ±3%). This can largely be avoided if instead an event-by-event fit vertex is used. In this case, any uncertainties in the primary vertex fitting are accounted for as secondary effects as other sources of error are studied. Furthermore, because the production rate of hadronic events was quite low during the 1990 SLC run, these events are often seperated quite significantly in time. This serves to further reduce the reliability of the of an average IP determination and increase the impetus for the use of an IP determined on an event-by-event basis.

4.8 Tracking System Performance Summary

In this chapter, the performance of the Mark II tracking detector system: the Central Drift Chamber, the Drift Chamber Vertex Detector and the Silicon Strip Vertex Detector, has been evaluated. The Monte Carlo detector simulation has been tuned to reproduce as accurately as possible the observed performance. The parameters of primary importance are the impact parameter resolution and the track finding efficiency.

In studying the impact parameter resolution it was found that even with the detector simulation tuned with the observed single-layer position resolution, the resulting impact parameter resolution of the data is poorer than that of the Monte Carlo. With the small event sample, no systematic source was found which could account for this difference. Consequently, it was decided that to improve the data/ Monte Carlo agreement, the impact parameters of the Monte Carlo tracks should be smeared after the track fitting. The amount of this smearing and its uncertainty was evaluated using the impact parameter significance distribution, as this will be the basic variable used to tag $b\bar{b}$ events as discussed in the next chapter. To minimize the bias of the resolution studies on the resulting measurements, only those tracks with $b < 0$ were used in the resolution study, whereas the tracks of interest, namely those from B decay will primarily have positive impact parameters as a result of signing the impact parameters with the thrust axis.

It must be noted that because this additional impact parameter smearing is applied to tracks on a random basis, it almost certainly is not applied correctly in the sense that no correlations with the unknown source of the degraded resolution could be made. Nonetheless, this is not a major impediment to the subsequent measurements which rely on impact parameter information. This is the case because the correction resulting from this smearing is relatively minor, such that if no smearing were applied, the resulting measurements would change within the

quoted systematic errors. If, however, higher statistics were available, it would be advantageous to reduce the uncertainty associated with the resolution. It is indeed quite possible that the resolution would be better understood with higher statistics, as the search for systematic correlations to explain the degraded resolution was hampered by the small event sample.

The tracking efficiency was also studied and it was determined that the efficiency as modelled in the Monte Carlo appears to be correct to an uncertainty of a few percent. Finally, the position of the interaction was studied and an average interaction point and the motion about this point studied. Using two related techniques, it was found that a Gaussian motion of 20 to 25 μm width appears to adequately describe the motion observed in the data.

Chapter 5

Tagging Bottom Quark Events

This chapter addresses the method used to select a subset of events which is enriched in the fraction of $Z^0 \to b\bar{b}$ events. As discussed in Section 1.4, a number of methods have been used previously, including the most common tag which looks for the high p and p_T leptons from semi-leptonic B decays. With high precision tracking detectors, such as those described in the previous chapter, it is possible to design a fairly simple yet powerful tagging algorithm which is not restricted to the semi-leptonic B decays. In particular, the goal of the tagging algorithm is both to efficiently tag the $Z^0 \to b\bar{b}$ events and to substantially reject $Z^0 \to c\bar{c}$ and $Z^0 \to u\bar{u}, d\bar{d}$, or $s\bar{s}$ events such that the tagged sample will have a high $b\bar{b}$ purity.

5.1 Introduction

In order to tag a sample of events containing a large fraction of B hadrons, one must identify distinctive signatures of these events. Among the possible characteristics of B hadrons, the mean lifetime of ~1.3 picoseconds[102][25] is particularly useful. Furthermore, a bottom-flavored hadron essentially always decays into a charmed hadron,[119] which also has a lifetime between ~0.2 and ~1.0 picoseconds, depending on the particular species.[102] The bottom hadrons from the decay of the Z^0 and the subsequent fragmentation process are produced with a large boost ($\gamma \sim 6$). The mean decay length for the B hadrons is thus about 2 mm. As a consequence of this hard fragmentation, the tracks from B decay will tend to have

both high momentum and because the B hadron is quite massive, a substantial component of this momentum tends to be transverse to the B direction. The result of the long lifetime and the transverse momentum is that the particles resulting from the decay of the B hadrons will have an average impact parameter of about 200 μm. With a tracking system of sufficient resolution, one can then look for these large impact parameter tracks as the signature of the B hadron decay. To account for the accuracy of the impact parameter measurement, which varies widely with the track's momentum, direction and the number of position measurements assigned to the track, the variable used is instead the impact parameter, b, divided by the expected resolution in that quantity, σ_b, which is called the *impact parameter significance*,

$$S \equiv \frac{b}{\sigma_b}. \tag{5-1}$$

A possible tagging algorithm which uses the impact parameter significance for tagging $Z^0 \to b\bar{b}$ events is to require the presence of at least a given number of tracks, n_{min}, either in the entire event or a single jet, which have an impact parameter significance greater than some minimum value, S_{min}. Such a tag was studied in 1984 by K. Hayes.[120] The specific requirements he employed were that there be at least 3 tracks per hemisphere with a minimum significance of 3.0. To further reduce the background from $Z^0 \to c\bar{c}$ events, he also required that the invariant mass of the three or more tagged tracks be at least 1.95 GeV/c^2.

For this analysis, a number of variations of this impact parameter significance algorithm have been investigated, in order to locate that which is optimal for each measurement. As discussed in Chapter 4, the impact parameter resolution is given by the sum in quadrature of three terms:

$$\sigma_b \equiv \sqrt{\sigma_{TR}^2 + \sigma_{IP}^2 + (15\ \mu\text{m})^2}, \tag{5-2}$$

where σ_{TR} is the error due to the track fit as extrapolated back to its distance of closest approach to the IP, and σ_{IP} is the error due to uncertainty in the IP position and the 15 μm is due to the remaining uncertainty in the alignment of the SSVD. With this definition chosen for σ_b, the Monte Carlo prediction of the impact parameter significance distribution for uds, $c\bar{c}$ and $b\bar{b}$ events is shown in Figure 5–1. These distributions were generated with the standard Monte Carlo as described in Chapter 3 and include tracks which passed the vertex track quality cuts (see Section 4.4). It can be seen that the tracks from $b\bar{b}$ events comprise the

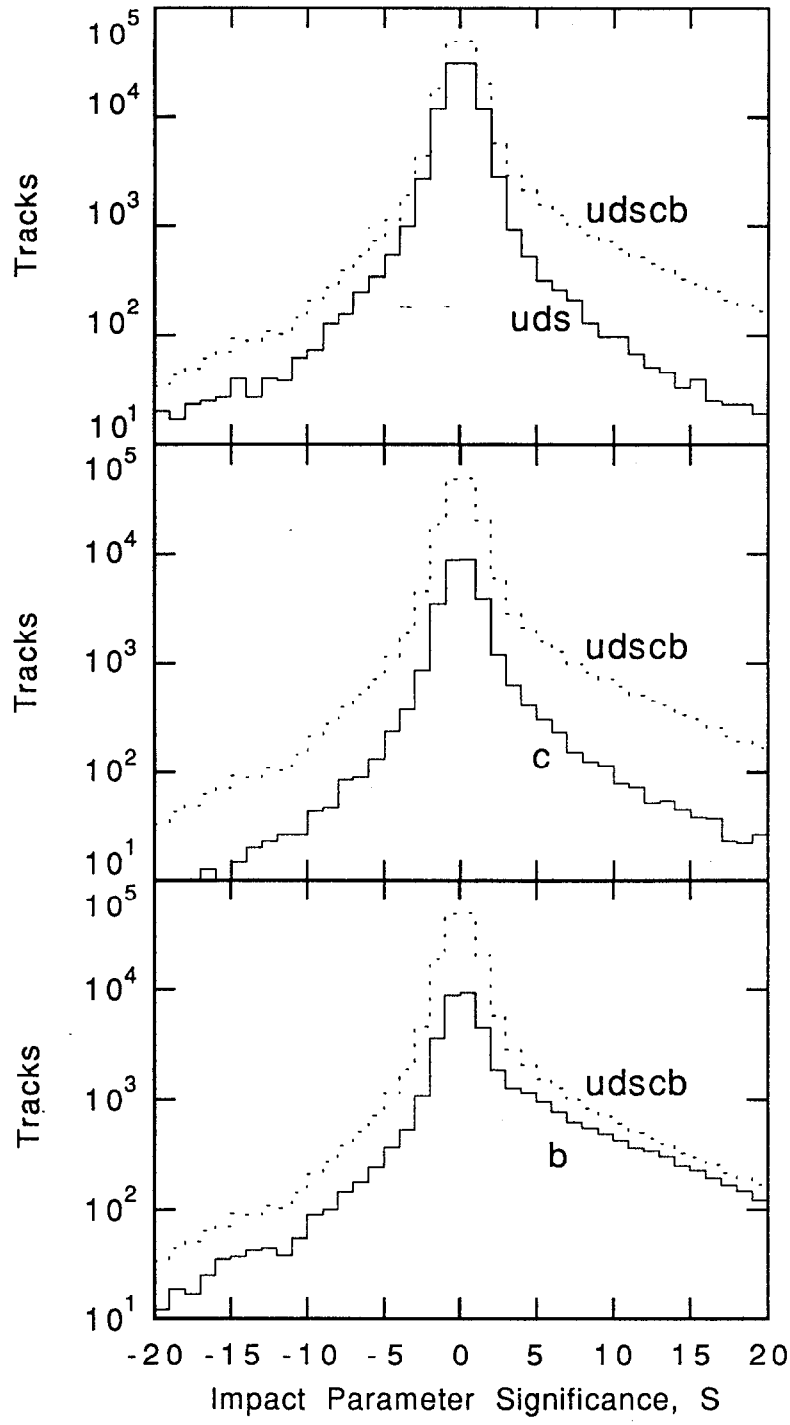

Figure 5–1 Impact parameter significance distributions as predicted by the Monte Carlo for different flavors of events.

majority of the tracks for large values of S. The number of significant tracks (namely those with $S > S_{min}$) per event illustrates the separation of $b\bar{b}$ events which is possible using a tag based on the impact parameter significance, given the resolution of the Mark II tracking detector system. Figure 5–2 shows the distribution of the number of significant tracks per event for a tag with $S_{min} = 3.0$.

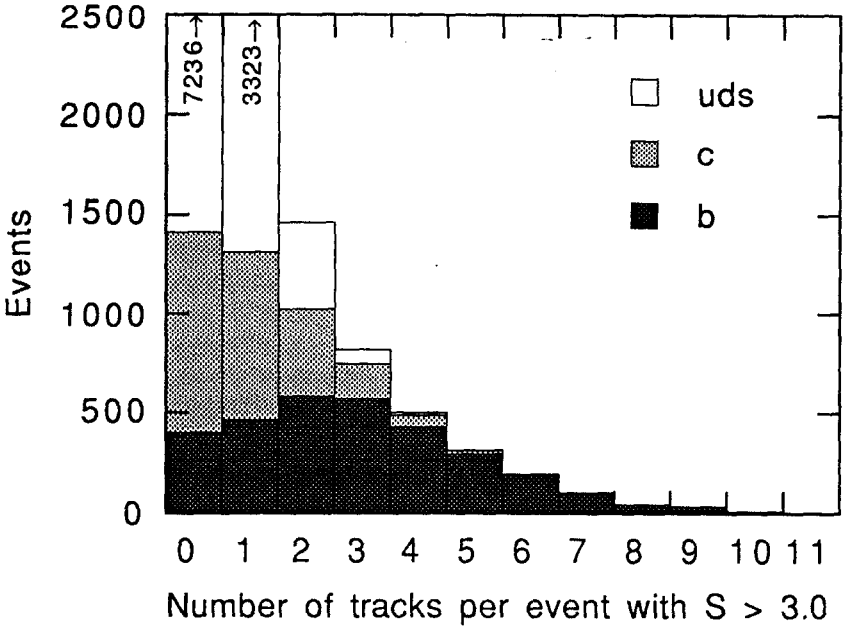

Figure 5–2 The number of significant tracks per event which illustrates the increasing fraction of b events as large numbers of tracks are required. A significant track is defined as one that has passed a minimum impact parameter significance cut, which in this example is S > 3.0.

From this it can be seen that as additional significant tracks per event are required, the events become increasingly dominated by $b\bar{b}$ as expected for the reasons described above.

Clearly one desires a tag which is both efficient in selecting $Z^0 \rightarrow b\bar{b}$ events, yet sufficiently discriminating to reject most other events. We define the efficiency for selecting $b\bar{b}$ events as the ratio of the number of tagged $b\bar{b}$ to the number of $b\bar{b}$ events *after* the hadronic event selection cuts have been applied. (Recall that the

efficiency for these event cuts is ~70%, and this varies only slightly among different flavors of events – see page 158). The $b\bar{b}$ event tagging efficiency is thus,

$$\varepsilon_b = \frac{N_b^{tag}}{h_b \mathrm{F}_b N_{udscb}} \tag{5-3}$$

where,

- N_b^{tag} is the number of tagged $Z^0 \to b\bar{b}$ events,
- N_{udscb} is the total number of produced events,
- h_b is the efficiency of the hadronic event selection cuts for $Z^0 \to b\bar{b}$ events,
- F_b is the $Z^0 \to b\bar{b}$ branching fraction, $\Gamma(Z^0 \to b\bar{b})/\Gamma(Z^0 \to \text{hadrons})$.

Note that in agreement with the above definition of efficiency, the denominator is simply equal to the number of $b\bar{b}$ events which passed the hadronic event selection cuts. Analogously, the efficiency of the tag to select non-$b\bar{b}$ events is

$$\varepsilon_{udsc} = \frac{N_{udsc}^{tag}}{h_{udsc}(1-\mathrm{F}_b)N_{udscb}}. \tag{5-4}$$

The $b\bar{b}$ purity of the tagged sample is then

$$p_b = \frac{N_b^{tag}}{N_b^{tag} + N_{udsc}^{tag}}. \tag{5-5}$$

Note that evaluating the tag $b\bar{b}$ purity necessitates the choice of some value of the $Z^0 \to b\bar{b}$ branching fraction, which is evident when the purity is rewritten in a useful form,

$$p_b = \frac{\varepsilon_b h_b \mathrm{F}_b}{\varepsilon_b h_b \mathrm{F}_b + \varepsilon_{udsc} h_{udsc}(1-\mathrm{F}_b)}. \tag{5-6}$$

While clearly a tag which is more efficient for a given purity (and conversely a tag which is purer for a given efficiency) is more statistically powerful, one must achieve a balance between efficiency and purity, because as the tagging algorithm is tuned for a higher efficiency, the effect is usually to reduce the purity. As will be shown this is in fact the case with the impact parameter significance tag. The optimal tag for a given measurement will however be the tag which yields the lowest possible total statistical and systematic error in the quantity measured. In the case of this analysis, the small data sample essentially simplifies this to finding

the tag with the lowest statistical error. This is addressed separately in the measurement of the $Z^0 \to b\bar{b}$ hadronic branching fraction in Section 6.2 on page 172 and the measurement of the non-leading multiplicity in $Z^0 \to b\bar{b}$ events in Section 7.2.2 on page 195. The remainder of this chapter will give some of the properties of the impact parameter significance tag and compare this tag to other methods.

5.2 Impact Parameter Significance Tag

Starting from the basic impact parameter tag as introduced by K. Hayes, a number of improvements were applied and the resulting tag efficiency and purity analyzed using the Monte Carlo. One of the primary improvements is the use of the physically-signed impact parameter, as described in Section 4.1.2, "Impact Parameter Signing," on page 110. This in and of itself improves the purity substantially as the tracks from light quark events will be spread almost evenly between positive and negative impact parameter while almost all of the tracks from B decay will be assigned a positive impact parameter. Among the broad range of different parameters which were varied in search of improved tag performance, there are

- the minimum track impact parameter significance required (S_{min}) for a track to be considered by the tag;
- the minimum number of significant tracks required (n_{min});
- the choice that the n_{min} tracks be in a single hemisphere, jet or the entire event;
- the use of a mass cut for the jet and hemisphere tags;
- the use of different algorithms to determine the event or jet axes.

A number of different algorithms were investigated for determining the event axis or jet axes, including the thrust axis, sphericity axis, a scaled invariant mass algorithm[101] and a momentum cluster algorithm,[107] as discussed in Section 4.1.2. The difference between these methods, in terms of the tag efficiency and purity was quite small, and when one eventually evaluates the statistical power for a measurement such as the hadronic branching fraction for $Z^0 \to b\bar{b}$, the difference is negligible. The thrust axis is therefore taken as the default.

5.2.1 Event Tags

Using the Monte Carlo with the full detector simulation, including the additional impact parameter resolution degradation found optimal in the previous

chapter the tag efficiencies were calculated. In particular, the event selection cuts and vertex track quality cuts described in Sections 4.3 and 4.4, were applied and tag properties calculated over a range of various S_{min} and n_{min} for *event tags* (namely the n_{min} significant tracks are required in the entire event, not a single jet or hemisphere). The efficiency to select $b\bar{b}$ events and *udsc* events, and the resulting purity of the tagged sample is given in Table 5–1. The purities are calculated using the $b\bar{b}$ tag efficiencies for b and *udsc* events, as well as the Monte Carlo predicted values of the hadronic event selection cut efficiencies, h_b and h_{udsc}, of 0.723±.007 and 0.698±.004 respectively, and the Standard Model prediction of 0.217 for the $Z^0 \rightarrow b\bar{b}$ branching fraction.[13] As shown in Figure 5–3, it is useful to view this information graphically by plotting the efficiency versus the purity for each of the different tags. In this type of plot the best tags from a statistical viewpoint are in the upper right corner. Namely, they select $b\bar{b}$ events with high efficiency, yet reject the *udsc* background well enough to produce a tagged event sample of high $b\bar{b}$ purity.

There are two facts which are immediately evident from this plot: there is a trade-off between achieving high efficiency and high purity. Also, the results from tags requiring different S_{min} and N_{min} primarily tend to fall within a fairly narrow band from high efficiency/low purity to low efficiency/high purity, indicating that they are using the available impact parameter information about equally well. The tag with $S_{min} > 1.0$ does significantly worse than the other tags, as it causes too many *udsc* events to be selected because this low significance cut is well into the central core of the impact parameter significance distribution. Among the other tags, those with a significance requirement of 3.0 or 4.0 appear to perform slightly better than either lower or high significance requirements in terms of achieving both high efficiency and purity.

5.2.2 Hemisphere Tags

One can also apply an impact parameter tag using only tracks in a single thrust hemisphere. A tag which requires that the minimum number of significant tracks be in one of the hemispheres will be referred to as the *hemisphere tag*. A useful feature of this tag is that it leaves the hemisphere opposite the tagged hemisphere unbiased. This facilitates its use in further analyses, such as the B lifetime or the $b\bar{b}$ event multiplicity, the latter of which is discussed in Chapter 7. If instead this is used simply to count events (as is the case in the measurement of the $b\bar{b}$ branching fraction), an event is considered tagged if *either* of the hemispheres are tagged. One

Event Tags		S_{min} 1.0	2.0	3.0	4.0	5.0
		tag efficiency for b events				
	1	0.956±.004	0.913.±005	0.877±.006	0.838±.007	0.793±.007
	2	0.905±.005	0.798±.007	0.723±.008	0.657±.008	0.580±.009
	3	0.822±.007	0.650±.008	0.542±.009	0.456±.009	0.385±.009
	4	0.704±.008	0.479±.008	0.364±.009	0.290±.008	0.224±.007
	5	0.543±.009	0.310±.008	0.222±.007	0.170±.007	0.122±.006
	6	0.402±.009	0.193±.007	0.124±.006	0.085±.005	0.055±.004
		tag efficiency for *udsc* events				
	1	0.860±.003	0.543±.005	0.369±.005	0.290±.004	0.235±.004
	2	0.640±.005	0.226±.004	0.111±.003	0.068±.002	0.047±.002
n_{min} per event	3	0.410±.005	0.080±.003	0.030±.002	0.017±.001	0.010±.001
	4	0.225±.004	0.027±.002	0.007±.001	0.004±.001	0.002±.000
	5	0.110±.003	0.008±.001	0.002±.000	0.001±.000	0.000±.000
	6	0.051±.001	0.002±.000	0.000±.000	0.000±.000	0.000±.000
		b purity of the tagged sample				
	1	0.242±.004	0.326±.005	0.406±.006	0.453±.007	0.492±.007
	2	0.289±.005	0.501±.007	0.653±.008	0.735±.008	0.780±.009
	3	0.365±.006	0.700±.008	0.841±.008	0.885±.008	0.917.007
	4	0.473±.007	0.836±.009	0.937±.007	0.954±.007	0.970±.006
	5	0.586±.009	0.918±.008	0.970±.006	0.980±.005	1.000±.000
	6	0.694±.011	0.965±.006	1.000±.000	1.000±.000	1.000±.000

Table 5–1 Event tag efficiency to tag a b event, a *udsc* event and the b purity of the resulting sample, as calculated by the Monte Carlo. (The associated errors are the statistical errors from the Monte Carlo). The efficiency for tagging a c event is greater than that for a *uds* event, with the factor varying widely depending on the restrictiveness of the tag. For example, the tag which requires at least 3 tracks with a minimum significance of 3.0 has a c (*uds*) efficiency of 0.098 (0.009).

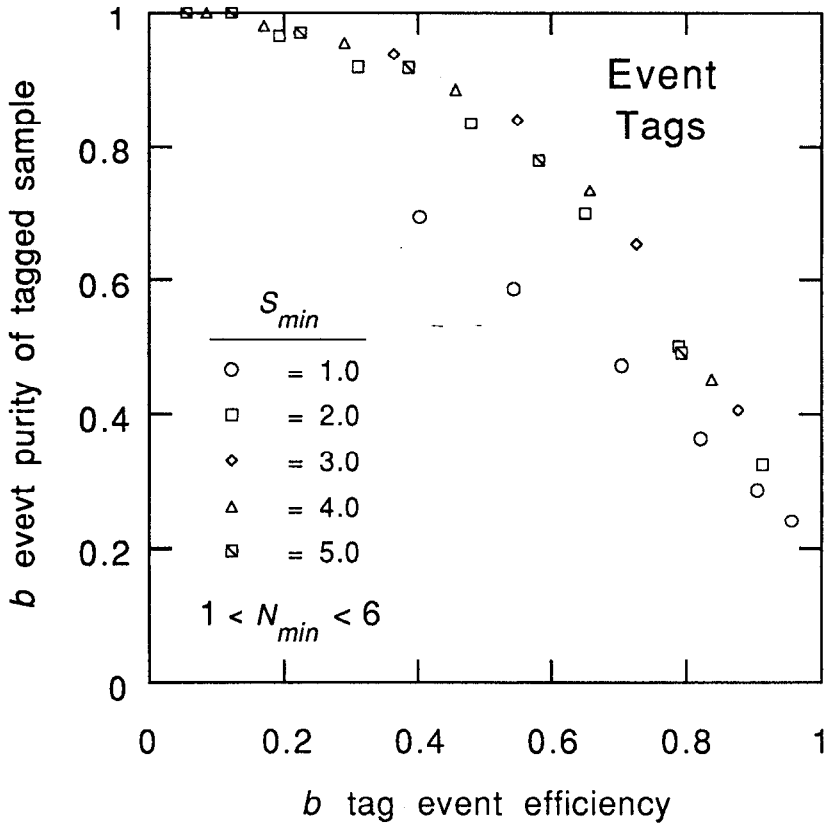

Figure 5–3 The b purity is plotted versus the b efficiency for event tags with a range of S_{min} and N_{min}. For a given S_{min}, there are six entries with different N_{min}, which go from the 1 to 6 from the left to right. These points represent data from Table 5–1.

must note that there are two possible definitions of efficiency for a hemisphere tag: the efficiency to tag a hemisphere, ε_i^{hem}, or the efficiency to tag an event as containing at least one tagged hemisphere, ε_i, where i is the initial quark flavor of the event. If the two hemispheres in an event are assumed to have uncorrelated probabilities of being tagged, then these efficiencies are related by

$$\varepsilon_i = 2\varepsilon_i^{hem} - (\varepsilon_i^{hem})^2. \tag{5-7}$$

Table 5–2 gives the event efficiencies (ε_b and ε_{udsc}) and purities for various hemisphere tags as calculated by Monte Carlo, and Figure 5–4 shows these graphically. From these it can be seen that the hemisphere tags have efficiencies and purities similar in performance to the event tags, and again in the central region, the tags with a significance requirement of 3.0 or 4.0 appear to be superior to either higher or lower significance cuts.

Hemisphere Tags		S_{min} 1.0	2.0	3.0	4.0	5.0
		tag efficiency for b events				
	1	0.956±.004	0.913.±005	0.877±.006	0.838±.007	0.793±.007
	2	0.864±.006	0.740±.008	0.660±.008	0.590±.009	0.516±.009
	3	0.683±.008	0.483±.009	0.391±.009	0.315±.008	0.264±.008
		tag efficiency for *udsc* events				
n_{min} per hemi-sphere	1	0.860±.003	0.543±.005	0.369±.005	0.290±.004	0.235±.004
	2	0.529±.005	0.161±.004	0.062±.002	0.049±.002	0.035±.002
	3	0.231±.004	0.036±.002	0.014±.001	0.008±.001	0.005±.001
		b purity of the tagged sample				
	1	0.242±.004	0.326±.005	0.406±.006	0.453±.007	0.492±.007
	2	0.319±.005	0.569±.008	0.753±.008	0.776±.008	0.809±.009
	3	0.459±.007	0.794±.009	0.889±.008	0.919±.008	0.938±.008

Table 5–2 Hemisphere tag efficiency to tag a b event, a *udsc* event and the b purity of the resulting sample, as calculated by the Monte Carlo. These efficiencies to tag the event by having tagged either of its two hemispheres can be related to the efficiency to tag any given hemisphere by Equation (5-7). (The associated errors are the statistical errors from the Monte Carlo).

As pointed out in K. Hayes' memo, a cut on the invariant mass of the significant tracks in a hemisphere of 1.95 GeV can significantly reduce the background from $c\bar{c}$ events. These events comprise 64% (76%) of the non-$b\bar{b}$ events tagged requiring at least 2 (3) tracks per hemisphere with a minimum significance of 3.0. The efficiencies and purities for these two tags are shown in Figure 5–3. While these cuts do reduce the background, the effect is such a large reduction in the efficiency that a restrictive tag without the mass cut can achieve similar purities, but with better efficiency. Consequently, tags with a mass cut are not pursued further.

5.2.3 Measuring Efficiency with Double Tagging

An advantage of the hemisphere tag as compared to the event tag is that it is possible to *measure* the $b\bar{b}$ tagging efficiency using a double tag technique instead

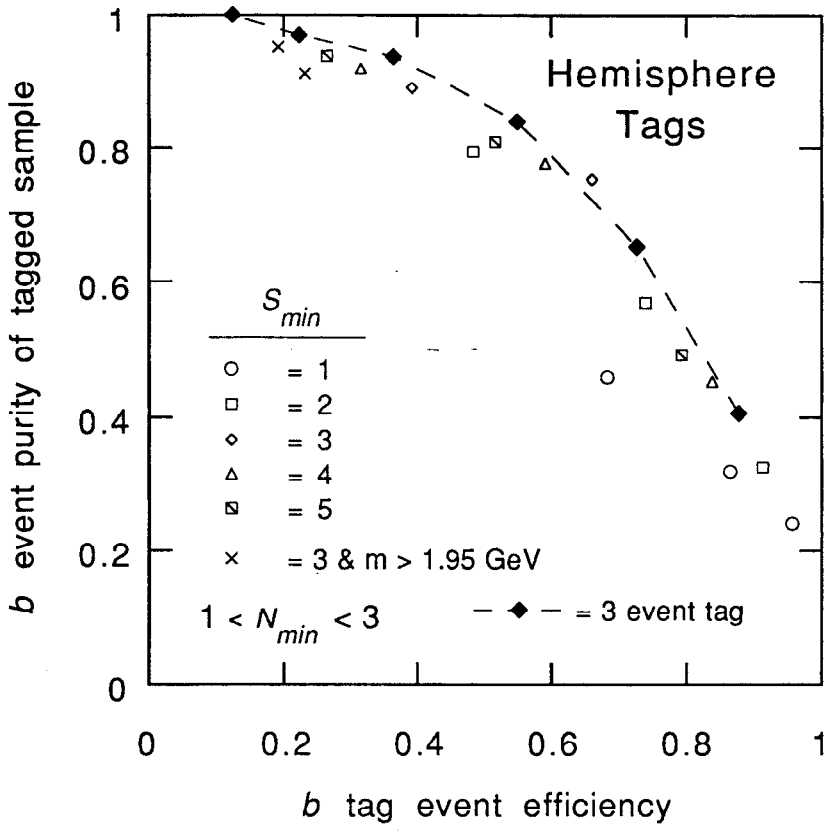

Figure 5–4 The b efficiency is plotted versus the b purity for tagging events by requiring that either hemisphere in the event be tagged with N_{min} tracks of significance S_{min} and N_{min}. For comparison, the event tags with $S_{min} = 3$ is also shown. With the exception of the points with the invariant mass cut, this data is from Table 5–1.

of relying on a Monte Carlo estimate. This involves applying the tag to one hemisphere per event, then applying it again to the opposite hemisphere in events which had a hemisphere tagged in the first pass. In an ideal case in which no *udsc* hemispheres are tagged, the $b\bar{b}$ efficiency is simply

$$\varepsilon_{2b}^{hem} = \frac{N_{2tag}^{hem}}{N_{1tag}^{hem}} \tag{5-8}$$

where N_{1tag}^{hem} and N_{2tag}^{hem} are the number of hemispheres tagged on the first and second passes, respectively.

Of course any tag will have some *udsc* component, and this complicates the situation a bit. In that case, it can be shown that

$$\varepsilon_{2b}^{hem} = \frac{N_{2tag}^{hem}}{N_{1tag}^{hem}} \cdot \left[\frac{1}{2p_{1b}^{hem}} \left(1 + \sqrt{1 - \frac{4\varepsilon_{2udsc}^{hem} p_{1b}^{hem} (1 - p_{1b}^{hem})}{N_{2tag}^{hem} / N_{1tag}^{hem}}} \right) \right] \tag{5-9}$$

where p_{1b}^{hem} is the $b\bar{b}$ purity of the hemispheres tagged on the first pass and $\varepsilon_{2udsc}^{hem}$ is the *udsc* hemisphere tag efficiency of the tag used in the second pass, namely the tag for which ε_{2b}^{hem} is to be determined. (Note that it is not required that the tags used in the two passes be the same). For the hemisphere tag requiring at least 2 (3) tracks on the first pass and at least 2 tracks with a minimum significance of 3.0 on the second pass, the correction term in square brackets is about 1.3 (1.1). Although the correction term is not of a particularly transparent form, it can be seen that in the limit $p_{1b}^{hem} \to 1$, namely no *udsc* hemispheres are tagged by the first pass tag, Equation (5-8) is recovered.

That the size of the correction term can be reduced with a higher tag purity in the first pass implies using a tag of very good purity for that pass, so as to minimize the sensitivity of the efficiency determination on the Monte Carlo estimated values of p_{1b}^{hem} and $\varepsilon_{2udsc}^{hem}$. However, as shown previously, raising the purity is usually done at the cost of lower efficiency. Thus, if limited statistics are a concern, a balance must be achieved between the reliance on statistical power and sensitivity to the Monte Carlo determined constants. The statistical power of the determination of ε_{2b}^{hem} is roughly proportional to $(N_{2tag}^{hem})^{-1/2}$. For our data sample, if we use the hemisphere tag with $S_{min} = 3.0$ and $n_{min} = 2$, 41 hemispheres are tagged on the first pass and only 8 of these are double tagged on the second pass. This corresponds to a statistical uncertainty in ε_{2b}^{hem} of order 35%, which makes this double tag measurement of the hemisphere $b\bar{b}$ tagging efficiency of little value as tighter limits can be placed on ε_{2b}^{hem} using the Monte Carlo with its resulting systematic uncertainties. In the future however, the use of a hemisphere based tag for which the $b\bar{b}$ efficiency is measured holds significant promise for reducing systematic errors.

5.2.4 Tag Dependence on Properties of *B* Hadrons from *Z* Decay

It is interesting to investigate the dependence of the impact parameter significance tag on the various properties of the B hadron. Some of these are illustrated in Figure 5–5, in which the efficiency to tag the hemisphere containing

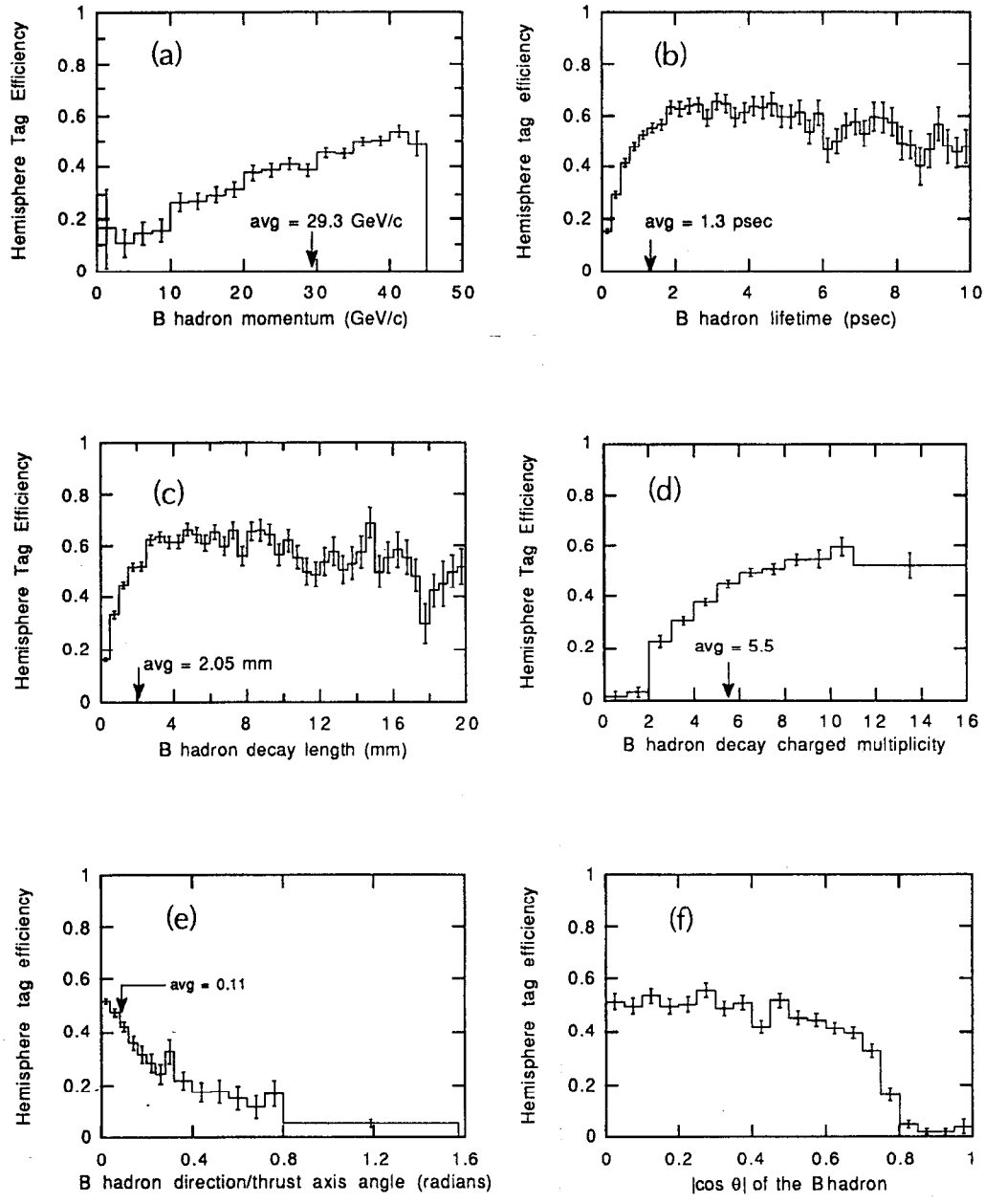

Figure 5–5 The Monte Carlo predictions of hemisphere b tagging efficiencies as a function of several variables related to the produced B hadron. The hemisphere tag efficiencies were calculated for a tag requiring at least 2 tracks per hemisphere with an impact parameter significance of at least 3.0 and only events which pass the event selection cuts were considered. The average b efficiency for this tag is 0.424.

the B hadron in question is plotted versus the property of that hadron. The tag used was to require at least 2 tracks per hemisphere of significance $b/\sigma_b > 3.0$.

As one might expect, the tagging efficiency increases with higher B hadron momentum. This dependence is illustrated in Figure 5–5(a). This is, in part, a consequence of the fact that the impact parameters of the tracks from B decay depend on the B momentum (albeit weakly once the B has a large boost). Compounding this is the use of the impact parameter significance which depends on the impact parameter resolution, σ_b. At low momentum σ_b becomes large as a result of multiple scattering, thus reducing the significance of that track.* Another effect which contributes to the poorer efficiency at low B hadron momentum is that these B's are more likely to have had a hard gluon radiate from the b quark during fragmentation. This will tend to reduce the correlation between the B hadron direction and the thrust axis resulting in more tracks with mis-signed impact parameters.

The impact parameter of a track from B decay is linearly dependent on the lifetime of the decaying B hadron (tracks from B-to-D decays have slightly less dependence and is complicated by the particular lifetime of the D and by the angle of the D with respect to the B) and thus one expects a notable dependence of the tagging efficiency on the B lifetime. From Figure 5–5(b) one can see that with the impact parameter resolution of this tracking detector system, the tagging efficiency essentially levels off around one mean B lifetime (about 1.3 picoseconds) and then gradually decreases at very long lifetimes. This decrease is an artifact of the cut which requires that all tracks have impact parameters of less than 2 mm.† The effects due to lifetime and momentum can be viewed together by studying the decay length of the B hadron. Figure 5–5(c) shows that the efficiency has almost reached a plateau by the average decay length of 2 mm. The gradual decline in the tagging efficiency for very large decay lengths is also due to the $|b| < 2$ mm track cut.

The tagging efficiency also depends on the charged multiplicity of the decaying B hadron as shown in Figure 5–5(d). The impact parameter significance tag is most adept at tagging those hemispheres with high B charged multiplicities simply because the probability of having the requisite number of significant tracks increases as more tracks are produced. However, as more particles are produced, the momenta of these particles in the decaying B's rest frame will tend to decrease.

* The dependence of the impact parameter and the impact parameter resolution on the B hadron momentum is discussed in Section 4.1.1, "Impact Parameter Definition," on page 108 and Section 4.1.3.2, "Multiple Scattering Resolution Term," on page 119, respectively.

† The track cuts are described in Section 4.4, "Vertex Quality Track Cuts," on page 128.

Upon boosting these tracks into the laboratory frame, the component of momentum transverse to the B direction will thus be smaller, resulting in smaller impact parameters for these tracks and reducing the probability to tag the hemisphere.

Figure 5–5(e) demonstrates the level to which the thrust axis approximates the actual B direction is also of importance. As discussed in Section 4.1.2 on page 110, the thrust axis approximates the B direction well in a majority of the cases, although there is a long tail, primarily due to events with substantial hard gluon radiation. This will affect the tagging efficiency through incorrect signing of the impact parameter for tracks from B decay. The probability to tag hemispheres in which the B hadron direction is not well approximated by the thrust axis drops very quickly as the angle between the thrust axis and the B hadron direction increases.

Finally, the tag efficiency is shown as a function of the polar angle in Figure 5–5(f). The efficiency is flat in the central region of the detector and falls off at large $\cos\theta$, primarily because of the event cut which requires that the thrust axis have a $\cos\theta$ of less than 0.7.

5.3 Comparison to Other Tagging Methods

Beside the impact parameter significance tag outlined in the previous section, there are other interesting ideas for tagging $b\bar{b}$ events. A survey of the many variations of tagging algorithms can be found in Chapter 1.

5.3.1 Other Impact Parameter Tags

There are many other possible algorithms for tagging $b\bar{b}$ events using track impact parameters which have different strengths. In particular, one can use the sum of the impact parameters or impact parameter significance as a signal for studying $b\bar{b}$ events. If a sum of impact parameters is made for all of the tracks in an event, it has the desirable characteristic that it will on average be insensitive to uncertainty of the interaction point location which is used to calculate the impact parameters. Varying the IP location along the event axis will simultaneously increase the impact parameters of tracks in one event hemisphere while decreasing the impact parameters in the other. Similarly, moving the IP in a direction perpendicular to the event axis also results in an average cancellation among tracks on each side of the event axis. The disadvantage of a sum of impact parameters is that low momentum tracks can unduly affect the sum. If instead one sums the impact parameter significance, this problem is corrected and some of the insensitivity to the IP location remains. Using either of these sums, or modifications

of them, one can extract information about $b\bar{b}$ events either by tagging them with a requirement that the sum be greater than some threshold cut or fitting the resulting distribution of the sums for all events. The latter provides a more powerful approach for a number of reasons as described below.

B. Schumm has done a detailed analysis along these lines.[121] In this approach, the variable which is calculated for each event is

$$\frac{1}{\sqrt{N}} \sum_{tracks} \frac{b}{\sigma_b}$$

where N is the number of tracks which pass track quality cuts that require they be well measured in the DCVD and SSVD. The factor of $1/\sqrt{N}$ accounts for the statistical uncertainty in the sum due to the number of tracks that pass the track quality cuts, which varies as the square-root of the number of tracks in the sum. It should also be noted that in order to reduce the effects from mis-measured tracks, the tracks with the largest absolute value of the impact parameter was excluded from the sum. The distribution of this variable was then fit to a form which included separate terms for *uds*, $c\bar{c}$ and $b\bar{b}$ events. These were Gaussian terms of the same width for each flavor of events (to account for the impact parameter resolution) and in the case of the heavy quark events, the Gaussian was convoluted with an exponential term, whose width is different for $c\bar{c}$ and $b\bar{b}$ events. A fit to a form such as this is systematically powerful for the determination of the hadronic branching fraction to bottom quarks, as its free parameters allow variation in the impact parameter resolution (through the width of the Gaussians) and the heavy hadron lifetimes (through the exponential tail width). Studies of the statistical power of this tag however indicate that the impact parameter significance tag as previously discussed is statistically stronger, and thus preferred for use when the total error will be dominated by statistical uncertainty. (The statistical power of the impact parameter significance tag will be discussed in more detail later in Section 6.2 on page 172).

5.3.2 Lepton Tag

The high p and p_T lepton tag has been used recently by groups at the SLC and LEP as discussed in Section 1.4.1 on page 19. Table 5–3 shows the efficiency to tag produced $b\bar{b}$ events* and the tagged sample purity for the lepton tags used in previous measurements of $\mathrm{Br}(Z^0 \to b\bar{b})$. These efficiencies and purities are illustrated in Figure 5–6. The purity of the lepton tagged events is between 62 and 75% while the efficiency if the electron and muon samples are combined is still less

Collaboration	p cut (GeV/c)	p_T cut (GeV/c)	$b\bar{b}$ efficiency	$b\bar{b}$ purity
Mark II (e and μ) [27]	> 2.0	> 1.25	10%	72%
ALEPH (e)[22]	> 3.0	> 2.0	4.6%	75%
ALEPH (μ)[22]	> 3.0	> 2.0	3.7%	71%
L3 (e)[23]	> 3.0	>1 & < 6	3.6%	76.7%
L3 (μ)[23]	> 4.0	>1 & < 6	6.9%	62.7%
OPAL (μ)[24]	> 4.5	> 1.0	5.1%	66%

Table 5–3 Efficiency and purity of the high p and p_T lepton tags used at the SLC and LEP. Note that the Mark II efficiency is higher because it is for a combined electron and muon sample.

than ~11%. At similar purities, the impact parameter significance tag has efficiency in the range 40 to 55%. Of course the lepton tag suffers from a combined semi-leptonic branching ratio of the B hadron to electrons and muons ~22%, which provides an ultimate limit for the lepton tag performance. It should be noted that the efficiency of the lepton tag for tagging semi-leptonic events is ~50%. It is clear that the impact parameter significance tagging algorithm is statistically more powerful than the lepton tags. However, the goal is to minimize the total statistical and systematic error, and when high statistics are available the limiting factors will be systematic considerations.

* Note the efficiency used in this section is different than that used previously. This is the probability to tag events in the sample of *produced* $b\bar{b}$ events, whereas elsewhere the efficiency refers to the probability to tag events in the sample of $b\bar{b}$ events *which pass the event selection cuts*.

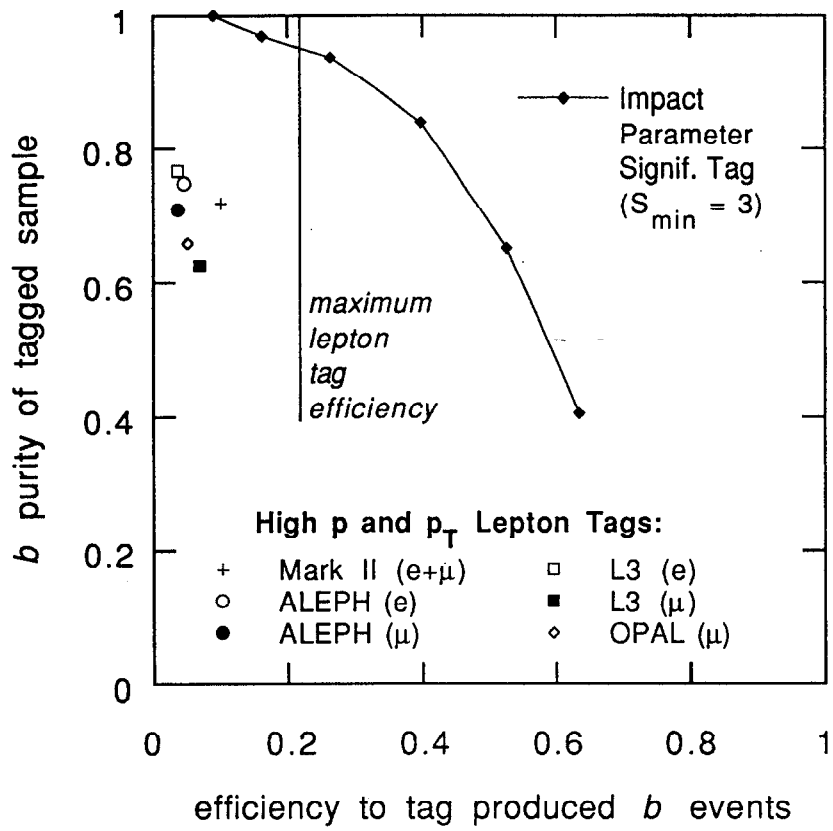

Figure 5–6 Comparison of efficiency and purity for the impact parameter tag and several previously published lepton tags (see Table 5–3). Note that this efficiency is with respect to the number of events *produced*, not the number which pass the event selection cuts as has been used previously.

Chapter 6

The Branching Fraction to Bottom Quarks

The hadronic branching fraction of the Z^0 to bottom quarks is the probability that a Z^0 decayed into a pair of bottom quarks instead of one of the other four flavors of quarks. This branching fraction, F_b, can be expressed as the ratio of partial widths for Z^0 decay,

$$F_b = \frac{\Gamma(Z^0 \to b\bar{b})}{\sum_{q=u,d,s,c,b} \Gamma(Z^0 \to q\bar{q})} , \tag{6-1}$$

assuming that only up, down, strange, charm and bottom quarks are produced in hadronic Z^0 decay. Measurements at LEP have shown that indeed there are only five flavors of quarks. For instance, the total hadronic width of the Z^0 has been measured to be 1.740±0.012 GeV (assuming lepton universality)[122], which is in agreement with the Standard Model prediction of 1.728.[13] As discussed in Chapter 1, this quantity is of theoretical interest first as a check of the Standard Model prediction of the electroweak couplings of the Z^0 to the bottom quarks and with increased precision as an exploratory tool in search of new physics.

6.1 Formalism

The $Z^0 \rightarrow b\bar{b}$ branching fraction can be determined in terms of two observed quantities, the number of events which pass the event selection cuts, N_{evt}, and the number of events which are selected by a particular tag N_{tag}. These quantities are related to the number of produced events, N_{udscb}, by the branching fraction, the efficiencies of the event selection cuts and the tag by the following relations:

$$N_{evt} = N_{udscb}\left[h_{udsc}(1-\mathrm{F}_b) + h_b \mathrm{F}_b\right] \tag{6-2}$$

$$N_{tag} = N_{udscb}\left[\varepsilon_{udsc} h_{udsc}(1-\mathrm{F}_b) + \varepsilon_b h_b \mathrm{F}_b\right]. \tag{6-3}$$

As discussed in the previous chapter, the efficiencies h_{udsc}, h_b, ε_{udsc} and ε_b are determined by the Monte Carlo, so the two unknowns are F_b and N_{udscb}. Solving for F_b yields,

$$\boxed{\mathrm{F}_b = \frac{f_{tag} - \varepsilon_{udsc}}{r_{evt}\varepsilon_b - \varepsilon_{udsc} - (r_{evt}-1) f_{tag}}} \tag{6-4}$$

where $r_{evt} \equiv h_b / h_{udsc}$, and f_{tag} is defined as the fraction of the hadronic cut selected events which are tagged,

$$f_{tag} \equiv \frac{N_{tag}}{N_{evt}}. \tag{6-5}$$

Note that F_b is sensitive only to the ratio of the hadronic event selection efficiencies h_{udsc} and h_b, rather than their absolute values.

6.2 Measurement of $\mathrm{F_b}$

The statistical error is of primary importance, because as will be demonstrated in the following sections, the total error will be dominated by statistical rather than systematic error. This is just a consequence of the small number of events recorded during the 1990 SLC runs. Consequently, the statistical error will guide the choice as to a particular tagging algorithm in an attempt to achieve the smallest possible error.

6.2.1 Statistical Error Formalism

To predict statistical error, we need to ask how the number of tagged events will fluctuate within the sample of events which have passed the event selection cuts. As the events will be divided into two groups, tagged and untagged, the statistical

error in F_b can be estimated using binomial statistics. To do this, first consider the fraction of $Z^0 \rightarrow b\bar{b}$ events in the sample of events which pass the event selection cuts, F_b^{evt}. As can be seen from Equations (6-2) and (6-3), the number of tagged events is related to this by,

$$N_{tag} = N_{evt}\left[\varepsilon_{udsc}(1 - F_b^{evt}) + \varepsilon_b F_b^{evt}\right] \tag{6-6}$$

which using the definition of f_{tag} from Equation (6-5) yields,

$$F_b^{evt} = \frac{f_{tag} - \varepsilon_{udsc}}{\varepsilon_b - \varepsilon_{udsc}}. \tag{6-7}$$

Thus the relative variation in F_b^{evt} as a function of the number of tagged events, N_{tag}, is

$$\frac{\delta F_b^{evt}}{F_b^{evt}} = \frac{f_{tag}}{f_{tag} - \varepsilon_{udsc}}\left(\frac{\delta N_{tag}}{N_{tag}}\right). \tag{6-8}$$

From the variance of the binomial distribution of tagged events, the relative uncertainty in the number of tagged events is

$$\frac{\delta N_{tag}}{N_{tag}} = \frac{1}{\varepsilon_{tag}}\sqrt{\frac{\varepsilon_{tag}(1 - \varepsilon_{tag})}{N_{evt}}}, \tag{6-9}$$

where ε_{tag} is the efficiency to tag any *udscb* event which has passed the event cuts, and is given by

$$\varepsilon_{tag} = \varepsilon_{udsc}(1 - F_b^{evt}) + \varepsilon_b F_b^{evt}. \tag{6-10}$$

Using Equations (6-8) and (6-9), the prediction of the relative statistical error in F_b^{evt} is

$$\left.\frac{\delta F_b^{evt}}{F_b^{evt}}\right|_{stat} = \frac{1}{|\varepsilon_{tag} - \varepsilon_{udsc}|}\sqrt{\frac{\varepsilon_{tag}(1 - \varepsilon_{tag})}{N_{evt}}}, \tag{6-11}$$

where ε_{tag} has been used as the average value for f_{tag}. The fraction of $b\bar{b}$ events in the sample of events which pass the event selection cuts, F_b^{evt}, is related to F_b, the hadronic branching fraction for, $Z^0 \rightarrow b\bar{b}$ as

$$F_b = \frac{F_b^{evt}}{[r_{evt} - (r_{evt} - 1) F_b^{evt}]}, \tag{6-12}$$

yielding a prediction of the relative statistical error of

$$\left.\frac{\delta F_b}{F_b}\right|_{stat} = \frac{r_{evt}}{[r_{evt} - (r_{evt} - 1) F_b^{evt}] |\varepsilon_{tag} - \varepsilon_{udsc}|} \sqrt{\frac{\varepsilon_{tag}(1 - \varepsilon_{tag})}{N_{evt}}}. \tag{6-13}$$

To get a qualitative feel for this function, Figure 6–1 shows contours of constant $\delta F_b/F_b$ on a plot of tag efficiency versus purity for an event sample of 196 events. As had been expected the region of the best statistical power is in the upper right hand corner where a tag must have high efficiency and also good purity. In the lower half of the plot the $\delta F_b/F_b$ contours repeat themselves in the opposite order from the region above. This is a region where the tag is essentially working as an anti-tag by efficiently rejecting $b\bar{b}$ events, which in principle could work equally well for measuring F_b. Finally, the bottom region of the plot is unphysical; the upper boundary of that region corresponds, to tagging all *udsc* events for each given $b\bar{b}$ efficiency, and thus the purity can not get any smaller.

As a check of whether this estimate of the statistical error using binomial statistics is indeed valid, a series of independent Monte Carlo 'experiments' were performed, each with the same number of events as in our data sample, and the statistical fluctuations found by the 68.3% bounds on the distribution of F_b calculated for each of the experiments. The upper and lower bounds for the calculated values of F_b were found to be in good agreement with the binomial estimate of the error. Furthermore, the 68.3% bounds exhibited little asymmetry.

6.2.2 Statistical Error Evaluation and Tag Selection

As our event sample is small, the resulting uncertainty in the measurement of F_b will be limited by statistics and thus necessitates choosing a tag of the highest statistical power. Evaluating the statistical error for each of the event and hemisphere impact parameter significance tags discussed in the previous chapter allows selection of the most statistically powerful combination of the minimum significance, S_{min}, and minimum number of significant tracks, n_{min}. The statistical error for each of the different tags is calculated using the Monte Carlo

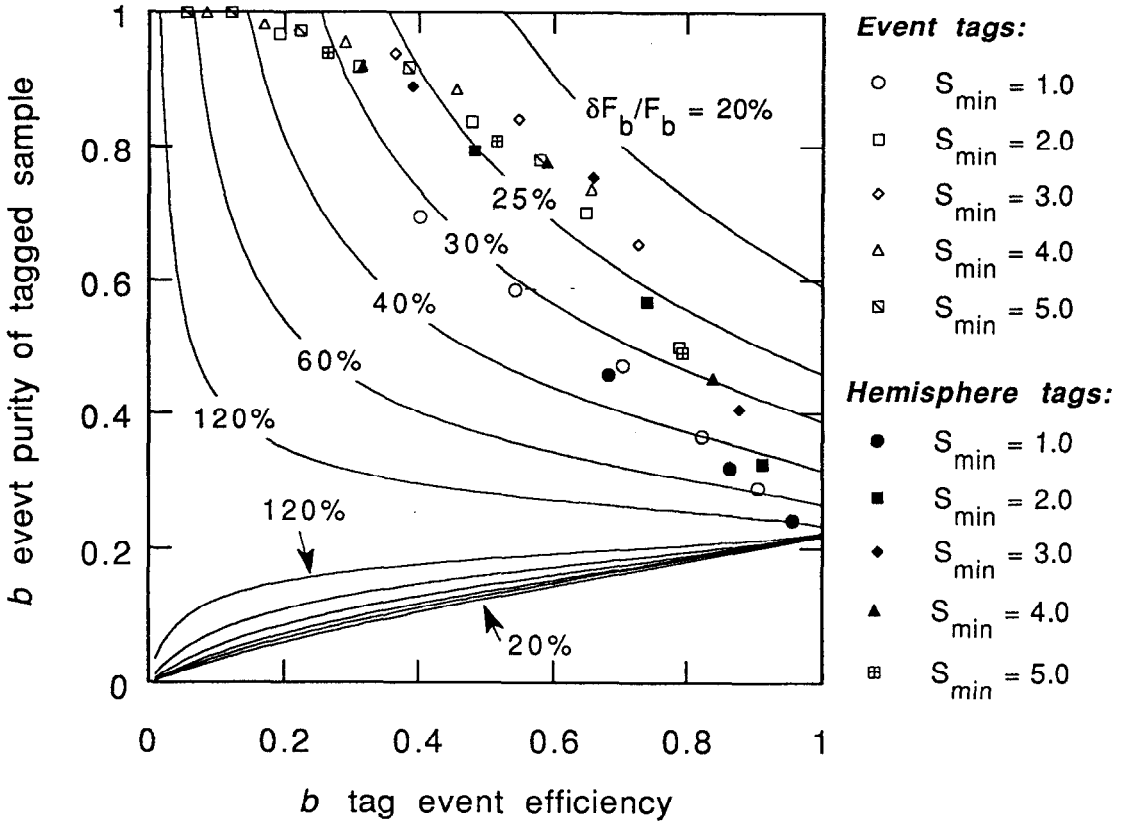

Figure 6–1 Contours of constant statistical error as a function of the b tag efficiency and the purity of the tagged sample assuming 196 events passed the event selection cuts. Also shown are the calculated efficiencies and purities for various event and hemisphere tags, which for a range of S_{min} span n_{min} of 1 to 6 for event tags and 1 to 3 for hemisphere tags. This tag data is from Table 5–1 on page 160 and Table 5–1 on page 160.

predicted efficiencies from Table 5–1 on page 160 and Table 5–1 on page 160, and the ratio for $b\bar{b}$ to $udsc$ hadronic event selection efficiency, r_{evt} = 1.035±0.011, where the uncertainty is the statistical error from the Monte Carlo determination of this value. Figure 6–1 shows the efficiencies and purities for various event and hemisphere tags with the contours of constant statistical error in F_b shown. The specific values of the statistical error for these tags is tabulated in Table 6–1 and Table 6–2 for the event and hemisphere tags, respectively. From these tables it can be seen that there is a fairly shallow minimum for the event tags around S_{min} from 3 to 5, and n_{min} around 2 or 3. Similarly, the minimum for the hemisphere tags is around the same S_{min} and n_{min} values. As the region of minimum statistical error is fairly broad, a tag near the minimum is chosen as the nominal tag. Aside from

Event Tags		S_{min}				
		1.0	2.0	3.0	4.0	5.0
		predicted fractional statistical error in F_b				
n_{min} per event	1	1.08	0.42	0.32	0.29	0.28
	2	0.56	0.27	0.22	0.22	0.22
	3	0.39	0.23	0.22	0.23	0.25
	4	0.31	0.23	0.25	0.28	0.32
	5	0.30	0.28	0.31	0.36	0.42
	6	0.30	0.34	0.42	0.51	0.63

Table 6–1 Event tag fractional statistical error in F_b, as calculated using Equation (6-13). This assumes 196 events pass the event selection cuts and the Standard Model value for F_b.

Hemisphere Tags		S_{min}				
		1.0	2.0	3.0	4.0	5.0
		predicted fractional statistical error in F_b				
n_{min} per hemi-sphere	1	1.08	0.42	0.32	0.29	0.28
	2	0.47	0.25	0.21	0.22	0.23
	3	0.33	.024	0.25	0.27	0.30

Table 6–2 Hemisphere tag fractional statistical error in F_b, using the same assumptions as in Table 6–1.

the requirement that an event pass the event selection cuts, in order to tag the event it is required that it have

> at least 3 tracks per event (n_{min} = 3) with an impact parameter significance of at least 3.0 (S_{min} = 3.0).

where only those tracks which pass the vertex quality track cuts are used.* Some of the other tags will be used in the next section as a systematic check on the resulting F_b calculated with the nominal tag.

6.2.3 Calculation of F_b

Using this nominal tag on the 196 events in the 1990 data sample, 30 of these events are tagged. With the event selection efficiency ratio $r_{evt} = 1.035 \pm 0.011$, and tag efficiencies ε_b and ε_{udsc} of 0.549 ± 0.009 and 0.030 ± 0.002 respectively, the resulting value for the hadronic branching fraction of the Z^0 to bottom quarks, as given by Equation (6-4), is $F_b = 0.234$. The errors on the above efficiencies are the statistical error from their determination by the Monte Carlo.

To evaluate the statistical error on this measurement, we use formalism similar to that developed in the previous sections, where the statistical error was predicted given only the efficiencies and the size of the event sample for each tagging algorithm. With a measured number of tagged events, it is now more rigorously correct to ask "what are the values of F_b which are 1σ allowed given the measured number of tagged events."[118] To evaluate this, Equation (6-2) and Equation (6-3) can be combined to yield an expression for the predicted number of tagged events for an assumed F_b:

$$N_{tag}(F_b;\varepsilon_b,\varepsilon_{udsc},r_{evt}) = N_{evt}\frac{[\varepsilon_{udsc}(1-F_b)+\varepsilon_b r_{evt}F_b]}{[(1-F_b)+r_{evt}F_b]}. \qquad (6\text{-}14)$$

A 1σ statistically-allowed region on a plot of F_b versus N_{tag} is then bounded by $N_{tag}(F_b+\delta F_b)$ and $N_{tag}(F_b-\delta F_b)$ where δF_b is prediction of the statistical error for a given F_b as determined by Equation (6-13). The statistical error on the value of F_b as determined by the number of events tagged is then determined as illustrated in Equation Figure 6–2. Thus the resulting value for the hadronic branching fraction, and its statistical error is

$$F_b = 0.234^{+0.053}_{-0.045}.$$

Systematic effects will be discussed in the next section.

As a check of this result for F_b, it can be compared with results calculated using the impact parameter tagging method except with other combinations of S_{min} and n_{min}. To determine the significance of the difference between F_b calculated with

* See Section 4.3 on page 127 and Section 4.4 on page 128 for more information on the event selection and vertex quality track cuts.

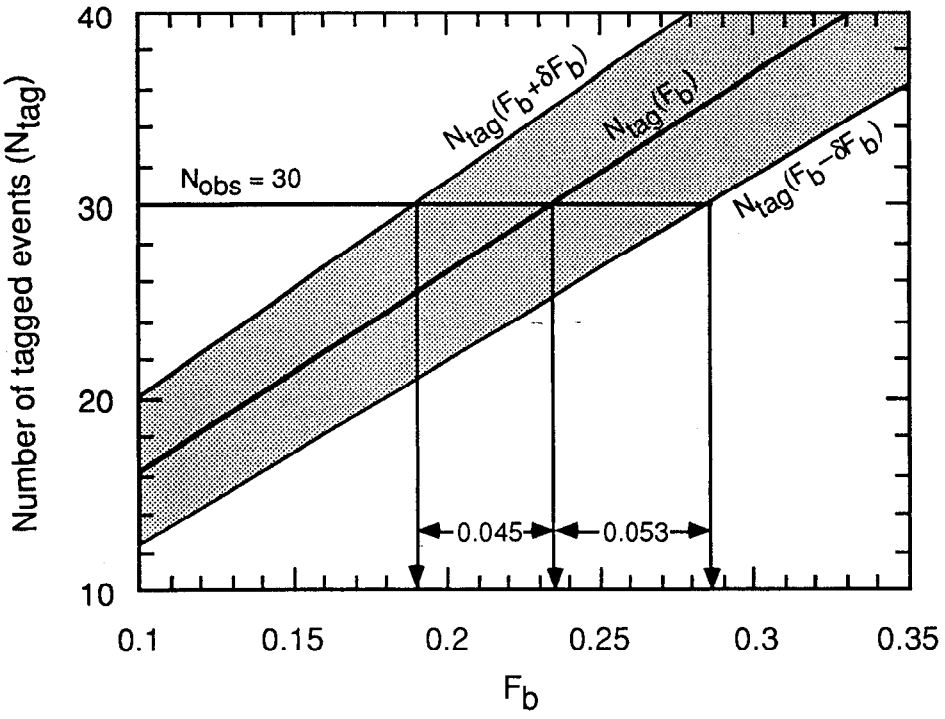

Figure 6–2 Determination of the statistical error in F_b using the nominal tag which selected 30 events. The central diagonal line the relationship between the number of events tagged and the resulting value of F_b as given by Equation (6-4). The shaded area is the 1σ allowed region. The statistical error is determined by finding the values of F_b which are 1σ allowed for the particular measured value of N_{tag}.

the nominal tag and F_b calculated with these other tags, the difference was calculated for 72 independent samples of Monte Carlo data, each with the same number of events as in the actual data sample. The expected difference between the two tags is then the central 68.3% of the distribution of the differences calculated in each MC sample. The differences in the branching fraction as observed in the data using the different tags, and the expected differences are shown in Table 6–3. Of the 14 event and hemisphere tags investigated, only 5 of those are outside of the 1σ of expected difference, and only 1 is beyond 2σ. For a normal distribution, one would expect 4.4 and 0.6 events to be outside the 1σ and 2σ limits, respectively.

Another check is to compare the above value of F_b, which was calculated using an interaction point (IP) determined on an event-by-event basis, with the result using an average IP location as discussed in Section 4.7 on page 146. This is interesting to consider because the IP position will not be not pulled by the presence

Comparison Tag		Number of events tagged	$F_b^{comp} - F_b^{nom}$	
S_{min}	n_{min}		Observed difference	Expected 1σ difference
2.0	2/event	65	–0.049	0.052
2.0	3/event	38	–0.037	0.031
2.0	4/event	27	0.007	0.029
3.0	2/event	48	–0.022	0.036
3.0	4/event	20	0.028	0.030
4.0	2/event	41	0.002	0.030
4.0	3/event	28	0.048	0.021
4.0	4/event	17	0.051	0.040
2.0	2/hemi.	51	–0.065	0.044
2.0	3/hemi.	30	0.024	0.033
3.0	2/hemi.	41	0.008	0.031
3.0	3/hemi.	22	0.023	0.031
4.0	2/hemi.	36	0.011	0.028
4.0	3/hemi.	21	0.084	0.042

Table 6–3 The number of events tagged for a variety of comparison tags with different S_{min} and n_{min} requirements is given along with the observed and expected difference between F_b as measured with the nominal tag ('*nom*') which requires S_{min} = 3.0 and n_{min} = 3 per event, and a comparison tag ('*comp*'). The 1σ limit on the difference in F_b is from the central 68.3% of the F_b difference calculated in 72 Monte Carlo event samples of the same size as the actual data sample. The *b* and *udsc* efficiencies used to calculate these F_b differences are from Table 5–1 on page 160 and Table 5–1 on page 160 and the ratio of *b* to *udsc* event cut efficiency is r_{evt} = 1.035±0.011.

of a high momentum tracks as is the case when the IP is determined for each event separately. As a consequence, the high precision tracks will tend to have larger impact parameters and thus contribute more significantly to tagging events. The event tagging efficiencies for the average IP tag which requires at least 3 tracks per event with S_{min} = 3.0 are 0.526±0.009 and 0.024±0.001 for $b\bar{b}$ and *udsc* events, respectively. In the 196 events of the data sample, 30 events are tagged by this tag.

Of these, 28 are tagged by the event-by-event IP tag. With these efficiencies, the value for the hadronic branching fraction to $b\bar{b}$ c events is found to be $F_b = 0.250 \pm 0.047$, which is consistent with the event-by-event IP result.

6.3 Systematic Error

The systematic errors in the branching fraction arise from two distinct sources, those which are due to the uncertainties in relevant physical constants and processes (lifetimes, branching fraction, fragmentation, *etc.*), and those which are due to the uncertainty in our understanding of the detectors (impact parameter resolution, efficiencies, *etc.*) In the following, all of the systematic errors are calculate for the nominal $n_{min} = 3$ / $S_{min} = 3.0$ event tag.

6.3.1 Average B Hadron Lifetime

The average lifetime of the produced mixture of different B hadrons, $\tau_{\langle B \rangle}$, has been measured by many experiments. The Particle Data Group average of measurements before 1990 is 1.18±0.11 picoseconds.[8] Subsequent measurements have also been made by the experiments at LEP,[25] which increase the world average to 1.31±0.07 psec. Using this value for placing systematic limits on F_b results in a systematic error of ±1.5% and a correction of +1.5% to F_b in order to account for the value of 1.24 psec used for the average B lifetime in the Monte Carlo. Studies have shown that two effects determine the dependence of the uncertainty in F_b on the uncertainty in $\tau_{\langle B \rangle}$. The first of these is a saturation effect which occurs when a tag becomes very efficient and consequently a change in $\tau_{\langle B \rangle}$ will cause a relatively smaller change in the number of tagged events (see Figure 5–5 on page 165). The other effect is due to tracks from $B \rightarrow D \rightarrow X$, whose impact parameters will be somewhat less affected by changes in $\tau_{\langle B \rangle}$ than will tracks directly from the B decay (whose impact parameter will just be proportional to the B lifetime).

There is also some question about the lifetime difference between different species of B hadrons, as is observed in the D system. By assuming the semi-leptonic partial widths for the charged and neutral B mesons to be the same, CLEO[123] and ARGUS[124] have made indirect measurements of the B lifetime ratio. Most recently[127] they have reported measurements of $[\tau(B^+)/\tau(B^0)] \cdot [f(B^+)/f(B^0)]$ to be 0.89±0.19±0.13 and 1.00±0.18±0.12, respectively, where f is the fraction of each B meson produced at the $\Upsilon(4s)$. A direct measurement has been made at 29 GeV by the Mark II[125] which found $\tau(B^0) = 1.20^{+0.52\ +0.16}_{-0.36\ -0.14}$ psec

Experiment	Method	$\tau_{\langle B \rangle}$ (psec)
Particle Data Group	various	1.18±0.11
ALEPH	high p and p_T e and μ impact parameters	1.29±0.06±0.10
DELPHI	high p and p_T μ and hadronic track impact parameters	1.28±0.10
L3	high p and p_T e and μ impact parameters	1.32±0.08±0.09
OPAL	high p and p_T e and μ impact parameters	1.37±0.07±0.06
OPAL	$J/\psi \rightarrow e^+e^-$, $\mu^+\mu^-$ decay length to vertex	$1.32^{+0.31}_{-0.25}$±0.15
Average		1.31±0.07

Table 6–4 List of the measurements of the average B hadron lifetime. If two errors are quoted, they are statistical and systematic, respectively. If only one error is quoted, it is the total error. The average was made accounting for the common systematics such as uncertainty about charm sector parameters and, when applicable, the physics functions used.

and at LEP by ALEPH[126] which has measured $\tau(B^+)/\tau(B^0) = 0.96^{+0.69}_{-0.44}$. However, E653[127] has measured $\tau(B^+)/\tau(B^0) = 4.0^{+2.9}_{-1.8}$. To investigate the effects of a potential lifetime difference on F_b, consider the case of the largest lifetime difference, in which the lifetimes of all neutral B hadrons are changed to 0.6 psec and that for all charged B hadrons to 2.4 psec. The resulting change in the tagging efficiency for $b\bar{b}$ events is –0.02 which corresponds to a 4% lower measurement of F_b. However, the majority of the above experimental evidence indicates that both the charged and neutral B meson lifetimes are consistent with being the same. Furthermore, because of the large mass of the B, the theoretical expectations are for much lower lifetime differences than the D system.[128] Consequently, the contribution to the systematic error from this source is based on the majority of the measurements that indicate nearly equal lifetimes, and yields <1% variation in F_b.

6.3.2 Charm Hadron Lifetimes

The lifetimes of several different species of charmed hadrons have been well measured, and the average values tabulated by the Particle Data Group.[8] Varying the D^0, $D^{\pm}$, D_s and Λ_c lifetimes within the limits of the Particle Data Group causes a systematic error in F_b of less than 1%.

6.3.3 Bottom Fragmentation

The track impact parameters exhibit a weak dependence on the momentum of the bottom hadron, (see Figure 4–2 on page 110), and thus the tag efficiencies will depend on the mean energy carried away by the bottom hadron during the fragmentation process. This mean energy fraction can be parameterized as $\langle x_E \rangle_b = E_B/E_{beam}$ and has been measured by several groups at LEP. These measurements are summarized in Table 6–5. The average of the measurements is

Experiment	Method	$\langle x_E \rangle_b$
ALEPH[22]	high p and p_T e and μ	$0.67^{+0.04}_{-0.03}$
L3[23]	high p and p_T e and μ	0.686±0.006±0.016
OPAL[24]	high p and p_T μ	0.726±0.007±0.022
Average		0.697±0.017

Table 6–5 The measurement of the energy fraction carried from fragmentation by the B hadron. The errors are statistical and systematic, respectively, if both are given, or the total error if a single value is quoted. Different effects were included by the various collaborations in determining the systematic error and the above error is an attempt to remove common effects.

$\langle x_E \rangle_b = 0.697 \pm 0.017$. Varying $\langle x_E \rangle_b$ over this range corresponds to an error on F_b of ±2%. Furthermore, the standard Monte Carlo used for determining the tagging efficiencies had $\langle x_E \rangle_b = 0.676$ and the Monte Carlo shows that F_b should be lowered by 2.0% in order to correct for the difference between this and the average value from LEP.

The shape of the fragmentation distribution has been measured by L3[23] which has shown that the x_E-distribution can be fit reasonably well to the Peterson functional form. While the rigorously correct variable to use in the Peterson function is z, not x_E,[42][43] the L3 plot implies that the Peterson shape is probably

not a bad choice, and thus no additional systematic error is applied based on the shape of the fragmentation distribution.

6.3.4 Charm Fragmentation

The average energy carried off by charmed hadrons, $\langle x_E \rangle_c$, will affect the *udsc*-event tagging efficiency and thus F_b. The average of 0.515±0.011 is the result of measurements by ALEPH and OPAL (see Table 6–6). Varying $\langle x_E \rangle_c$ over this range introduces a systematic effect of less than 1% in F_b.

Experiment	Method	$\langle x_E \rangle_c$
ALEPH[22]	high p and p_T e and μ	$0.52^{+0.16}_{-0.15}$
ALEPH[94]	$D^{*+} \rightarrow K^-\pi^+\pi^+$	$0.504^{+0.013}_{-0.017} \pm 0.008$
OPAL[95]	$D^{*+} \rightarrow K^-\pi^+\pi^+$	0.52±0.03±0.01
Average		0.515±0.011

Table 6–6 The measurement of the energy fraction carried from fragmentation by the charmed hadron as determined by fitting various momentum spectra. The errors are statistical and systematic, respectively, if both are given, or the total error if a single value is quoted.

6.3.5 Charm Production

The hadronic branching ratio to charm quark pairs, $Br(Z^0 \rightarrow c\bar{c})$ has been well measured using a high p_T lepton tag at ALEPH[22] and a D^* tag at DELPHI[129] and OPAL.[95] The average of these measurements is 0.171±0.029. Varying the fraction of charm events in the MC over this range corresponds to a systematic error in F_b of ±2%.

The ratio of the production of D to D^* mesons is also important as the neutral D^* always decays into a D^0, whereas the charged D^* decays 55±4% of the time into D^0 and the remainder into $D^{\pm}$.[102] Thus, a higher initial production of D^* versus D mesons will change the ratio of D^0 to $D^{\pm}$, and as their lifetimes differ by roughly a factor of 2,[102] the tagging efficiencies of $Z^0 \rightarrow c\bar{c}$ events will also change. ALEPH has measured the production of charm from two exclusive decay channels,[94] and has made some initial estimates of the D to D^* production fraction, but with the limited statistics of reconstruction the exclusive channels and the uncertainties regarding higher mass charm hadrons, this measurement is of little use for placing a systematic limit in the measurement of F_b. To span the entire range of

possibilities, the ratio of D to D^* production was varied from 0 to 100% and this led to an uncertainty in F_b of ±0.4%.

6.3.6 *B* Hadron Decay Properties

As the majority of the exclusive B hadron decay channels remain unmeasured, one must rely on inclusive measurements of tracks from B hadron decays to constrain the properties of these particles in the Monte Carlo. In particular, the momentum and multiplicity distributions of tracks from B decay will effectively constrain hadronic decays. CLEO[130] and ARGUS[131] have measured the mean multiplicity at the $\Upsilon(4s)$ to be 10.81±0.05±0.23 and 10.99±0.06±0.29 respectively. The average of these values taking into account an estimate of the common systematics is 10.88±0.20.* Furthermore, the variance of the multiplicity as measured by CLEO[132] is 2.3±0.2, in agreement with our Monte Carlo, which predicts a value of 2.1. The momentum of tracks from B decay is commonly measured using the variable $x = p_B/m_B$, where m_B is the B hadron mass and p_B is the momentum of the tracks from B decay in the B hadron rest frame. The distribution of x has also been measured by CLEO.[133] While these distributions measured at the $\Upsilon(4s)$ only include the decays of $B_{u,d}$ mesons, the expectation is that B_s should behave very similarly, and even the B baryons, which are expected only to be perhaps 10% of the B hadrons at high energy, are not expected to decay vastly differently. Thus the $\Upsilon(4s)$ B decay data is used to constrain the mixture of B hadrons produced at the Z^0 resonance.

The qualitative effects of these two variables, x and multiplicity, on the impact parameter tag can be easily described. When a track is produced with lower momentum in the rest frame of the B hadron, then when it is boosted into the lab frame, it will tend to have lower momentum transverse to the B direction and hence a smaller impact parameter, b. Furthermore its total momentum will be less which raises the impact parameter error, σ_b. The consequence of both of these effects is to lower the impact parameter significance b/σ_b when the B decay momentum spectrum is softened. By the same argument, a harder B decay momentum spectrum will increase the impact parameter significance. The B decay multiplicity spectrum also affects the results of the impact parameter significance tag, as there will be a larger number of tracks which have the required minimum significance.

* A correction to this $B_{u,d}$ multiplicity to include estimates of the effects from B_s and B baryons can be performed, but the remaining error is essentially unchanged. See Section 7.5, "b Event Total and Non-leading Multiplicities," on page 214 for a detailed discussion of this correction.

Note the B decay momentum distribution and the multiplicity distribution can be varied independently because the fraction of charged energy is not constrained.

To investigate the effects of the x and multiplicity distributions, an event reweighting scheme was used. Events were assigned weights depending on the charged energy fraction of the B hadron decay products (in the rest frame of the B hadron) or the number of tracks from the B decay. In order to vary the x distribution independently of the multiplicity, ad-hoc weighting functions were used. Using this scheme, it is seen that a 2% uncertainty on the mean B decay multiplicity corresponds to a systematic uncertainty of ±1.7% in F_b. To place a limit on the allowable variation in x, the region of very low momentum, $x < 0.04$ is used. This region, which contains about 20% of the tracks, is entirely unconstrained by Reference [133]. However, in order measure the charged multiplicity, CLEO and ARGUS made this extrapolation, and thus the uncertainty on the multiplicity can be used to place a limit on the tracks in this region. This method produces an uncertainty of ±2.9% in F_b.

Finally, the ratio of B hadrons which decay to D^0 or $D^{\pm}$ is also of importance, owing to the very different lifetimes of the charged and neutral charm mesons. CLEO[134] has measured this ratio to be

$$\frac{Br(B \to D^0 X)}{Br(B \to D^{\pm} X)} = 2.3 \pm 0.7.$$

Changing this ratio in the Monte Carlo over the above limit produces an uncertainty of 0.9% in F_b. Adding the above three sources of systematic error in quadrature yields a combined error 3.5% from the uncertainty in the B hadron decay properties.

6.3.7 Total Charged Multiplicity

The total hadronic multiplicity has been well measured at the Z^0 resonance by Mark II[113] and all four LEP[114][115][116][117] experiments. The average of these measurements is $\bar{n}_{had} = 20.94 \pm 0.20$ tracks per event. As the decay multiplicity of the bottom and charm hadrons is fixed in the Monte Carlo generation to the results of independent measurements, any variation in $\bar{n}_{had}$ can be considered to arise from *uds* events and the tracks produced by fragmentation in $b\bar{b}$ or $c\bar{c}$. By reweighting events based upon the number of tracks not from the decay of heavy hadrons, the uncertainty of ±0.20 tracks in the multiplicity corresponds to ±1% in F_b. The Monte Carlo total charged multiplicity is 21.93 tracks per event which is

significantly higher than the world average. Correcting F_b using the same reweighting scheme used to place the systematic limit lowers the measured value of F_b by 1.3%.

6.3.8 Non-hadronic Contamination

The initial Mark II hadronic decay analysis estimated the non-hadronic background to be 0.42 events in the sample of 398 hadronic events.[62] For the 1991 data sample of 196 hadronic events, with slightly more stringent hadronic event selection cuts, this corresponds to a contamination of less than 0.2 events. In the worst possible case, if the non-hadronic events were tagged — which is quite unlikely — it would cause a systematic error of <1% in F_b. and so will be ignored.

6.3.9 Intrinsic Impact Parameter Resolution

In Chapter 4, the impact parameter resolution of the combined tracking system was studied and it was found that additional impact parameter smearing was required in the Monte Carlo in order to reproduce the impact parameter distributions observed in the data. Comparing the data and Monte Carlo led to a choice of an optimal amount of additional smearing as well as 1σ and 2σ allowed regions as shown in Table 4–2 on page 136. The 2σ allowed region is chosen to determine the uncertainty in F_b because of the additional uncertainties regarding the source of the degraded resolution and the potential correlations with track parameters that are not taken into account when adding the additional smearing to the Monte Carlo tracks. Determining the efficiencies for each of these values yields a systematic error in F_b of +9%/–6%. A limited amount of very broad impact parameter smearing (the 'far tail') is also allowed (see Table 4–3 on page 137), and using the 2σ allowed far tail smearing leads to only a –4% variation in F_b.

It is important to mention the affect of the additional impact parameter smearing that was determined necessary in Chapter 4. If this smearing were not added, F_b would be 9.5% higher, which is only ~1σ of the systematic error due to the uncertainty in the impact parameter resolution. Thus adding this additional smearing, though probably the proper approach given the knowledge of the impact parameter resolution, does not alter the determination of F_b beyond its assigned errors.

6.3.10 Multiple Coulomb and Nuclear Scattering

The implementation of multiple Coulomb and nuclear scattering in the Monte Carlo detector simulation is discussed in Section 3.4 on page 102. Systematic

uncertainties can arise due to the imperfect knowledge of the amount and distribution of scattering material in the detectors, as well as the limitations of the models employed in the simulation. For example, the modification of the detector simulation to incorporate the Molière scattering theory significantly improved the accuracy of the simulation compared with the earlier Gaussian-based method. Additionally, although elastic nuclear scattering is modelled in the Monte Carlo, inelastic scattering was modelled only as removing the inelastically scattered track in the default Mark II detector simulation. To investigate the effects of tracks produced by inelastic nuclear scattering, a nuclear interaction generator was written and employed.

To study the amount of material in the detectors and the effects of multiple Coulomb and elastic nuclear scattering from within this material, tracks with extrapolated errors $\sigma_{TR} > 25$ μm were employed. These tracks were chosen because these lower momentum tracks will be more sensitive to multiple scattering effects. The amount of scattering material which most affects the impact parameter resolution, the beam pipe and SSVD, can be constrained using these tracks to ±3% given the available statistics. The material further outside, the DCVD and CDC, is more difficult to study but less important for the impact parameter resolution. Varying the amount of scattering material in the inner scattering layers by ±3% results in a change in F_b of ±1%.

As mentioned above the default Mark II detector simulation did not produce tracks from inelastic nuclear scattering, but instead just terminated the scattered track. A crude nuclear interaction generator was written which was based on data from nuclear scattering experiments.[135] This generator makes conservative assumptions throughout and is intended only to set an upper limit on the effects of these tracks, not to apply a correction. With this generator installed, it is found that an average of approximately 0.04 tracks per event whose origin was an inelastic nuclear interaction passed the vertex quality cuts. Furthermore, only half of these have a significance larger than 3.0 and only 3% of events have more than one nuclear interaction track which passed the vertex track quality cuts. The consequence is that the effect of inelastic nuclear scattering is small, producing an uncertainty in F_b of less than ±1%.

6.3.11 Tracking Efficiency

As discussed in Section 4.6 on page 144, the uncertainty in the track finding efficiency for the vertex quality track cuts is ±2.3%. By adding this amount of

additional tracking uncertainty to the Monte Carlo simulation, it is found that this uncertainty in the tracking efficiency corresponds to an uncertainty in F_b of ±4%.

6.3.12 Monte Carlo Statistics

The determination of the event selection efficiency ratio r_{evt}, and the tagging efficiencies, ε_{udsc} and ε_b, used a Monte Carlo sample of approximately 20,000 hadronic events. The finite size of this sample results in a statistical uncertainty in these efficiencies. The values and their uncertainties from the Monte Carlo efficiency ratio and tagging efficiencies, and their statistical uncertainties are $r_{evt} = 1.035 \pm 0.011$, $\varepsilon_{udsc} = 0.030 \pm 0.002$ and $\varepsilon_b = 0.549 \pm 0.009$, respectively. This corresponds to a systematic error of ±2% in F_b.

6.4 Hadronic Branching Fraction to Bottom Quarks

Table 6–7 shows a summary of the various contributions to the relative systematic error in F_b as described in the preceding sections. Adding these contributions in quadrature yields +11%/–9%. It is interesting to note the sources of the systematic errors. About ±6% is due to uncertainties in various physical measurements, within which the B decay properties and $\mathrm{Br}(Z^0 \to c\bar{c})$ are the largest sources, and it is probable that at least the latter will be reduced by measurements at LEP in the near future. The remainder of the error, +10%/–7%, is due to the uncertainties related to the knowledge of the tracking detector system. As discussed later, this second source of error can be substantially reduced with higher statistics as one is able to study the detectors more thoroughly.

Thus, including the small systematic corrections to correct for the most recent measurements of the total charged multiplicity (+2.0%), the average B hadron lifetime (–1.5%) and $\langle x_E \rangle_b$ (–1.5%), the hadronic branching fraction for $Z^0 \to b\bar{b}$ is measured to be

$$F_b = 0.232^{+0.053}_{-0.045}\ (\mathrm{stat})\ ^{+0.025}_{-0.021}\ (\mathrm{syst}).$$

This value for F_b is, within its uncertainty, in agreement with the Standard Model prediction of 0.217.[13] Comparison can also be made with the various previous measurements of F_b. Table 6–8 shows the previously measured values of F_b and shows an excellent agreement between this measurement and previous measurements, whose average was calculated in Section 1.5 to be 0.212±0.003±0.011.

Source of Systematic Error	Range	Systematic Error on F_b
Physics-related errors:		
average B hadron lifetime	1.24 – 1.38 psec	±2%
charm hadron lifetimes	PDG limits	<1%
b fragmentation	0.680 – 0.714	±2%
c fragmentation	0.504 – 0.526	<1%
$\mathrm{Br}(Z^0 \to c\bar{c})$	0.142 – 0.200	±2%
B decay properties	CLEO & ARGUS data (see text)	±4%
total charged multiplicity	20.74 – 21.14	±1%
Detector-related errors:		
non-hadronic events	<0.1% contamination	<1%
impact parameter resolution	2σ allowed region of b smearing	+9/–6%
multiple scattering	±3%	±1
nuclear scattering	(see page 187)	<1%
tracking efficiency	±2.3%	±4%
Monte Carlo statistics	20,000 MC events	±2%
Total Systematic Error on F_b		+11/–9%

Table 6–7 A summary of the systematic errors on F_b. The sources for each of these limits is given in the relevant section of text.

The impact parameter significance tagging algorithm used in this analysis demonstrates the strength of using a tagging method based on impact parameters as measured by high resolution tracking detectors. In the future, methods such as this should serve as important check on the lepton tag methods, as they are largely independent of the semileptonic B decay branching fraction. Furthermore, it should be possible to significantly reduce the systematic error, particularly as high statistics are available to study the impact parameter resolution of the detectors.

Experiment	F_b
Mark II	$0.23^{+0.10+0.05}_{-0.09-0.04}$
ALEPH	0.220±0.016±0.024
L3*	0.221±0.004±0.012
OPAL*	0.193±0.006±0.015
DELPHI	0.209±0.030±0.031
this measurement	$0.230\pm0.045^{+0.025}_{-0.021}$

Table 6-8 Values for F_b from previous experiments and this measurement. Those marked with an asterisk have been converted from related measurements as described in Section 1.5 on page 22.

Chapter 7

The Multiplicity of Bottom Quark Events

The average charged multiplicity of $Z^0 \to b\bar{b}$ events ($\bar{n}_b$) can be measured by making use of the impact parameter tag to select a sample composed primarily of $b\bar{b}$ events. The primary purpose of this measurement is a qualitative check of QCD phenomenology. Within the framework of QCD, non-leading particle production is governed by gluon fragmentation, triggered by the disruption of the vacuum by the color charge, and thus is expected to be independent of the flavor of the initial quarks. It has been suggested[37][38] that this expectation can be tested by measuring $\bar{n}_b$, subtracting off the well-known average B meson decay multiplicity, and comparing the resulting *non-leading* multiplicity to the multiplicity of e^+e^- annihilation at the center-of-mass energy equal to the average energy available to the non-leading system in $Z^0 \to b\bar{b}$ events, essentially $E_{nl} = E_{cm}(1 - \langle x_E \rangle_b)$. Conversely, if this expectation is taken as a given, then the non-leading multiplicity in $Z^0 \to b\bar{b}$ events may be used to extract $\langle x_E \rangle_b$, the average energy fraction carried off by the hadron system in e^+e^- annihilation.

In this chapter, both approaches are taken. The $b\bar{b}$ event multiplicity is determined by measuring the difference in multiplicity between $b\bar{b}$ and all hadronic events, which significantly reduces the systematic error of the measurement. The multiplicity comparison checking the flavor independence is then made between the non-leading multiplicity and the total multiplicity at a center-of-mass energy equal to E_{nl}. Finally, the flavor independence is assumed and a value for $\langle x_E \rangle_b$ measured.

7.1 Approach and Formalism

In the Mark II measurement of the total hadronic multiplicity at the Z^0,[113] the systematic error was dominated by a contribution of ±0.8 tracks due to uncertainty in the detector efficiency. In this measurement of $\bar{n}_b$, this systematic error is reduced by measuring

$$\delta\bar{n}_b \equiv \bar{n}_b - \bar{n}_{had} \tag{7-1}$$

with our data, and then adding back in the world average $\bar{n}_{had}$, which is now known to about ±0.2 tracks. This also has the effect of reducing the systematic error from several important sources as will be discussed below.

Given a perfectly efficient detector, and a $Z^0 \to b\bar{b}$ tag with sample purity P_t and no multiplicity bias effects, we can write the measured multiplicities of the hadronic events and the tagged subset, ($\bar{m}_{had}$ and $\bar{m}_{tag}$), as

$$\bar{m}_{had} = (1-P_h)\,\bar{n}_{udsc} + P_h\bar{n}_b \tag{7-2}$$

$$\bar{m}_{tag} = (1-P_t)\,\bar{n}_{udsc} + P_t\bar{n}_b \tag{7-3}$$

where P_h is the $b\bar{b}$ purity of the event sample which passed the event selection cuts (see Section 4.3 on page 127), and the $\bar{n}_i$'s are the 'true' average multiplicities for *udsc* and *b* events. As is now standard, we use the following definition of the true charged multiplicity:

> The true multiplicity includes any prompt track or decay product of a parent particle with a mean lifetime less than 3×10^{-10} sec.

Thus, decay products of K_s^0 and Λ are included in the true multiplicity.

In general, there are inefficiencies and biases, so we must introduce *reconstruction constants* $C_{i,j}$ relating the true multiplicities $\bar{n}_i$ to the measured multiplicities $\bar{m}_i$

$$\bar{m}_{had} = C_{h,\,udsc}\,(1-P_h)\,\bar{n}_{udsc} + C_{h,\,b}P_h\bar{n}_b \tag{7-4}$$

$$\bar{m}_{tag} = C_{t,\,udsc}\,(1-P_t)\,\bar{n}_{udsc} + C_{t,\,b}P_t\bar{n}_b. \tag{7-5}$$

However, the B hadron decay multiplicity $\bar{n}_B$ has been independently measured, so the measurement of $\delta\bar{n}_b$ is only sensitive to the size of the non-leading multiplicity $\bar{n}_{nl}$. Since the B decay products are stiffer and more collimated than the non-leading particles, the reconstruction constant $C_{i,b}$ is different for leading and non-

leading particles. Thus, to avoid having $C_{i,b}$ itself depend on $\delta\bar{n}_b$, thereby necessitating an iterative solution for $\delta\bar{n}_b$, the constants $C_{i,b}$ must be broken up into two separate sets of constants $C_{i,B}$ and $C_{i,nl}$, and so

$$\bar{m}_{had} = C_{h,\,udsc}(1-P_h)\bar{n}_{udsc} + C_{h,B}P_h\bar{n}_B + C_{h,nl}P_h\bar{n}_{nl} \tag{7-6}$$

$$\bar{m}_{tag} = C_{t,\,udsc}(1-P_t)\bar{n}_{udsc} + C_{t,B}P_t\bar{n}_B + C_{t,nl}P_t\bar{n}_{nl} \tag{7-7}$$

Finally noting that $\bar{n}_{had} = (1-\mathrm{F}_b)\bar{n}_{udsc} + F_b\bar{n}_b$, we can substitute into Equation (7-1) which yields

$$\delta\bar{n}_b = (1-\mathrm{F}_b)\,(\bar{n}_B + \bar{n}_{nl} - \bar{n}_{udsc}) \tag{7-8}$$

where $\bar{n}_{nl}$ and $\bar{n}_{udsc}$ are the solutions to the above two simultaneous equations. Solving these equations yields

$$\delta\bar{n}_b = \frac{(1-\mathrm{F}_b)}{\eta}\left[\bar{m}_{tag}\chi_{had} - \bar{m}_{had}\chi_{tag} + \bar{n}_B(\eta + C_{t,B}P_t\chi_{had} - C_{h,B}P_h\chi_{tag})\right] \tag{7-9}$$

where,

$$\eta = C_{t,\,udsc}C_{h,\,nl}(1-P_t)P_h - C_{t,\,nl}C_{h,\,udsc}(1-P_h)P_t$$

$$\chi_{had} = C_{h,\,udsc} + (C_{h,\,nl} - C_{h,\,udsc})P_h$$

$$\chi_{tag} = C_{t,\,udsc} + (C_{t,\,nl} - C_{t,\,udsc})P_t$$

In the above solution, the B hadron decay multiplicity, $\bar{n}_B$, is obtained primarily from $\Upsilon(4s)$ data, the $C_{i,j}$'s are constants determined from the Monte Carlo, and F_b is the $Z^0 \to b\bar{b}$ branching fraction. The B hadron decay constants $C_{i,B}$ are determined by inclusive decay properties measured at the $\Upsilon(4s)$, while the light decay constants $C_{i,udsc}$ are constrained by the OPAL tuning of Lund 7.1 to hadronic data.[102] The non-leading constants $C_{i,nl}$, on the other hand, are not tightly constrained by existing data, and so must be constrained by more general arguments in order to preserve the model dependence of the measurement. The uncertainty introduced by these considerations will be addressed later.

A slight simplification of Equation (7-9) lends particular insight to the behavior of $\delta\bar{n}_b$. In the case where all of the constants $C_{i,j}$ are equal to the same number C (which is roughly true in actuality) the solution for $\delta\bar{n}_b$ becomes

$$\delta\bar{n}_b = \frac{(1-F_b)}{(P_t - P_h)}\,\frac{(\bar{m}_{tag} - \bar{m}_{had})}{C} \tag{7-10}$$

Here one can clearly see the advantage of measuring $\delta\bar{n}_b$ rather than the total multiplicity: systematic fluctuations which similarly affect the hadronic event sample and the tagged event sample multiplicities will tend to cancel. In particular, this avoids potentially large systematic errors due to tracking efficiency, photon conversions, and nuclear scattering. However, some remnant of systematic uncertainty will still result from these sources. This is because the actual formula for $\delta\bar{n}_b$ is Equation (7-9) and the reconstruction constants used in this formula are slightly different from each other, such that $\bar{m}_{tag}$ and $\bar{m}_{had}$ do not enter this equation as symmetrically as they do in Equation (7-10).

7.2 Measurement of Multiplicity Difference

This section describes the track cuts used to select a well-understood set of reconstructed tracks for the multiplicity determination, the tags used to select a $b\bar{b}$-enriched sample, the biases these tags induce on the multiplicity, the determination of the various constants, and a value for $\delta\bar{n}_b$.

7.2.1 Multiplicity Track Quality Cuts

Within the selected sample of events (the hadronic events and those tagged as $b\bar{b}$ events), a subset of the tracks is selected for inclusion in the measured multiplicities $\bar{m}_{had}$ and $\bar{m}_{tag}$. The track cuts employed are similar to the cuts used to select vertex-quality tracks for selecting $b\bar{b}$ events except for the requirements of DCVD and SSVD information. An important aspect of this analysis is that the vertex detector information is used only to tag $b\bar{b}$ events, while the multiplicity tracks are selected using the well-understood CDC.

The multiplicity track cuts are as follows.

1. The calculated angle of the track with respect to the beam axis must satisfy $|\cos\theta| < 0.8$ such that the tracks are well inside the active regions of the tracking detectors.
2. The projection of the track's momentum into the plane perpendicular to the beam axis, p_{xy}, must be greater than 0.150 GeV/c.
3. The distance of closest approach in the z-direction of the track to the nominal interaction point must satisfy $|z_m| < 15$ mm.
4. The number of hits associated with the track in the CDC tracking must be at least 25 of the 72 possible.
5. The impact parameter of the track, with respect to an interaction point which is fit on an event-by-event basis, must satisfy $|b| < 15$ mm.

Table 7–1 gives the fraction of tracks remaining after each cut is applied in order, as estimated by the Monte Carlo. Extensive studies have been done to ensure that the

track cut	% passed
1. $\|\cos\theta\| < 0.8$	94.3%
2. $p_{xy} > 0.15$ GeV	88.6%
3. $\|z_m\| < 15$ mm	80.8%
4. $N_{CDC} \geq 25$	80.6%
5. $\|b\| < 15$ mm	78.9%

Table 7–1 The fraction of the reconstructed tracks passing each of the multiplicity track quality cuts in events which pass all of the hadronic event selection cuts.

Monte Carlo is modelling these values sufficiently. This also allows systematic limits to be placed on the calculated value of $\delta\bar{n}_b$ which result from uncertainties associated with these cuts. (This will be addressed in detail in Section 7.3.11 on page 208).

In order to get some insight as to the relationship between the generated true multiplicity tracks (namely, the tracks to be counted in the multiplicity according to the definition on page 192) and those actually reconstructed in the detector, the generated and detected tracks were matched in the Monte Carlo. Of the reconstructed tracks, 90.5% are true multiplicity tracks, while the remaining 9.5% are due to conversions. (The effects of these conversion tracks on the determination of $\delta\bar{n}_b$ is addressed in Section 7.3.9 on page 207). On the other hand, of the generated true multiplicity tracks, 70.8% are properly reconstructed, 20.2% are outside the detector acceptance in $|\cos\theta|$ or p_{xy}, 6.5% are decays in flight from parents of lifetimes longer than the requisite 3×10^{-10} sec and the remainder are due to detector inefficiencies. Thus the corrections to the measured multiplicity are not large.

7.2.2 Impact Parameter Tags and Biases

As for the $Z^0 \to b\bar{b}$ branching fraction measurement, $Z^0 \to b\bar{b}$ candidates were selected by requiring that the event have at least a certain number of tracks, n_{min}, with a physically-signed impact parameter significance b/σ_b of at least some minimum value S_{min}.* Of the many variations of this tag using different

combinations of n_{min} and S_{min}, three tagging algorithms were investigated further, based on their statistical power for measuring the non-leading multiplicity. Each of these tags used S_{min} = 3.0.

7.2.2.1 Impact Parameter Tag Properties

The three significant track event tag ('EV3') was found, based on Monte Carlo studies, to have less statistical power than a two track event tag ('EV2'). One can remove much of the multiplicity bias introduced by the tag by restricting the tag to one hemisphere (as defined by the plane perpendicular to the thrust axis), and counting only the multiplicity in the hemisphere opposite to the tagged hemisphere. Thus, we included in the study a hemisphere-only tag ('HE2') requiring two or more significant tracks. The relevant properties of these three tags, as well as the event cut, are summarized in Table 7–2. Because there are very significant correlations

Tag Property	Event Selection	EV2 Tag	EV3 Tag	HE2 Tag
minimum impact parameter significance, S_{min}	—	3.0	3.0	3.0
minimum number of significant tracks, n_{min}	—	2/event	3/event	2/hemi.
$b\bar{b}$ efficiency (MC)	0.723±.007	0.723±.008	0.542±.009	0.423±.006
$b\bar{b}$ sample purity (MC)	0.227±.002	0.653±.008	0.841±.008	0.753±.007
Number of events tagged	196	48	30	49
$\delta\bar{n}_b$ statistical error	—	$^{+1.78}_{-1.86}$	$^{+1.97}_{-1.85}$	$^{+2.05}_{-2.00}$

Table 7–2 The properties of the event selection cuts and the three tags used for this multiplicity measurement. The tag efficiency for the tags is given with respect to the number of events which have already passed the hadronic event cuts and is that predicted by the full detector simulation Monte Carlo. The number of events tagged is what is observed in our data sample. The statistical errors are the result of a Monte Carlo study.

between the hadronic event multiplicity, the sample multiplicity and the sample purities, the statistical error was calculated using a Monte Carlo method. Specifically, it was calculated by using 72 Monte Carlo samples of identical size to the data sample and calculating $\delta\bar{n}_b$ in each. The spread in the resulting values of

* See Chapter 5 for more information on using the impact parameter significance tag to select $b\bar{b}$ events.

$\delta\bar{n}_b$ for all of these experiments indicates the statistical precision of the measurement. The 1σ range of $\delta\bar{n}_b$ was chosen as the central 68.3% of the values found in the 72 data samples. As will be discussed in a later section, the systematic error in the $Z^0 \to b\bar{b}$ multiplicity measurement is relatively small, and so we chose the EV2 tag for the measurement based solely on its statistical power. The other two tags will be used as checks on the multiplicity result.

7.2.2.2 Multiplicity Biases Introduced by the Impact Parameter Tags

Biases introduced by the tags, to the extent that they are modelled by the Monte Carlo, are taken into account naturally in the Monte Carlo-derived reconstruction constants $C_{i,j}$ described in Section 7.1. In order to have confidence that the Monte Carlo is correctly accounting for tag biases, it is helpful to understand the source of all biases which affect the result by more than a fraction of the statistical error.

A tag can alter the relationship between reconstructed and true multiplicity in two ways: either via correlations with the event multiplicity (e.g. events with high multiplicity B hadron decays are more likely to be tagged), or via correlations with the reconstruction efficiency. To study these effects, one can define two quantities: the *raw bias* and the *reconstructed bias*. The raw bias for a given set of tracks, j, (where $j \in udsc$, $b\bar{b}$ non-leading, or B decay tracks) is given by the following ratio of the Monte Carlo generated multiplicities $\bar{n}^{\,j}_{gen}$ for the sample of b-tagged events and for all of the hadronic events:

$$B^j_{raw} = \frac{\bar{n}^{\,j}_{gen}\ \text{(tagged events)}}{\bar{n}^{\,j}_{gen}\ \text{(all hadronic events)}}. \tag{7-11}$$

This raw bias is a measure of the correlation between the tagging efficiency and the multiplicity of the events tagged. The reconstructed bias is similarly given by ratio of multiplicities of tracks reconstructed by the tracking detectors after the Monte Carlo detector simulation, $\bar{m}^{\,i}_{recon}$:

$$B^j_{recon} = \frac{\bar{m}^{\,j}_{recon}\ \text{(tagged events)}}{\bar{m}^{\,j}_{recon}\ \text{(all hadronic events)}}. \tag{7-12}$$

where again the multiplicity sample i is that of subset f the tracks such as the $udsc$, $b\bar{b}$ non-leading, or B decay tracks. A value of 1.0 corresponds to no bias.

In the case of the hemisphere tag HE2, which is expected to be relatively free of bias, the raw bias is 0.989±.008 (1.016±.016) and the reconstructed bias 1.036±.009 (1.056±.015) for $Z^0 \to b\bar{b}$ ($Z^0 \to udsc$) events. The $1-2\%$ raw biases correspond to

less than 0.5 tracks, and are statistically consistent with 1.0. The reconstructed biases are significant, and are found to be due to the back-to-back correlation introduced by recoiling jets: the HE2 tag preferentially tags central events (namely those with $\cos\theta_{thrust} \sim 0$) due to the higher average reconstructed multiplicity, and since the untagged jets used to measure the multiplicity is recoiling against the tagged jet, it carries the preference towards events with a larger reconstruction fraction into the multiplicity measurement. If the sample is restricted to central events only ($|\cos\theta_{thrust}| < 0.6$), the reconstructed bias is reduced to 1.016±.011 (1.013±.019) for $Z^0 \rightarrow b\bar{b}$ ($Z^0 \rightarrow udsc$) decays. This is consistent with no bias. The removal of 3-jet events from the sample, which also might be expected to introduce significant hemisphere-to-hemisphere correlations, produces very little change in the HE2 tag bias. Nevertheless, it has been demonstrated that, for the HE2 tag, the 6% tag bias is understood in terms of effects well modelled by the Monte Carlo.

For the EV3 tag, where the biases are expected to be the largest,* the raw and reconstructed biases are given in Table 7–3 for $Z^0 \rightarrow b\bar{b}$ and $Z^0 \rightarrow udsc$ decays. The biases are given with the standard event cuts and after restricting the sample to central 2-jet events as above. The sources of this bias will be investigated separately for the $b\bar{b}$ and *udsc* events below.

Event Cuts	$Z^0 \rightarrow b\bar{b}$		$Z^0 \rightarrow udsc$	
	raw bias	recon. bias	raw bias	recon. bias
standard cuts	0.985±.008	1.005±008	1.060±.016	1.143±.017
2-jet events & $\|\cos\theta_{thrust}\| < 0.6$	1.012±.010	1.031±.010	1.090±.019	1.113±.020

Table 7–3 Raw and reconstructed biases for the EV3 tag.

Although the $Z^0 \rightarrow b\bar{b}$ reconstructed bias of 1.031 looks small, it is so only because of a cancellation between the biases for leading and non-leading tracks (1.061 *vs.* 0.995). However it is expected that significant biases may be present for an event tag. The possible sources of this bias include the B energy from fragmentation and the B decay multiplicity. The bias due to the B hadron energy can arise from the fact the impact parameter tag is more efficient for a higher B energy† and if the B has much of the energy, less is available for the non-leading

* By requiring that a given event have more significant tracks, the EV3 tag will more strongly bias the measured multiplicities than the less restrictive EV2 tag.

system to form additional particles. To examine this source of bias, events were selected in which both B hadrons have $x_E < 0.5$, $0.5 < x_E < 0.75$ or $x_E > 0.75$. The resulting biases in these event samples were found to still be statistically inconsistent with unity, indicating that the B hadron energy is not the dominant source of bias. In fact, the B hadron energy spectrum for the B hadrons in events tagged by the EV3 tag has virtually the same mean as that for all produced B hadrons, which indicates that this should not cause a bias. The B decay multiplicity is also a potential source of bias because a larger B decay multiplicity raises the tagging efficiency and also the multiplicity of the entire event. To investigate the bias due to the B decay multiplicity, the sample of events was binned by the number of tracks from the decays of both B hadrons in the event. Both the raw and reconstructed biases for the leading and non-leading tracks were found to be statistically equal to 1.0 within each of these bins, indicating that it is the B decay multiplicity which is the major source of bias for the event tag in $b\bar{b}$ events.

For $Z^0 \rightarrow udsc$ events the source of the remaining bias is also straight forward: it is simply due to the tendency of high multiplicity events to more often have the requisite number of significant tracks to be tagged. A simple calculation can demonstrate this for *uds* events. If one assumes that the significant tracks in such an event are uncorrelated, then binomial statistics can be used to estimate the *uds* bias. Two inputs are used from the full Monte Carlo: the probability of a track in a *uds* event having $b/\sigma_b > 3$ and a hadronic reconstructed multiplicity distribution. With this, the average reconstructed multiplicity of the tagged sample can be determined and the bias calculated. The results are that reconstructed biases for the EV3 (EV2) tag are 1.18±0.03 (1.13±0.01) using the full Monte Carlo and 1.24 (1.15) with this model. For $Z^0 \rightarrow c\bar{c}$ events, the effect of correlated heavy quark decay tracks is not large enough to significantly change the generally uncorrelated behavior seen with $Z^0 \rightarrow uds$ events.

Thus the source of the bias introduced by the different tags has been resolved for effects modelled by the Monte Carlo. For the hemisphere tag it results primarily from the back-to-back correlation between recoiling jets. For the whole event tags, the bias in $Z^0 \rightarrow b\bar{b}$ events results from the correlation with the high multiplicity and the large impact parameters of tracks from the decay of the heavy quark. For $Z^0 \rightarrow udsc$ events the bias simply arises from correlation between multiplicity and the likelihood of having two uncorrelated tracks with significantly mis-measured

† See Figure 5–5 on page 165 for information on the sensitivity of the impact parameter tag to certain B hadron properties.

impact parameters. In all cases, we are confident that these effects are either well modelled in the Monte Carlo, or will be properly addressed in the section on systematic errors (e.g. B decay kinematics, uncorrelated impact parameter smearing). Of course, there is always the possibility that there are biasing effects which the Monte Carlo knows nothing about. For these, we have only the consistency between the whole-event tags and the relatively unbiased hemisphere tag to indicate that the biases are properly modelled.

7.2.3 Calculation Parameters and Results

In order to derive $\delta\bar{n}_b$ from the measured multiplicity of the hadronic and the tagged events, the sample b-purities and reconstruction constants introduced in Section 7.1 must be determined. The purities P_h and P_t are determined by counting the number of b and $udsc$ events in the hadronic and tagged Monte Carlo samples. The reconstruction constants, $C_{i,j}$, are given by the Monte Carlo ratio of the reconstructed to generated multiplicity for all events in the categories specified by the indices i and j (*i.e.* tagged/un-tagged and $udsc$/B-decay/non-leading $b\bar{b}$). The values of these parameters for the event cuts and the three tags described in the previous section are shown in Table 7–4. The B decay multiplicity used to calculate

Tag Property	Hadronic Event Cuts	EV2 Tag	EV3 Tag	HE2 Tag
C_{udsc} (MC)	0.804	0.878	0.889	0.819
C_B (MC)	0.848	0.917	0.959	0.879
C_{nl} (MC)	0.749	0.745	0.731	0.776
tag b purity (MC)	0.227	0.653	0.841	0.753
mean multiplicity (data)	16.71	18.52	19.37	18.66
$\delta\bar{n}_b$ (data)	—	2.11	2.73	2.76

Table 7–4 The constants and multiplicities used to calculate the difference between the b event and total hadronic multiplicity. The reconstruction constants $C_{i,j}$ and the purity were determined by the Monte Carlo. The mean multiplicities are those observed in the data (see Figure 7–1) Note that the statistical error on the multiplicity difference is not calculated from the errors on the above quantities, but rather using the Monte Carlo method described on page 202.

$\delta\bar{n}_b$ was given by the average of the CLEO[130] and ARGUS[131] $B_{u,d}$ meson

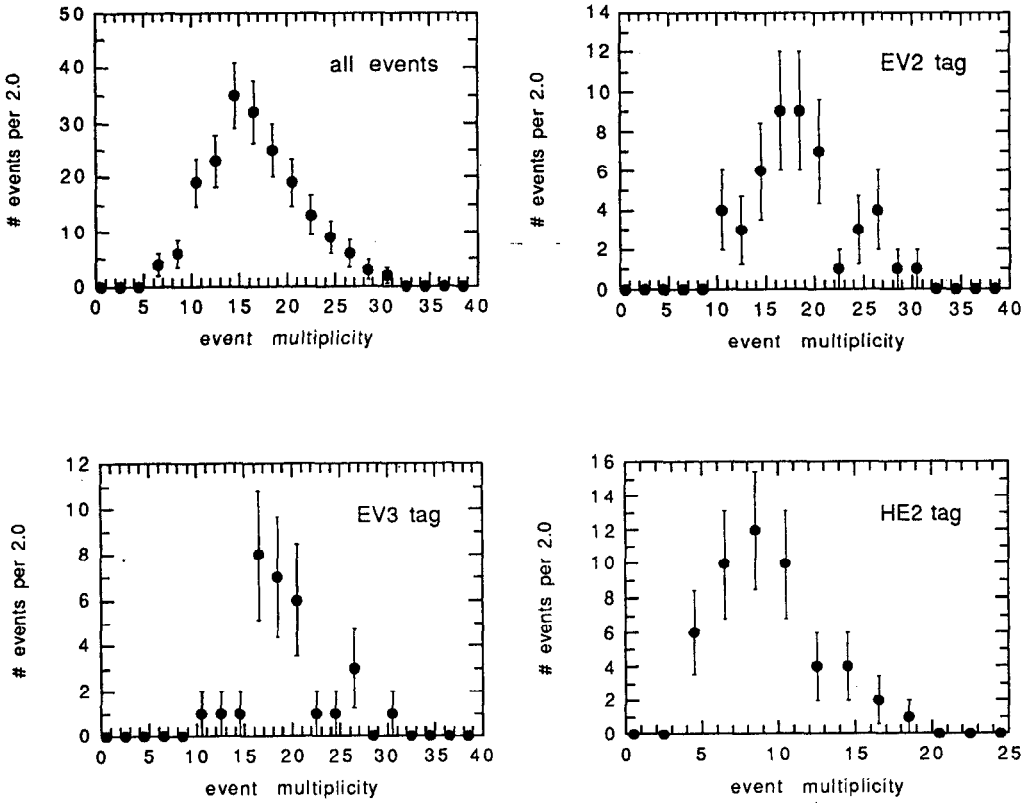

Figure 7–1 Multiplicity distributions for all events after the event selection cuts and for the events which passed each b-tag.

multiplicities measurements, 5.44, with a correction determined using the Lund Monte Carlo of 0.13 tracks per event to account for the decays of the other B hadrons ($B_{s,c}$ and B baryons). The resulting event multiplicity due to B-decay was thus $\bar{n}_B = 11.01$. This Monte Carlo correction for the heavier B species is described in more detail in Section 7.5 on page 214. For the $Z^0 \to b\bar{b}$ branching fraction, F_b, the standard model value of 0.217 was assumed.[13]

The measured multiplicity distributions for the hadronic sample and the three tagged samples are shown in Figure 7–1. Using the means of these multiplicity distributions, the values of $\delta\bar{n}_b$ for each of the three tags was calculated and is given in Table 7–4. To determine whether the three different tags yield consistent values for $\delta\bar{n}_b$, a technique similar to that used for determining the statistical errors was employed (see page 196). For 72 different Monte Carlo, $\delta\bar{n}_b$ was calculated using each of the three tags and the *difference* between $\delta\bar{n}_b$ calculated by each tag was recorded. The width of the resulting $\delta\bar{n}_b$ difference distribution yields

the level of difference one might expect to see in the data. The 1σ differences among these three tags were determined by the central 68.3% of these samples. Table 7–5

Tag	measured difference in $\delta\bar{n}_b$	expected 1σ difference in $\delta\bar{n}_b$
EV2 – EV3	–0.62	1.06
EV2 – HE2	–0.65	1.34
HE2 – EV3	0.03	1.59

Table 7–5 Comparison between multiplicity difference calculated using the three different tags.

shows the measured differences among the various combinations of the three tags with the expected 1σ difference. From this it is seen that all three values are consistent. Thus using the EV2 tag as the standard, the nominal result is,

$$\delta\bar{n}_b = 2.11^{+1.78}_{-1.86} \tag{7-13}$$

where this error is statistical only.

As another check, the reconstruction constants for the hadronic event cut sample, $C_{h,j}$, can be combined into a single constant and multiplied by the measured mean multiplicity in the hadronic sample of 16.71±0.35, to yield a corrected multiplicity for the 1991 data set of 20.89±0.44 (statistical error only). This value is close to the world average total multiplicity of 20.94±0.20 and provides an independent check that our method of extracting the 'true' multiplicity from the measured multiplicity is sensible. Furthermore, if the reconstruction constants are entirely ignored by using Equations (7-2) and (7-3), the result for $\delta\bar{n}_b$ is 4.13. This would cause a difference of less than 20% in the resulting value of the non-leading multiplicity in $b\bar{b}$ events, compared to the value calculated using the fully corrected equations. This difference is the full effect of the biases and variations among the individual reconstruction constants.

7.3 Systematic Errors in the Multiplicity Difference

A broad range of effects which can systematically affect $\delta\bar{n}_b$, either through the tagging purities or the reconstruction constants, were investigated. The sources of error due to uncertainties in various physics parameters include the ability to

properly model events in the three classes (*udsc*, *B*-decay and non-leading tracks in $b\bar{b}$ events) and heavy quark production and decay properties (branching ratios, fragmentation, lifetimes). Other errors result from uncertainties in the detectors. These include track finding efficiency, tracks from photon conversions, multiple Coulomb and nuclear scattering, track selection cuts, and impact parameter resolution. The final source of systematic error is that due to the finite number of tracks used in the Monte Carlo data sample.

The principle sources of error for this measurement are:

- the uncertainty in modelling the momentum and polar angle distributions of the non-leading tracks in $b\bar{b}$ events;
- the uncertainty in the impact parameter resolution function;
- the statistics in the number of Monte Carlo events generated.

All of the significant sources of systematic error are discussed below and values are given for the EV2 tag. A summary of the results can be found in Table 7–8 on page 213. The total systematic error in $\delta\bar{n}_b$ is significantly smaller than the statistical error.

7.3.1 Modelling of $Z^0 \rightarrow$ *udsc* Decays

Since the acceptance of the Mark II detector is not perfect, there will be a dependence of the reconstruction constants $C_{i,j}$ on the modelling of hadronic events due to acceptance limits in $\cos\theta$ and p_{xy}. In the case of *udsc* events, the distributions of these variable are well constrained by the existing measurements of the exclusive properties of hadronic decays.

All reconstruction constants were initially derived using the Lund 6.3 Parton Shower tuned primarily to Mark II data from PEP, as discussed in Chapter 3. For *udsc* events, the reconstruction constants were then corrected to those corresponding to a more recent tuning of Lund done at the Z^0 by OPAL.[102] This was accomplished by comparing the two models in $\cos\theta$ and p_{xy} at the generator level, after applying a cut equivalent to the event cut applied after full detector simulation. For all three tags, the correction to the light quark reconstruction constants were less than 0.1%.

The uncertainty in $\delta\bar{n}_b$ introduced by the uncertainty in the light quark reconstruction constants was studied by varying the Lund Parton Shower parameters within the range constrained by the OPAL tuning, and calculating the resulting change in the reconstruction constants. The corresponding uncertainty in $\delta\bar{n}_b$ was found to be less than ± 0.05 tracks. There is also uncertainty due to the

model-dependent extrapolation below $|\cos\theta| = 0.8$ and $p_{xy} = 0.15$ GeV/c, which is outside the acceptance of all experiments. To be conservative, an ALEPH estimate is used of the uncertainty associated with this extrapolation. Using a somewhat larger p_{xy} cut of 0.2 GeV/c, they estimated this to be ±0.1 tracks.[114] Combining these two effects, the total uncertainty in $\delta\bar{n}_b$ due to the uncertainty in the modelling of udsc events is taken as ±0.10.

7.3.2 Modelling of Non-leading Particle Production in *b* Events

In the case of non-leading tracks from $Z^0 \to b\bar{b}$ decays, there is no data available to constrain the $\cos\theta$ and p_{xy} distributions, and in particular the fraction of these tracks which fall outside of the detector acceptance of $|\cos\theta| < 0.8$ and $p_{xy} > 0.15$ GeV/c . Consequently, an approach based on more general principles is warranted.

Within the Lund Parton Shower Model, the various parameters control the stiffness of the momentum spectrum and the spread of the event around the jet axis (*e.g.* the vector to pseudovector ratio, strangeness and baryon production, fragmentation and shower cut-off energies) have been varied over wide ranges. In addition, the Matrix Element generator has been substituted for the Parton Shower routine and Feynman-Field fragmentation has been substituted for the Lund String fragmentation for light quarks. None of these effects changed $\delta\bar{n}_b$ by more than 0.25 tracks.

In addition to the above, the momentum spectrum of the non-leading tracks was rescaled so that the fraction of the non-leading energy in the form of charged tracks varied between 2/3, corresponding to pure isospin 1 (pion-like) production, and 1/2, corresponding to pure isospin 1/2 (kaon-like) production. This is an extremely conservative constraint: if instead this range is changed by varying the level of mass suppression, or the relative population of SU(3) multiplets, the variation in the charged energy fraction is less than half of this size. In any case, varying the non-leading charged energy fraction from 0.50 to 0.67 (our default Lund Monte Carlo gives 0.59), yields, an error in $\delta\bar{n}_b$ of ±0.4 tracks. In the interest of preserving the model independence of this measurement, this conservative estimate is taken as the systematic error.

7.3.3 *B* Decay and Modelling of Leading Particle Properties

The measurement of $\delta\bar{n}_b$ is sensitive to the modelling of the B hadron decay properties, such as the multiplicity and momentum spectrum, through the leading reconstruction constants $C_{i,B}$ and the tag purity. These properties are constrained

primarily by CLEO and ARGUS measurements at the $\Upsilon(4s)$.[130][131][133] A reweighting technique was used to conform to the CLEO and ARGUS data, and to study the uncertainty in $\delta\bar{n}_b$ introduced by the uncertainty in these constraints, as was used in the $Z^0 \to b\bar{b}$ fraction measurement in Section 6.3.6 on page 184. The largest effect, the uncertainty in the B decay multiplicity, was found to introduce an uncertainty of ±0.05 tracks in $\delta\bar{n}_b$. The variation in $\delta\bar{n}_b$ associated with the softening of the Lund generated momentum spectrum to agree with the CLEO data was negligible.

7.3.4 3-Jet Rate

The dependence of the 3-jet rate was explored through the use of a reweighting scheme which preserved $\langle x_E \rangle_b$ while varying the 3-jet rate (at $y_{min} = 0.08$) over a very conservatively large range between 0.12 and 0.22.[136] The resulting change in $\delta\bar{n}_b$ was ±0.04 tracks.

7.3.5 Non-hadronic Contamination

For the initial Mark II hadronic decay measurements, the non-hadronic background was estimated to be 0.42 events in the sample of 398 hadronic events.[62] For the 1991 data sample of 196 hadronic events, with slightly more stringent hadronic event selection cuts, this corresponds to a contamination of less than 0.2 events. In the worst possible case, if this 0.2 events has 7 tracks (the minimum allowed by the event selection cuts) and is tagged (unlikely), it causes an uncertainty of 0.05 tracks in $\delta\bar{n}_b$.

7.3.6 Bottom and Charm Hadron Production and Lifetimes

The result for $\delta\bar{n}_b$ will depend on the branching ratio of the Z^0 to bottom and charm quarks, the energy carried off by the heavy hadron during fragmentation and lifetime of the heavy hadrons, primarily through their effects on the purity of the tagged event samples. For more information on the limits chosen here, see Section 6.3 on page 180.

7.3.6.1 Z^0 Branching Fraction to Bottom Quarks

All four LEP experiments have measured $\mathrm{Br}(Z^0 \to b\bar{b})$ and as discussed in Section 1.5 on page 22, the average value is 0.212±0.011. Varying the fraction of $b\bar{b}$ events by ±0.011 in the Monte Carlo will change $\delta\bar{n}_b$ by ±0.05 tracks.

7.3.6.2 Z^0 Branching Fraction to Charm Quarks

Similarly, $\mathrm{Br}(Z^0 \to c\bar{c})$ has been well measured using both a high p_T lepton tag at ALEPH[22] and D^* tags at DELPHI[129] and OPAL.[95] The average of these

measurements is 0.171±0.029. Varying the fraction of charm events in the Monte Carlo similarly yields a systematic error in $\delta\bar{n}_b$ of ±0.10 tracks.

7.3.6.3 Bottom Fragmentation

The mean energy carried away by the bottom hadron, $\langle x_E \rangle_b = E_B/E_{beam}$, will affect $\delta\bar{n}_b$ both through the reconstruction constants and the tag purity. The energy carried away by the B hadron determines how much energy is left to produce the non-leading particles, and in this way the value of $\langle x_E \rangle_b$ will affect the non-leading reconstruction constants. The track impact parameters also have a weak dependence on $\langle x_E \rangle_b$ (see Figure 4–2 on page 110), and thus the tag efficiency and purity will also depend on the stiffness of the fragmenting process. The average of the measurements by ALEPH,[22] L3,[23] and OPAL[24] is $\langle x_E \rangle_b = 0.697 \pm 0.017$ corresponds to an error on $\delta\bar{n}_b$ of ±0.03 tracks. Note that care must be taken to hold the non-leading multiplicity constant while $\langle x_E \rangle_b$ is varied. This was achieved using a reweighting scheme which depended on both the $\langle x_E \rangle_b$ of the two B hadrons in an events and the non-leading multiplicity. As discussed in Section 6.3.3 on page 182, no attempt is made to account for uncertainty in the shape of the fragmentation function.

7.3.6.4 Charm Fragmentation

The average energy carried off by charmed hadrons, $\langle x_E \rangle_c$, will affect the reconstruction constants and tag purities as in the case of the bottom hadrons. The average of 0.515±0.011 is the result of measurements by ALEPH[22] and OPAL.[95] Using this uncertainty to provide a systematic limit on $\delta\bar{n}_b$ yields an error of ±0.03 tracks.

7.3.6.5 Bottom Hadron Lifetime

The average lifetime of the B hadrons is well measured[102][25] and as discussed in Section 6.3.1 on page 180, has an average value of 1.31±0.07 picoseconds. This uncertainty corresponds to an uncertainty in $\delta\bar{n}_b$ of ±0.03 tracks.

7.3.6.6 Charm Hadron Lifetime

The lifetimes of each of the charm hadrons have been independently measured. Varying the D^0, $D^{\pm}$, D_s and Λ_c within the Particle Data Group limits[102] produces an uncertainty in $\delta\bar{n}_b$ of ±0.02 tracks. Additionally, if the ratio of D^0 to $D^{\pm}$ production is varied from 0–100% vector (D^*) production leads to uncertainty of ±0.05 tracks in $\delta\bar{n}_b$.

7.3.7 Intrinsic Impact Parameter Resolution

As discussed in Section 6.3.9 on page 186, additional impact parameter smearing is required in the Monte Carlo in order to reproduce the impact parameter distributions observed in the data. Making the same conservative choice as before by using the 2σ allowed region of different amounts of smearing, and determining the reconstruction constants for each of these values yields a systematic error in $\delta\bar{n}_b$ of ± 0.15 tracks. A limited amount of very broad impact parameter smearing (the 'far tail') is also allowed (see Table 4–3 on page 137), and using the 2σ allowed far tail smearing leads to an additional error on $\delta\bar{n}_b$ of ± 0.02 tracks. Thus the total systematic error on $\delta\bar{n}_b$ due to the uncertainty in the intrinsic impact parameter resolution is ± 0.15 tracks.

7.3.8 Multiple Coulomb and Nuclear Scattering

Using methods as described in Section 6.3.10 on page 186, systematic limits can be placed on $\delta\bar{n}_b$ which result from multiple Coulomb scattering and both elastic and inelastic nuclear scattering. The amount of scattering material which most affects the impact parameter resolution, namely that in the beam pipe and SSVD, can be constrained to $\pm 3\%$ with our statistics. Varying the amount of scattering material in the inner scattering layers by this amount results in a change in $\delta\bar{n}_b$ of ± 0.04 tracks. Although the material in the DCVD and CDC is more difficult to study using tracking information, it is less important for the impact parameter resolution. This material is, however, quite relevant for photon conversions as will be discussed in the next section. Using the inelastic nuclear scattering generator, it was found a conservative systematic limit of ± 0.10 tracks can be placed on $\delta\bar{n}_b$.

7.3.9 Photon Conversions

The Monte Carlo predicts that 9.3% of the reconstructed tracks which pass the multiplicity track cuts arise from photon conversions. Hence it is important that these be well modelled so their effect is properly accounted for in the reconstruction constants, $C_{i,j}$. Two approaches were taken to verify our modelling of these conversion tracks. The first check is a rough estimate based on the Monte Carlo generated photon spectrum. It has been estimated that the conversion probability is $P_c = 7/9\,(L/L_R)$, where L/L_R is the number of radiation lengths.[137] Making use of the generated photon spectrum and the nominal material thicknesses in the Monte Carlo, this estimates that conversions should be between 9 and 11% of all of the reconstructed charged tracks, thus confirming the more rigorous result from the detector simulation.

The second check investigated how well the conversion tracks are modelled in comparison to our data. This uses the fact that according to the detector simulation, greater than 60% of the conversion tracks originate in the DCVD outer wall and the CDC inner wall. Thus the addition of a track cut which requires track information to be found in the DCVD will substantially reduce the number of conversions. If at least 15 out of 32 possible position measurements in the DCVD are required the detector simulation predicts that the fraction of tracks from conversions should be reduced from 9.3% to 3.7%. When $\delta\bar{n}_b$ is determined using the additional track cut and the EV2 tag, the result differs by 0.27 tracks from the nominal result. The significance of the difference is determined as above using the 72 Monte Carlo data samples of 220 events, and it is found that the expected 1σ difference between the determination with and without the requirement of DCVD information on the tracks is 0.83 tracks, thus indicating that the observed difference of 0.27 is well within the expected range.

Given the consistency of these two checks and the accuracy of the *a priori* knowledge of the amount of material present in the detectors (particularly the DCVD/CDC interface region which is not well constrained by the impact parameter resolution studies of the previous section) a very conservative limit of ±20% is placed on the number of conversion tracks. This corresponds to a systematic error in $\delta\bar{n}_b$ of ±0.05 tracks.

7.3.10 Track Finding Efficiency

The track finding efficiency has been studied as described in Section 4.6 on page 144, and is understood to within ±1% for the multiplicity track cuts (which do not use the vertex detector information). This corresponds to a systematic error in $\delta\bar{n}_b$ of ±0.04 tracks. It is interesting to note that this uncertainty would be much larger (>0.2 tracks) if instead of $\delta\bar{n}_b$, the total multiplicity had been measured.

7.3.11 Track Cuts

Differences between the effects of the multiplicity track cuts on the data and the Monte Carlo are also a possible source of systematic error. (See Section 7.2.1 on page 194 for a description of these cuts.) Exclusive distributions* of the quantities used in the multiplicity track cuts are shown in Figure 7–2 for all of the events which pass the hadronic selection cuts, and in Figure 7–3 for the events which were tagged by the EV2 tag. As an initial check, each of the cuts was separately varied

* In this usage, 'exclusive distribution' means that when looking at the distribution of one variable used in the track cuts, the other cuts have already been applied.

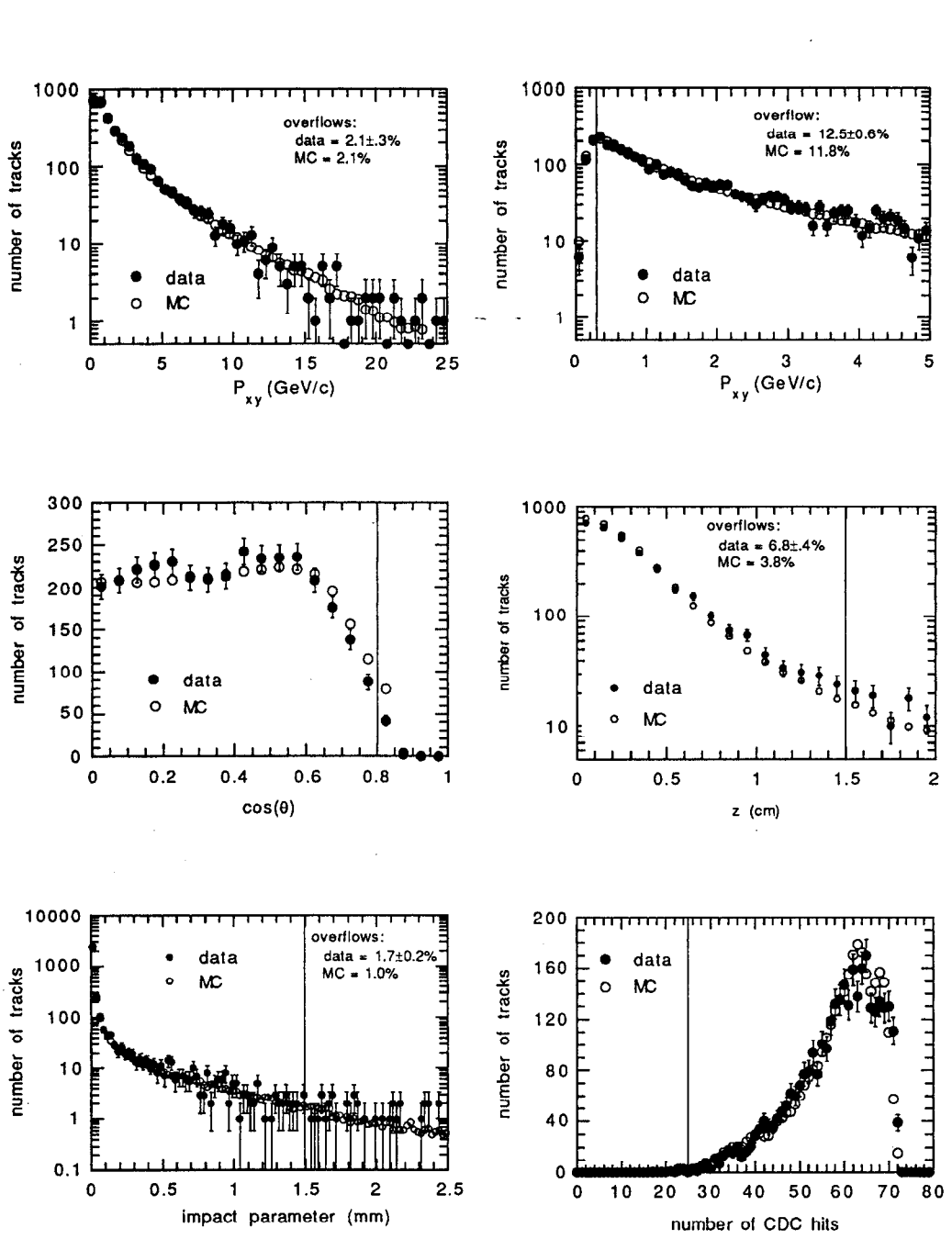

Figure 7–2 Exclusive track distributions of the variables used for the multiplicity track cuts for all events. The apparent discrepancy in the cos θ distribution actually is just a result of a slightly lower fraction of events in the data at values of large |cos θ| probably resulting from a statistical fluctuation. Specifically, in the data we see 81±11% as many tracks in the region $0.6 < |\cos\theta| < 0.8$ as are predicted by the Monte Carlo.

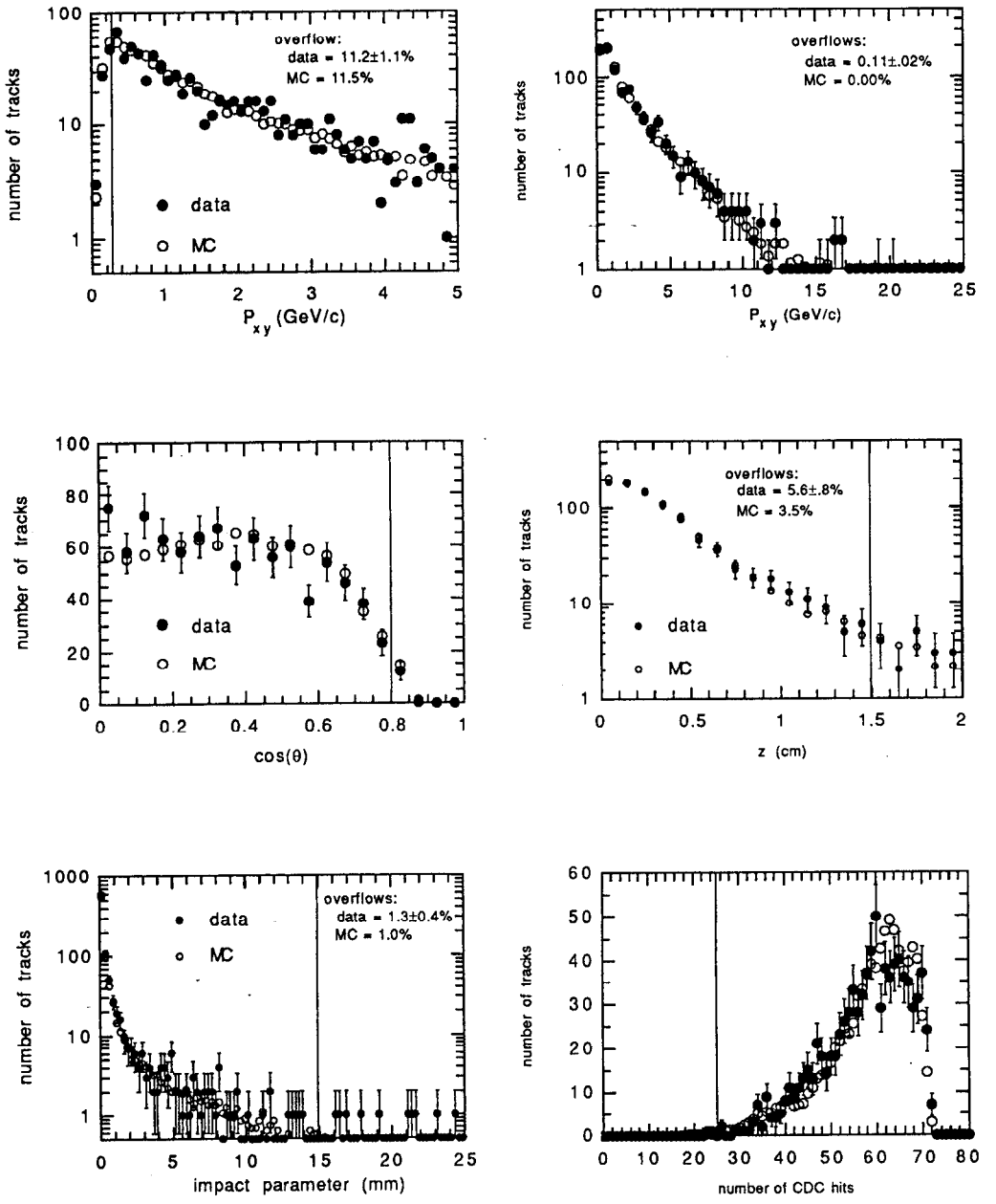

Figure 7–3 Exclusive track distributions of the variables used for the multiplicity track cuts for events which were selected by the EV2 tag.

Original cut	Modified cut	measured difference in $\delta\bar{n}_b$	expected 1σ difference in $\delta\bar{n}_b$
$\lvert\cos\theta\rvert < 0.8$	< 0.6	0.756	1.502
	< 0.7	0.604	0.587
$p_{xy} < 0.15$ GeV/c	< 0.25 GeV/c	–0.401	0.306
	< 0.50 GeV/c	–0.453	0.814
$N_{CDC} \geq 25$	≥ 15	0.004	0.058
	≥ 35	0.084	0.222
$\lvert z_m \rvert < 15$ mm	< 10 mm	0.060	0.263
	< 20 mm	0.162	0.212
$\lvert b \rvert < 15$ mm	< 10 mm	0.060	0.156
	< 20 mm	–0.032	0.125

Table 7–6 The difference between multiplicity difference $\delta\bar{n}_b$ calculated with the original multiplicity track cuts and the case when one of the multiplicity track cuts at a time is changed. In only 2 of the 10 cases does the measured difference exceed one standard deviation.

and a value for $\delta\bar{n}_b$ calculated with this new cut. To gauge the significance of the difference between the result with the original and the modified cuts, the same method used above was employed. In this method the values of $\delta\bar{n}_b$ are calculated for 72 Monte Carlo event samples of the same size as the data sample. The standard deviation of the differences in $\delta\bar{n}_b$ calculated with the original and modified cuts for the 72 samples thus provides an estimate of the expected difference in $\delta\bar{n}_b$. Table 7–6 shows the results of this test. Of the 10 trails in which a particular cut value was varied, the difference of $\delta\bar{n}_b$ was greater than one standard deviation in only 2 of them.

To obtain some quantitative estimate of the systematic error, the differences between the fraction of tracks outside the cuts in the data and Monte Carlo was interpreted as an uncertainty in the reconstruction efficiency. This approach is very conservative, as the cuts are designed to remove regions where the detector modelling is suspected to be poor. The data/Monte Carlo differences are given for

multiplicity track cut	fraction fail: data	fraction fail: MC	fraction fail: data – MC	effect on $\delta\bar{n}_b$
$\|\cos\theta\| < 0.8$	1.33±.20%	2.48%	-1.15%	±0.03
$p_{xy} < 0.15$ GeV/c	1.33±.20%	1.71%	-0.38%	±0.01
$N_{CDC} \geq 25$	0.21±.08%	0.22%	-0.01%	±0.00
$\|z_m\| < 15$mm	8.97±.48%	5.46%	3.51%	±0.06
$\|b\| < 15$ mm	2.79±.28%	2.04%	0.75%	±0.01
Total Systematic Error on $\delta\bar{n}_b$ due to multiplicity track cuts:				±0.07

Table 7–7 A data/Monte Carlo (MC) comparison of the fraction of tracks failing each track cut. The differences are used to set a conservative limit on the multiplicity difference.

each cut in Table 7–7 along with the effective uncertainty this introduces in $\delta\bar{n}_b$, as measured by the EV2 tag. The sum of the effects in quadrature yields ±0.07 tracks which will be taken as the systematic uncertainty due to the uncertainty in the effect of the track cuts.

7.3.12 Monte Carlo Statistics

Since the reconstruction constants and purities were determined using the Monte Carlo, there will be an uncertainty due to the finite statistics of the Monte Carlo sample of 20,000 hadronic events with full detector simulation. The effect of this level of statistics is a systematic error of ±0.30 tracks in $\delta\bar{n}_b$.

7.3.13 Full Result for the Multiplicity Difference

Table 7–8 has a summary of the contributions to the systematic error $\delta\bar{n}_b$ for the EV2 tag. The sum of these systematic errors in quadrature is ±0.57 tracks and thus the full result for the difference between the multiplicity of $b\bar{b}$ events and all flavors of hadronic events is

$$\delta\bar{n}_b = 2.11 \pm 1.82\,(\text{stat}) \pm 0.57\,(\text{syst})\,.$$

Source of Systematic Error	Range	Systematic Error on $\delta\bar{n}_b$
MC Model: *udsc* tracks	see text	±0.10
MC Model: non-leading tracks from $b\bar{b}$ events	see text	±0.40
MC Model: B decay tracks	see text	±0.05
3-jet fraction	0.12 – 0.22 (at y_{min} = 0.08)	±0.04
non-hadronic events	0–0.2 in 196 events	±0.05
b fragmentation	0.680 – 0.714	±0.04
c fragmentation	0.504 – 0.526	±0.03
average bottom hadron lifetime	1.24 – 1.38 psec	±0.03
average charm hadron lifetime	PDG limits	±0.05
$\mathrm{Br}(Z^0 \to b\bar{b})$	0.201 – 0.223	±0.05
$\mathrm{Br}(Z^0 \to c\bar{c})$	0.142 – 0.200	±0.10
conversion tracks	±20%	±0.05
multiple scattering	±3%	±0.03
nuclear scattering	see text	±0.10
impact parameter resolution	see text	±0.15
track finding efficiency	±1%	±0.04
multiplicity track cuts	see text	±0.07
Monte Carlo statistics	20000 MC events	±0.30
Total Systematic Error on $\delta\bar{n}_b$		±0.57

Table 7–8 A summary of the systematic errors on the difference of b and *udscb* multiplicity.

7.4 Center-of-Mass Energy

The average center-of-mass energy for the 1990 running has been measured with the distribution of energy spectrometer readings from runs with Small Angle Monitor Bhabha events to be

$$\langle E_{cm} \rangle = 90.93 \pm 0.01 \pm 0.04 \text{ GeV}$$

with a roughly Gaussian distribution of width 0.2 GeV.[50] In certain cases, in order to make a proper comparison with lower energy data, this value must be corrected for the effect of initial state radiation, which is small near the Z^0 resonance. For example, the corrections, as given by the standard Lund initial state radiation routine, at the Z^0 mass and 400 MeV below and above it are –0.20, –0.21 and –0.41 GeV, respectively. The correction for the data sample, most of which lies between 90.7 and 91.2 GeV, is approximately –0.20 GeV. Thus the average center-of-mass energy for the 1990 run, corrected for initial state radiation, is

$$\langle E_{cm}^{\text{isr corr.}} \rangle = 90.7 \text{ GeV}.$$

7.5 *b* Event Total and Non-leading Multiplicities

To extract the value of the average non-leading multiplicity, we recall that $\delta\bar{n}_b = \bar{n}_b - \bar{n}_{had}$. The $Z^0 \to b\bar{b}$ event multiplicity, $\bar{n}_b$, can be written as the sum of the B hadron decay multiplicity and the non-leading multiplicity, $\bar{n}_B + \bar{n}_{nl}$. Substituting this into the above equation for $\delta\bar{n}_b$ and solving for the non-leading multiplicity yields,

$$\bar{n}_{nl} = \delta\bar{n}_b + \bar{n}_{had} - \bar{n}_B. \tag{7-14}$$

As shown in Table 7–9, the total hadronic multiplicity, $\bar{n}_{had}$ has been well measured at the Z^0 resonance by Mark II and all four LEP experiments. The average $\bar{n}_{had} = 20.94 \pm 0.20$ tracks per event. Adding this value to $\delta\bar{n}_b$ gives a $b\bar{b}$ event multiplicity of

$$\bar{n}_b = 23.05 \pm 1.82 \text{ (stat)} \pm 0.60 \text{ (syst)}.$$

To determine the non-leading multiplicity in $b\bar{b}$ events, the B decay multiplicity is required. The multiplicity of $B_{u,d}$ meson decays has been well measured at the $\Upsilon(4s)$. CLEO[130] and ARGUS[131] have measured the multiplicity at the $\Upsilon(4s)$ to be 10.81±0.05±0.23 and 10.99±0.06±0.29 respectively. The average of these values

experiment	total charged multiplicity
ALEPH[114]	20.85±0.02±0.24
OPAL[115]	21.40±0.02±0.43
DELPHI[116]	20.71±0.04±0.84
L3[117]	20.70±0.02±0.70
Mark II[113]	20.10±1.00±0.90
Average	20.94±0.20

Table 7-9 The previous measurements of the total charged multiplicity at the Z^0 and weighted average. The average accounts for the correlated systematic errors among the experiments.

taking into account an estimate of the common systematics is 10.88±0.20. At energies higher than the $\Upsilon(4s)$ however, there are contributions to the B hadron decay multiplicity from other B mesons and B baryons. The Lund Monte Carlo calculates that the B hadron multiplicity for all B species is 0.13 tracks per event higher than for $B_{u,d}$ only. A summary of the production fractions and multiplicities as predicted by Lund are given in Table 7–10. Adding this to the CLEO and ARGUS

B hadron species	production fraction	average multiplicity per event
$B_{u,d}$	0.79	10.88
B_s	0.12	11.34
B baryon	0.09	11.74
average B hadron multiplicity per event		11.01

Table 7-10 Production fractions and decay multiplicities used for the different B hadron species. The production fractions are those predicted by the Lund Monte Carlo. The decay multiplicities for $B_{u,d}$ and B baryons are also predicted by the Lund Monte Carlo and scaled to the average of the CLEO and ARGUS values for the $B_{u,d}$ decay multiplicity.

average multiplicity gives a value for the combination of all B hadron species of

11.01 tracks per event. Of course this number is somewhat sensitive to the specific assumptions in the Monte Carlo regarding the decay multiplicities of the B_s and B baryons and production fractions of the different B species. Although no experimental information on B_s and B baryon multiplicities exists, and theoretical information is of little help, one expects that because of the high Q^2 of the decays, the differences between the decays of the $B_{u,d}$ are reasonably well handled by standard approaches, such as that implemented by the Lund Monte Carlo, in which the difference is simply provided by the change in the phase space.

There is however some information available about the production fractions of the different B hadrons. Although the information on the B baryon production fraction is limited,* one can constrain the B_s production fraction, $P(b \to B_s)$, using the present measurements of $B\bar{B}$ mixing. This is done using a Standard Model places a constraint on the relative mixing strengths of B_d and B_s, which results from the unitarity of the Kobayashi-Maskawa (KM) matrix (see Appendix A). The $b \to B_s$ fraction is found in this manner to be 0.18±0.10, assuming a B baryon production fraction of 0.1±0.1. This is consistent with the Lund prediction of 0.12.

Using the $b \to B_s$ fraction found above and 0.1±0.1 as the B baryon production fraction, this adds an uncertainty of ±0.04 tracks to the 0.13 track correction to the B decay multiplicity which accounted for the non-$B_{u,d}$ hadrons. Thus the B decay multiplicity at the Z^0 is taken as

$$\bar{n}_B = 11.01 \pm 0.20.$$

Thus with the value for $\delta\bar{n}_b$ as found in Section 7.3.13, the world average value for the total hadronic charged multiplicity at the Z^0 resonance from Table 7–9 and this value of the B decay multiplicity modified to include all of the B hadron species, the non-leading multiplicity is calculated at the initial-state radiation corrected center-of-mass energy of E_{cm} = 90.7 GeV to be

$$\bar{n}_{nl} = 12.04 \pm 1.82\ (\text{stat}) \pm 0.63(\text{syst}).$$

* ALEPH has done a presently-unpublished analysis of Λ_b production. They use a fairly standard lepton tag to measure the quantity $P(b \to \Lambda_b) \cdot Br(\Lambda_b \to l + \Lambda + X)$. The size of the errors and the fact that this will not constrain the production of the other weakly-decaying B baryons (the Σ_b^+ and Σ_b^-) limits the usefulness of this measurement for our purpose. For more information on this measurement, see Reference [127].

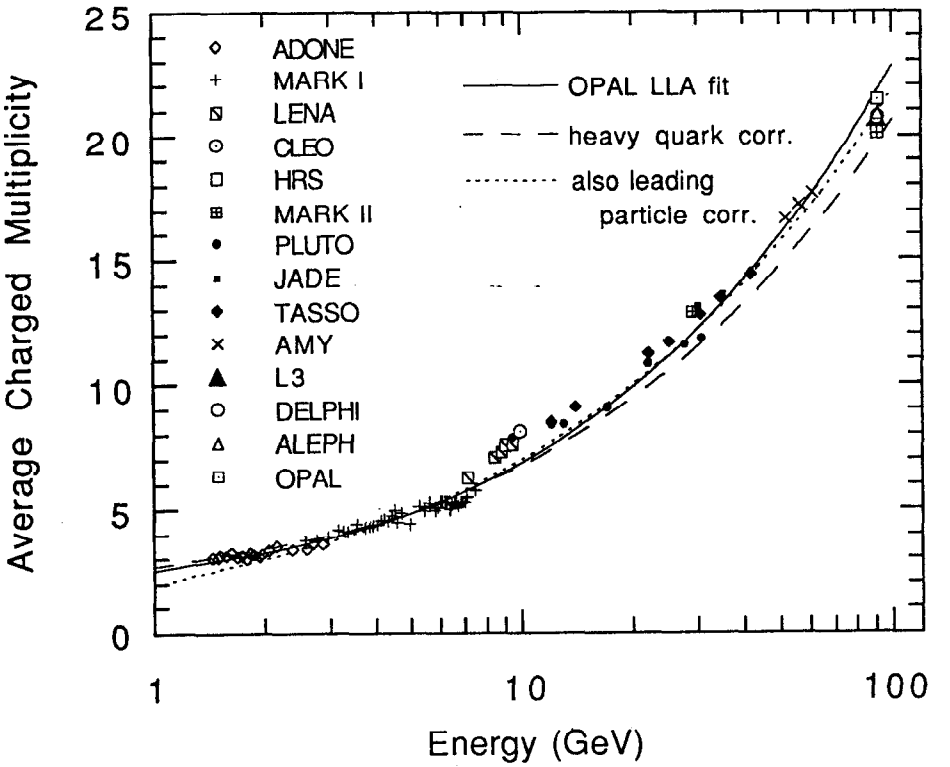

Figure 7–4 World sample of e^+e^- annihilation charged multiplicity data versus E_{cm}. Each of the fits is based on the leading log approximation-inspired form. The OPAL fit corresponds to the constants given in Reference [115]. The heavy quark corrected fit removes the effects of c and b production, as discussed in Section 7.6.1. The third fit has removed the leading particle effects, in addition to the heavy quark correction (see Section 7.6.3). The data comes from References [97], [114], [115], [116], [117] and [138].

7.6 Comparison with Data at Lower C.M. Energy

Figure 7–4 shows the world sample of non-resonant mean charged multiplicity data versus the center-of-mass energy, E_{cm}, for e^+e^- annihilation. The solid line in the figure is a fit to the multiplicity data using the leading-logarithm approximation (LLA) inspired form,[139]

$$\bar{n}_{had} = a + b \cdot \exp\{c\sqrt{\ln E_{cm}}\}, \tag{7-15}$$

where a, b, and c are the constants determined by the fit and E_{cm} is in GeV. For this fit, done by OPAL, the constants have the values $a = 2.418$, $b = 0.113$ and $c = 2.421$.[115] While the LLA inspired form provides a general description of the

data over a wide range of energies, there are some regions where the agreement is not very good. In particular, the fit is significantly lower than the data in the region around the bottom threshold, where one would expect that the LLA inspired shape would not hold. There is probably a similar problem at the charm threshold, obscured by the large systematic uncertainty of the Mark I data. Clearly, one should use caution in making such global fits to the multiplicity. To make the comparison between the non-leading multiplicity and this data more meaningful, several corrections were studied.

7.6.1 Heavy Quark Correction

In the total multiplicity measurements of Figure 7–4, there is a significant contribution from heavy quark ($c\bar{c}$ and $b\bar{b}$) production, which is almost entirely absent in the non-leading production process, and thus must be removed from the total multiplicity measurements. At 29 GeV, we find that the heavy quark event multiplicities are[37][39][40]

$$\bar{n}_{c\bar{c}} = 13.4\pm0.7 \text{ and } \bar{n}_{b\bar{b}} = 15.7\pm0.6,$$

and from all PEP and PETRA measurements near 29 GeV[140] the multiplicity for all flavors of hadronic events is

$$\bar{n}_{udscb} = 12.41\pm0.21.$$

Combining these yields a correction to the total multiplicity to account for the presence of heavy quarks of

$$\bar{n}_{udscb} - \bar{n}_{uds} = 1.20\pm0.50.$$

To extend this to other center-of-mass energies, the Lund Monte Carlo was employed with the parameter settings determined by Chrin,[42] (taking care to evolve ε_c and ε_b in the manner outlined in that article) tuned to the above multiplicity difference at 29 GeV.

With the multiplicity data corrected in this fashion, it was re-fit to the LLA-inspired form with the result

$$\bar{n}_{had} = 2.554 + 0.1252 \cdot \exp\{2.317\sqrt{\ln E_{cm}}\}.$$

Figure 7–5 shows the corrected data and the fit. With the heavy quark contributions removed, the LLA form provides a much better description of the data. The worst agreement is in the region between 3 and 7 GeV, which is nevertheless within the common systematic error of 0.9 tracks of the Mark I data in that region. This fit is

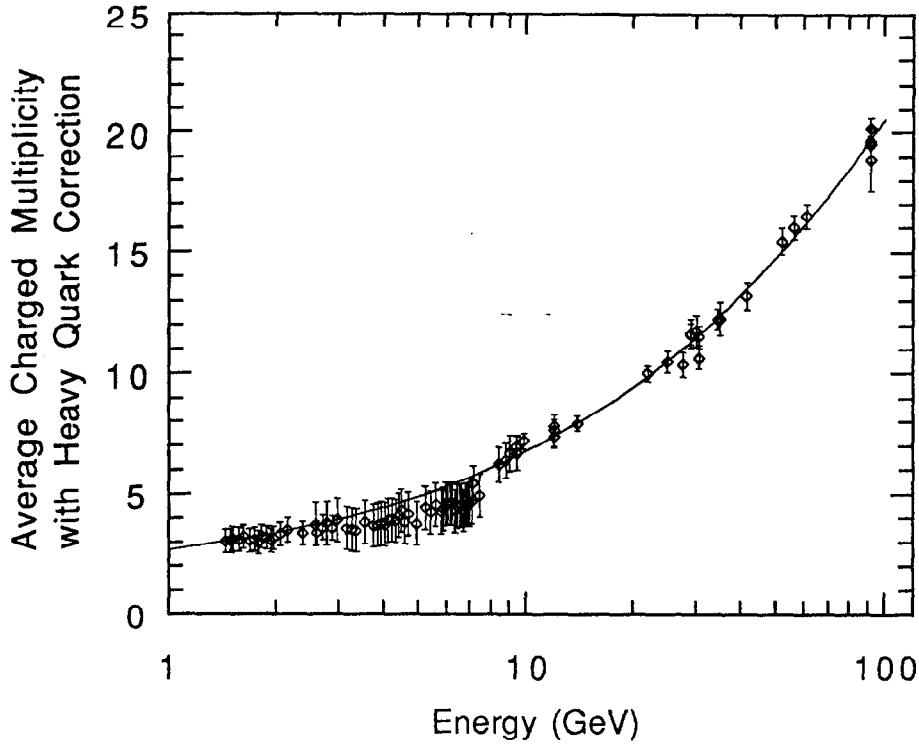

Figure 7–5 World sample of charged multiplicity data, corrected to remove the effects of heavy quark production. The line is a fit of the LLA-inspired form to this data.

also shown as the dashed line in Figure 7–4, where it lies below the *udscb* data points.

It should be noted that, in basing this correct on measurements of the $c\bar{c}$ and $b\bar{b}$ multiplicities at 29 GeV, we have introduced an additional systematic error of ±0.5 tracks in the multiplicity comparison. While this is small compared to the statistical error in the non-leading multiplicity, it is nevertheless one of the largest systematic errors, and thus may possibly determine the degree of accuracy with which this comparison can be made in the high-statistics limit. It may well be that this uncertainty could be reduced by considering the measurements of the *difference* between $c\bar{c}$, $b\bar{b}$ and *udscb* multiplicities, rather than considering the measurements separately as has been done before.

7.6.2 Non-leading Energy and x_E-distribution Bias

Because the x_E distribution is not a δ-function, but is instead a rather broad function presumably related to the Peterson function, and because the relationship between the average multiplicity and E_{cm} is not linear, the mean non-leading multiplicity expected for a given $\langle x_E \rangle$ is not quite equal to the mean total

multiplicity measured at a lower center-of-mass energy equal to average non-leading energy,

$$\langle E_{nl} \rangle = E_{cm}(1 - \langle x_E \rangle). \tag{7-16}$$

Mathematically, this accounts for the fact that the non-leading multiplicity measures the multiplicity at a distribution of energies is given by

$$\langle \bar{n}(E_{nl}) \rangle = \int \bar{n}(E_{nl}) P(E_{\bar{n}l}) dE_{nl}, \tag{7-17}$$

whereas the multiplicity at $\langle E_{nl} \rangle$ is

$$\bar{n}(\langle E_{nl} \rangle) = \bar{n}[\int E_{nl} P(E_{nl}) dE_{nl}] \tag{7-18}$$

where $\bar{n}$ is the function which relates center-of-mass energy to the mean total multiplicity and $P(E_{nl})$ is the normalized non-leading energy distribution which is given by a convolution of the $1 - x_E$ distributions for the two B hadrons in the event. In the following comparisons between the non-leading multiplicity and lower energy total multiplicity data, this is accounted for by the application of a correction to the non-leading energy. The corrections used are given in Table 7–11. These

E_{cm} (GeV) and heavy quark type	$\langle x_E \rangle$ (no ISR)	x_E dist. corr. (GeV)	$\langle E_{nl} \rangle$ (GeV)
29 GeV ($c\bar{c}$)	0.562	–0.24	12.46
29 GeV ($b\bar{b}$)	0.751	–0.10	7.12
35 GeV ($b\bar{b}$)	0.740	–0.35	8.75
42.1 GeV ($b\bar{b}$)	0.727	–0.45	11.04
90.9 GeV ($b\bar{b}$)	0.697	–1.50	26.05

Table 7–11 The non-leading energies and the associated x-distribution correction at which the previous measurements of the non-leading multiplicity were done.

corrections have been calculated assuming a Peterson fragmentation function. The values for $\langle x_E \rangle$ at PEP/PETRA energies were calculated using the values and prescription as described by Chrin,[42] except with initial state radiation (ISR) off. This is because multiplicities are customarily quoted at the nominal E_{cm} and are corrected to remove ISR.

The non-leading energies used for comparison to the total multiplicity data, for this measurement as well as for the PEP and PETRA measurements, are shown in Table 7–12, along with the non-leading multiplicity values. It should be pointed out

experiment and heavy quark type	E_{cm} (GeV)	$\bar{n}_b$ or $\bar{n}_c$	$\bar{n}_{nl}$	$\langle E_{nl} \rangle$ (GeV)
Mark II $(b\bar{b})$[37]	29	16.1±1.1	5.1±1.1	7.12
Mark II $(c\bar{c})$[37]	29	13.2±1.0	8.1±1.0	12.46
DELCO $(b\bar{b})$[39]	29	14.32±0.92	3.31±1.20	7.12
TPC $(b\bar{b})$[40]	29	16.7±1.0	5.7±1.0	7.12
TPC $(c\bar{c})$[40]	29	13.5±0.9	8.4±0.9	12.46
TASSO $(b\bar{b})$[41]	35	15.96±1.43	4.95±1.44	8.75
TASSO $(b\bar{b})$[41]	42.1	17.02±1.98	6.01±1.99	11.04
this meas. $(b\bar{b})$	90.9	23.05±1.92	12.04±1.93	26.05

Table 7–12 The b or c event multiplicities, corresponding non-leading multiplicities and corrected non-leading energies are given with their total statistical and systematic error for previous experiments and this measurement. The b non-leading multiplicities were calculated using an average B decay multiplicity of 11.01±0.20 (see Section 7.5). The c non-leading multiplicities were calculated assuming 5.1±0.3 tracks for the average charm hadron decay multiplicity, as used in these measurements.

that the PEP and PETRA experiments have chosen to take initial state radiation into account by correcting their measured $b\bar{b}$ multiplicity back to the nominal beam energies. On the other hand, $\langle x_E \rangle_b$ is quoted in terms of the *uncorrected* beam energy, and so initial state radiation must be added back into E_{cm} before multiplying by $\langle x_E \rangle_b$ to get the non-leading energy. Since events with very energetic initial state radiation will fail hadronic cuts, this effect is detector dependent. The average energy lost to initial state radiation at PEP and PETRA energies has been estimated to be 1.0±0.5 GeV. This correction has been applied to the PEP and PETRA energies, and the uncertainty included. For our measurement at the Z^0 uncorrected beam energy of 90.9 GeV is used as a starting point.

7.6.3 Leading Contribution in Light Quark Decay

One might expect that the comparison with the non-leading multiplicity from heavy quark decays at higher energy might be most properly done with only the non-leading portion of the light quark decays at lower energy. Again, the Lund Monte Carlo can be used to derive a correction to the multiplicity data, although in this case the correction is somewhat model dependent since it can not be tied to an independent measurement, as can the heavy quark correction. This correction, from the multiplicity in *uds* decays to the non-leading multiplicity in *uds* decays, has the form

$$\delta_{\bar{n}} = a' + b' \cdot \log_{10}(E_{cm})$$

where $a' = -0.724$, $b' = 0.970$ and E_{cm} is in GeV. At 30 GeV, for instance, the size of this correction is +0.71 tracks. The correction is derived by removing the leading (most energetic) particle, or its decay products, in each hemisphere from both the multiplicity sum and the center-of-mass energy. The result of this correction is plotted as the dotted line in Figure 7–4.

The correction for the effects of the leading particles should be interpreted as a check of the dependence of the multiplicity comparison and later, in the opposite fashion, the extraction of $\langle x_E \rangle_b$, on the theoretical uncertainty in the underlying assumptions. These assumptions include those regarding the process of non-leading particle production, and specifically the relationship of the non-leading particle multiplicity and the non-leading energy. Nonetheless, that the difference of approximately 0.7 tracks between this leading particle-corrected multiplicity function and the multiplicity function with only the heavy quark correction is on the same order as the total systematic error indicates that the overall approach is robust. This illustrates that this is another area (along with the non-leading reconstruction constant and heavy quark correction) which could benefit from additional theoretical study. Consequently, for the final results derived in the following sections only the heavy quark and the x_E-distribution corrections are used.

7.6.4 Multiplicity Comparison

Figure 7–6 shows the world sample of multiplicity data, and the heavy quark-corrected multiplicity fit (see Section 7.6.1 for a description of this correction). Plotted over this are the non-leading multiplicity points from Table 7–12, which include the x_E-distribution correction described in the previous section. To the level

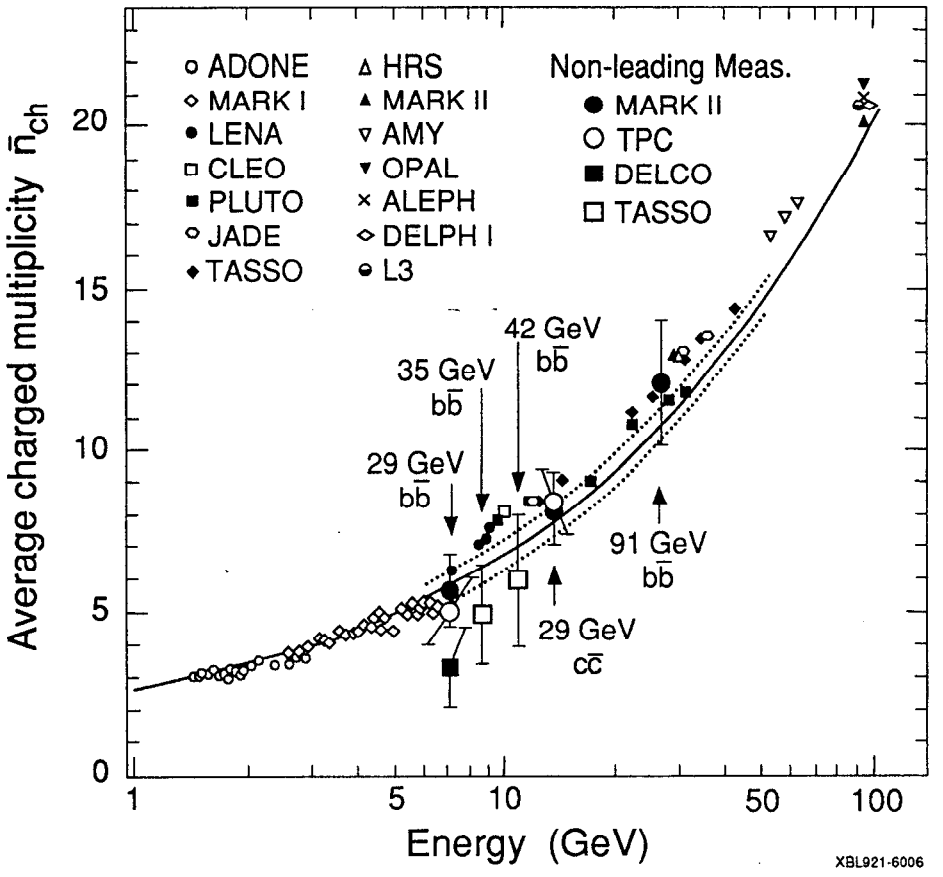

Figure 7–6 World sample of charged multiplicity data, without error bars, and the heavy quark corrected fit from Figure 7–4 and Figure 7–5. The dotted line is the ±0.5 track uncertainty resulting from the normalization of the heavy quark correction to PEP and PETRA data. Also shown are the non-leading multiplicity measurements from previous experiments and this analysis, plotted at the appropriate x_E-distribution corrected non-leading energy, as listed in Table 7–12. (The effects from the leading quark in *uds* events are not included as discussed in Section 7.6.3). The assumption of flavor independence for the fragmentation process predicts that the non-leading data should fall on the solid line.

of experimental accuracy available, that the points lie on the corrected multiplicity curve, represented by the solid line, confirms the prediction of the flavor independence of the fragmentation process on the initial quark flavor. The highest energy point, from this study, serves to strengthen the quality of the check available from the lower energy measurements alone.

Finally, should this measurement be pushed at LEP, and an effort made to better understand the theoretical underpinnings of the measurement, it should be pointed out that there is a limit to the accuracy of the comparison imposed by the uncertainty in the measurement of $\bar{n}$ at lower energy. This is most likely a hard limit, since there are no plans for more running at intermediate energies (around 30 GeV). Fortunately, the centroid of the non-leading energy distribution for $Z^0 \rightarrow b\bar{b}$ decay falls in a region, where $\bar{n}$ has been well measured by five of the PEP and PETRA collaborations. Correcting for the small energy differences and combining the five measurements closest to 30 GeV[140] gives an uncertainty in $\bar{n}$ of ± 0.21 tracks, with a $\chi^2 = 7.0$ for 4 degrees of freedom. Thus, depending on how much the various systematic problems mentioned above can be brought under control, it will soon be possible to push this test to an accuracy 4 to 10 times greater than presented here.

7.7 Extraction of the Average x_E

If it is instead assumed that the non-leading fragmentation is indeed independent of the flavor of the leading quarks, it is possible to estimate $\langle x_E \rangle_b$ from the non-leading multiplicity, essentially by reading off the non-leading energy from the $\bar{n}$ versus E_{cm} plot. For $\langle x_E \rangle_b \sim 0.7$, the relevant range of E_{cm} for this measurement is between 15 and 45 GeV. The value of $\langle x_E \rangle_b$ is determined by the value of $\bar{n}$ at the central value of $E_{cm} \sim 30$ GeV, while the uncertainty in $\langle x_E \rangle_b$ will be given by the slope of the $\bar{n}$ dependence upon E_{cm}, which in this range is given by the low energy PETRA data and the TRISTAN data. Figure 7–7(a) shows the fit to the LLA inspired form as discussed previously,

$$\bar{n}_{had} = a + b \cdot \exp\{c\sqrt{\ln E_{cm}}\} \tag{7-19}$$

with $a = 4.684$, $b = 0.511$ and $c = 2.736$. Figure 7–7(b) shows the residuals from this fit as a function of energy. All corrections discussed previously, the heavy quark correction, removing the effects of the leading particles and the x_E-distribution corrections, can then be applied to the results of this fit, although none have been included in Figure 7–7(a). The value of $\langle x_E \rangle_b$, with errors, is then found by solving the above equation, with the desired correction included, for the center-of-mass energy corresponding to the measured non-leading multiplicity. As a correction to the charged multiplicity, rather than a correction to the energy, the x_E-distribution correction has the approximate form $\delta\bar{n} = -141 \cdot E_{cm}^{-1.80}$, such that at 30 GeV, it is

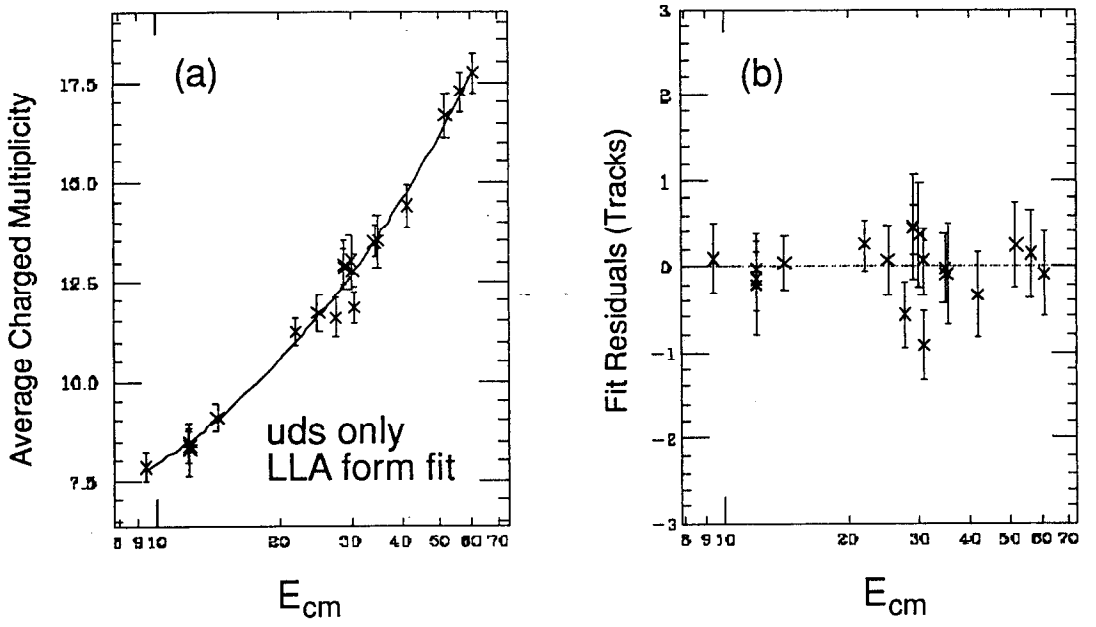

Figure 7–7 (a) Data and fit to the LLA-inspired form for total multiplicity restricted to the data from PEP, PETRA, and TRISTAN, for extraction of the mean x_E. (b) Residuals from the fit.

–0.31 tracks. For example, with the heavy quark and x_E-distribution corrections applied, the corrected fit is

$$\bar{n}_{had} = 3.484 + 0.511 \cdot \exp\{2.736\sqrt{\ln E_{cm}}\} - 141 \cdot E_{cm}^{-1.80}. \qquad (7\text{-}20)$$

Table 7–13 shows the results for $\langle x_E \rangle_b$, including statistical error only, for each of the three tags. In addition to systematic effects enumerated in the previous

tag	no correction	add x_E distribution correction	also add heavy quark correction	also add non-leading, correction
EV2	$0.701^{+.095}_{-.103}$	$0683^{+.082}_{-.097}$	$\mathbf{0.619^{+.096}_{-.107}}$	$0.659^{+.085}_{-.096}$
EV3	$0667^{+.098}_{-.120}$	$0.650^{+.092}_{-.114}$	$0.583^{+.102}_{-.124}$	$0.627^{+.089}_{-.111}$
HE2	$0.665^{+.105}_{-.124}$	$0649^{+.098}_{-.119}$	$0.581^{+.110}_{-.130}$	$0626^{+.096}_{-.117}$

Table 7–13 The values of $\langle x_E \rangle_b$ calculated with the different corrections as described in text. The EV2 value with the x_E-distribution and heavy quark corrections is taken as our final result.

section, the systematic error must include a contribution of 0.5 tracks due to the

uncertainty in the heavy quark correction. For the fit with the heavy quark and x_E-distribution corrections, which is taken as the final measurement, the resulting total systematic error of ±0.80 tracks yields

$$\langle x_E \rangle_b = 0.619^{+.096\ +.043}_{-.107\ -.046}.$$

where the errors are statistical and systematic, respectively. Thus, to its rather limited level of statistical accuracy, this approach provides a result in agreement with the current LEP average of 0.697±0.013,[22][23][24] and thus has provided an important independent check of the $\langle x_E \rangle_b$ measurements which use the lepton momentum spectrum.

In the future, the LEP experiments should be able to exceed the systematic error limit quoted here. This should provide a very meaningful check of the B hadron fragmentation energy, which is a critical parameter in the measurement of various parameters associated with $Z^0 \to b\bar{b}$ decays (branching fraction, lifetimes, exclusive branching fractions, *etc.*)

Appendix A

Limits on B_s Production at the Z from B Mixing Measurements

It is useful in the measurement of the non-leading multiplicity in $Z^0 \to b\bar{b}$ events, to place a limit on the production of the various bottom hadron species. Though little direct information on the production fractions exists, one can limit the B_s production fraction, $P(b \to B_s)$, using the present measurements of $B\bar{B}$ mixing and assuming a constraint from the Standard Model. The strength of the mixing can be parameterized as[141]

$$\chi \equiv \frac{N(BB) + N(\bar{B}\bar{B})}{N(b\bar{b})}, \tag{A-1}$$

which is the ratio of the number of mixed events to the total number of produced $b\bar{b}$ events. If the B-mixing is large enough that the meson could mix many times before the B decays ('full mixing'), then χ tends toward 0.5. To determine the level of B_s mixing, one notes that the Standard Model places a constraint on the relative mixing strengths of B_d and B_s, resulting from the unitarity of the Kobayashi-Maskawa (KM) matrix, that

$$\frac{|V_{td}|^2}{|V_{ts}|^2} > 0.21. \tag{A-2}$$

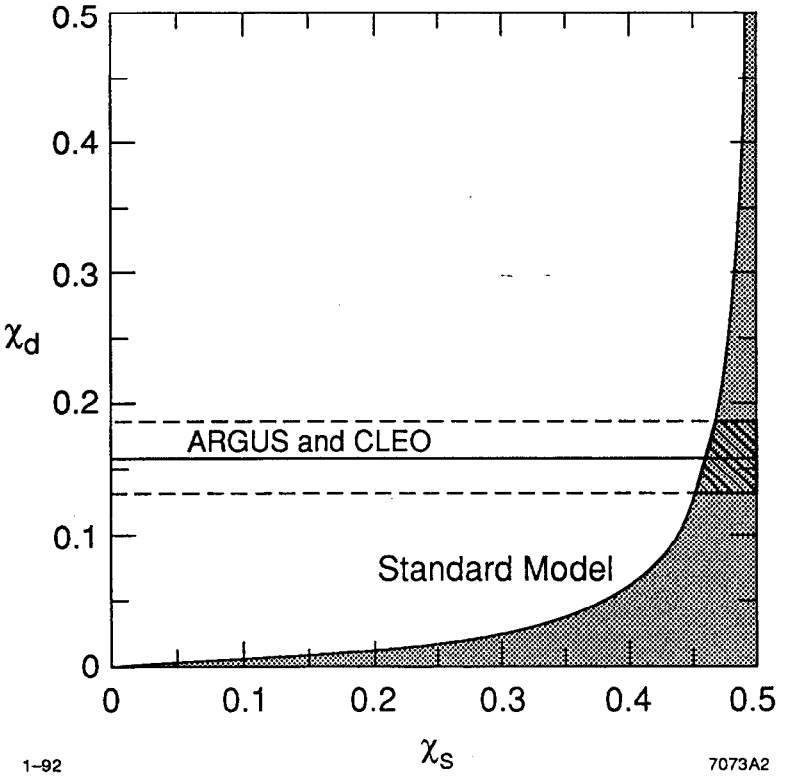

Figure A–1 The allowed regions for B_d mixing from the CLEO and ARGUS experiments[126] and the constraint from the standard model are shown. The combination of these indicates that B_s mixing is nearly maximal.

The ratio of the B_d to B_s mixing rates (x_d/x_s) will then, to within small uncertainty, be proportional to this ratio of KM elements and x_i is then related to χ_i by

$$x_i = \sqrt{\frac{2\chi_i}{1-2\chi_i}}. \qquad \text{(A-3)}$$

The mixing of the B_d has been measured by CLEO and ARGUS at the $\Upsilon(4s)$, where no B_s is produced, and yields an average value of $\chi_d = 0.155 \pm 0.043$.[126] Using the Standard Model constraint in conjuction with the CLEO and ARGUS measurement of χ_d, it can be seen in Figure A–1 that B_s must be almost fully mixed, namely $0.45 < \chi_s < 0.5$.

At the Z^0, the mixing will be a linear combination of the B_d and B_s mixing strengths,

$$\chi(Z^0) = f_d\chi_d + f_s\chi_s, \tag{A-4}$$

where f_d and f_s are the B_d and B_s fractions, with

$$f_u + f_d + f_s + f_{B\ baryon} = 1. \tag{A-5}$$

The LEP experiments have measured the mixing to be $\chi(Z^0) = 0.143 \pm 0.023$.[126] To place a limit on f_s, Equations (A-4) and (A-5) can be solved to yield,

$$f_s = \frac{2\chi(Z^0) - (1 - f_{B\ baryon})\chi_d}{2\chi_s - \chi_d} \tag{A-6}$$

with the assumption that $f_u = f_d$. Using the above values for χ_d and χ_s, and assuming that $f_{B\ baryon} = 0.1 \pm 0.1$, the $b \rightarrow B_s$ fraction is found to be 0.18±0.10, which is consistent with the Lund value of 0.12.

Appendix B

DCVD Gas and Temperature Control Systems

The operation of the DCVD in the unsaturated regime placed stringent constraints on the gas parameters such as its composition and temperature. This appendix discusses the apparatus used to investigate and maintain the required gas properties.

B.1 Gas Properties Overview

The gas used in the DCVD was a mixture of 92% CO_2 and 8% C_2H_6. The nominal gas pressure during the 1990 operation at the SLC was 2 atmospheres (absolute), although the chamber ran at 3 atm for much of its check-out prior to installation. At either operating pressure, the nominal reduced drift field, E/P, was 0.77 kV/cm/atm. With this field, the drift velocity is typically about 5.7 μm/ns. The drift velocity in this regime is unsaturated, which means that it depends acutely on the environmental conditions. This dependence can be expressed as

$$v_d \propto \frac{\mathrm{E}}{\mathrm{P}} f(\mathrm{T}, \text{gas composition}) .$$

The drift velocity depends linearly on the reduced electric field, and will also have a non-trivial dependence on the gas temperature and composition. Furthermore, because the drift velocity is so low and the maximum drift distance fairly long

(about 5 cm), the electronegative impurities in the gas must be kept to a minimum in order to maintain a minimum loss of signal during the electron drift. In order to minimize the influence of these environmental properties on the drift velocity and hence the time-distance relation, the goal was to control these parameters adequately to maintain a drift velocity variation of less than 0.05%. As discussed in Section 2.2.3.3 on page 56, the electric field strength was maintained within the required tolerances by the DCVD high voltage system.

B.2 Gas Delivery System

The gas delivery system for the DCVD was designed to handle a number of responsibilities. Specifically, it was required that the gas delivery system

- supply gas as free of impurities as possible,
- monitor and maintain a constant gas composition, and
- monitor and control the gas pressure.

The entire gas system appears reasonably complex, in part because it was designed to be flexible enough to work with a variety of gas quality control and monitoring devices. A diagram of the system can be found in Figure B–1. The system does not re-circulate the gas, but just vents the gas after passing through the chamber.

B.2.1 Mechanical Assembly

The mechanical assembly of the plumbing for the gas panel used 0.25 inch diameter oxygen-free high-conductivity (OFHC) copper tubing, which was cleaned in a solvent to remove any oils and then fired in a hydrogen furnace to remove any remaining volatile compounds. The connections were made with brass Swagelok compression fittings,* which were cleaned with an ultrasonic cleaner before use. All valves were brass Nupro H-Series bellows valves and were ordered fully cleaned. These valves contained no non-metal seals which could potentially contaminate the gas. The bulk of the gas delivery system shown in Figure B–1 was mounted on a large gas panel and was located next to the Mark II counting house.

To ensure the integrity of the system when it was fully assembled and connected to the DCVD, a helium mass-spectrometer leak detector was used. It was found that these fittings could routinely achieve full vacuum leak-tightness when properly tightened. Furthermore, no leaks could be detected from any of the pressure seals on the DCVD itself.

* The Swagelok fittings and Nupro valves are manufactured by the Crawford Fitting Company of Solon, Ohio.

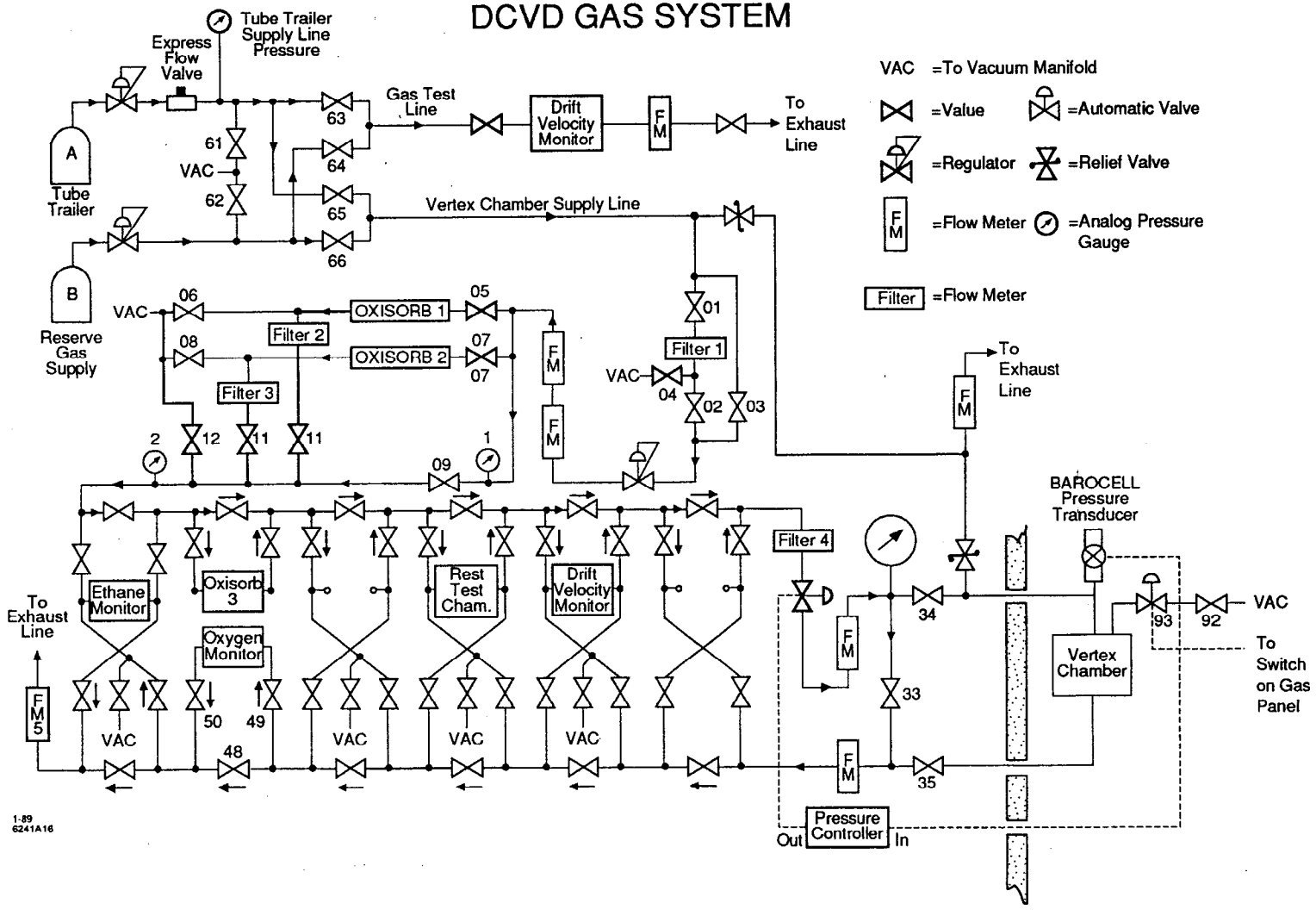

Figure B–1 A schematic diagram of the gas system for the DCVD.

Because the DCVD could be pumped to a vacuum, a 0.875 inch diameter vacuum manifold went from a mechanical vacuum pump placed by the gas panel, out to the Mark II magnet iron, about 15 feet from the chamber. A pneumatically controlled vacuum valve was located there to seal the chamber from the vacuum manifold. The final 15 feet of vacuum manifold was comprised of 0.5 inch OFHC copper tubing, as this was in constant contact with the gas in the chamber.

B.2.2 Gas Source

The gas supply for the 1990 run was two large tube trailers containing the CO_2/C_2H_6 gas mixture. The gas was mixed commercially by the Liquid Carbonic Company and required to meet purity specifications. It was standard to also test the gas locally using our gas monitoring equipment, as discussed later. Typical gas shipments would contain as much as 3 ppm of oxygen as the primary electronegative contaminant. Contamination of other organic compounds, as measured by the supplier, were usually less than 100 ppm. Using the tube trailers was particularly advantageous, as it ensured a constant gas composition for extended periods. At the nominal gas flow rates of 1–2 scfh, a tube trailer would last for at least six months of operation. The gas pressure of the tube trailer when supplied was about 500 lbs, which is below the pressure at which the CO_2 would liquify. The gas pressure was regulated down to about 80 psi for the transfer line to the gas panel. Mounted on each tube trailer was an excess flow valve, designed to close automatically should the flow rate get too large (as in the case of a broken supply line, *etc.*)

B.2.3 Elements of the Gas System

At the gas panel, the gas was routed through a pair of Oxisorb units which remove virtually all of the trace amount of oxygen in the gas. Two units were used because the small units tended to last only about two weeks, depending on the oxygen level in the incident gas. Several particulate filters were used to ensure that the chamber was not contaminated by any solid material. The specifications for the Oxisorb units stated that they would lower the oxygen level to less than 0.1 ppm when the inlet gas is not greater than 15 ppm. This performance is consistent with the observations made with our monitoring equipment.

The last item on the gas panel before the supply line to the chamber was an electronically controlled regulator valve for active pressure control. The pressure in the chamber was measured by a Barocell Pressure Transducer, mounted on the end of the 0.5 inch vacuum manifold, about 15 feet from the chamber. This transducer

was connected to a Datametrics Type 1501 Pressure Controller. The controller incorporated an electronic feedback system and would adjust a regulator valve placed on the gas panel just prior to the supply line to the chamber. The desired pressure was set with a dial switch on the controller.

After the chamber, the gas would flow through some of the gas monitoring equipment such as the Drift Velocity Monitor (DVM), the oxygen monitor and the ethane monitor. The DVM was a device for monitoring the drift velocity and electron lifetime of the gas, and is discussed below in Section B.4.1. It was not operated continuously, as were the other monitors, but rather was used for studies of gas properties and for verifying the quality of new gas shipments.

The oxygen level in the gas was measured by a Model 316 Oxygen Analyzer produced by Teledyne Analytical Instruments. This device uses a fuel cell to electrochemically measure the concentration of oxygen in a gas. It can measure levels from a few parts per million up to 21%. Although intended to be calibrated with air, the cell type which was required for use in CO_2 had a very long recovery time until it would again be sensitive on the few ppm level. Consequently, we employed a standard reference bottle of CO_2 with about 80 ppm O_2 to provide at least a very good relative oxygen determination. This unit was used continuously as a warning device of possible problems during the 1990 data runs.

The percentage of ethane in the gas was measured by a Teledyne Model 235 Thermal Conductivity Analyzer. This analyzer determines the fraction of C_2H_6 by comparing the thermal conductivity of the sample gas to that of a reference sample of pure CO_2. The accuracy of this device is 0.01% ethane.

The pressure measurement, oxygen level and ethane fraction were read out through a 14-bit CAMAC analog-to-digital converter to the VAX host computer. The Mark II environmental monitoring routine, which recorded information for all the various Mark II systems would record the gas monitoring information to the data tape every four minutes. This program would also check that the various values were within preset limits and alert the physicists on shift of a potential problem. The pressure measurement was also connected to a hardware DCVD alarm interlock which would trip the DCVD high voltage should the gas pressure drop too low.

The gas system data recorded by the VAX can be used to characterize the long term performance of the gas system. The oxygen and ethane levels were virtually constant throughout the entire running. Typically the pressure would be held constant to better than 0.01 psi (0.03%) over periods of weeks, although some shifts

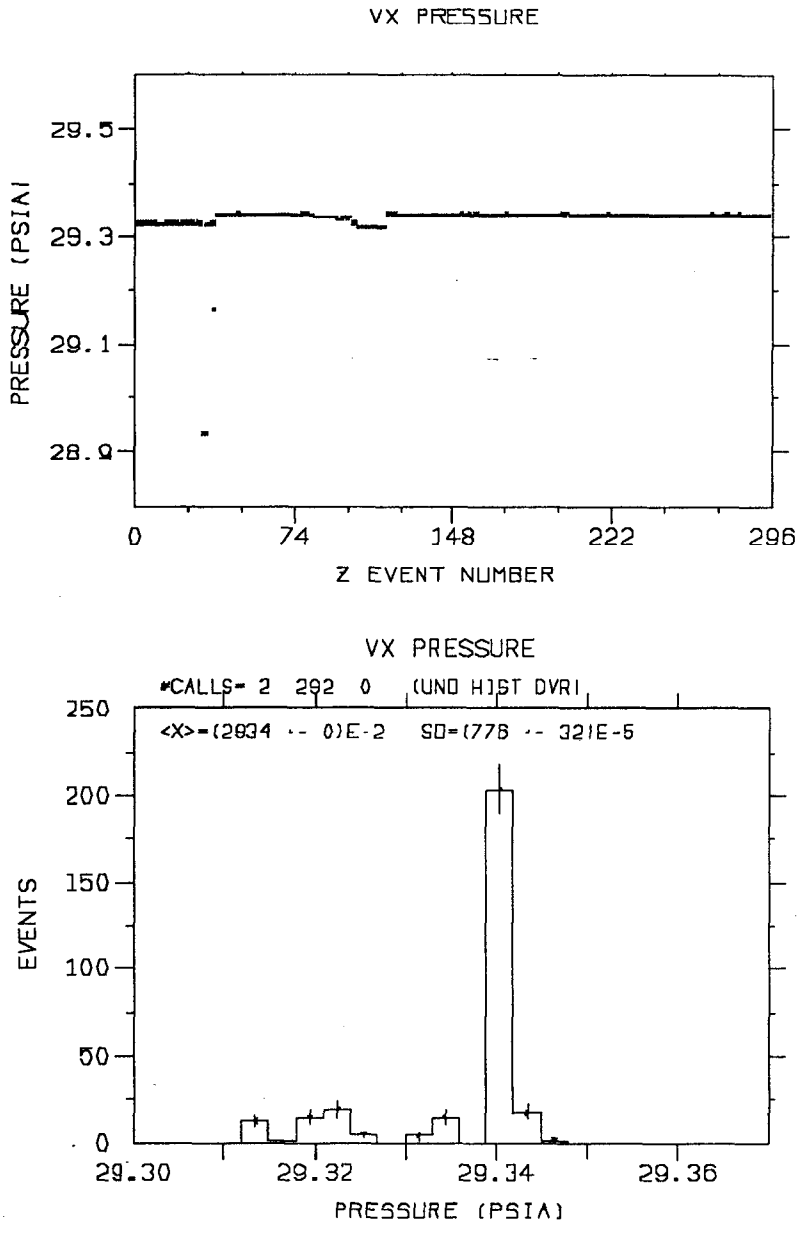

Figure B–2 Measured DCVD pressure for all of the 294 triggered Z events. The two low points we during periods when the pressure control malfunctioned.

were seen on the order of 0.02 psi at a few points during the run. The pressure which was recorded closest to each recorded Z trigger is shown in Figure B–2. Neglecting two very low points when the pressure control was malfunctioning, the rms pressure is 0.007 psi over all of the Z events.

B.3 Temperature Control System

The temperature of the DCVD was monitored and controlled by a computer controlled feedback system which circulated water around the outside of the chamber. The goal of this system was to achieve temperature stability and uniformity within the chamber.

B.3.1 Temperature Measurement

The temperature of the DCVD was measured by a series of 48 thermistors placed in and around the chamber. These thermistors were individually calibrated with respect to a reference thermistor to correct for relative offsets. Over the typical temperature ranges of 25 to 35° C, the temperature response was not significantly different among thermistors to require more than a single offset correction. The average offset correction was equivalent to less than 0.05° C. After the thermistors were installed in the DCVD, the entire chamber was placed inside of a foam container and allowed to equilibrate thermally. Further, generally small, offset corrections were made from this test.

The thermistors on the chamber were placed in a number of locations. These included:

- on the outer surface of the inner and outer shells
- on the aluminum supports for the Macor wire-foundations, which are inside the gas volume
- on the pressure heads
- in the high voltage faraday cages
- in the air outside of the DCVD
- on the CDC inner core
- in the water lines which circulate water around the DCVD

The best measurement of the internal chamber temperature came from the thermistors mounted on the aluminum supports for the Macor foundations, as these are the most de-coupled from surfaces with the temperature control water lines.

The thermistor resistances were converted to a voltage signal using custom electronics containing 64 thermistor channels. These temperature signals were read out to the VAX host computer via the same CAMAC ADC's as used for the pressure system. The temperature signals were read in every 12 seconds and corrected in software to account for the individual thermistor calibrations. These temperatures

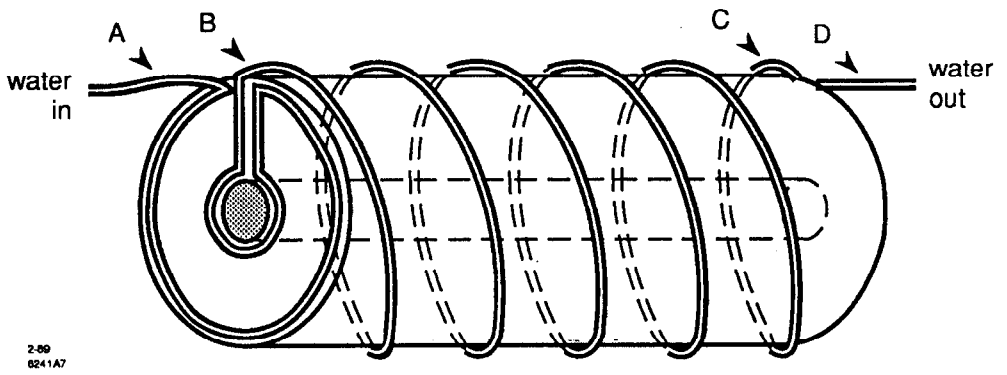

Figure B–3 Water tubing around the pressure heads and the outer shell of the DCVD. The letters indicate the positions of the thermistors in the water supply lines.

were recorded to the data tape every four minutes and were used for the active temperature control discussed in the next section.

B.3.2 Temperature Control

The temperature of the DCVD was controlled by circulating water from a temperature-controlled reservoir around the DCVD. The water would first go around the pressure head on the inner and outer radius, then around the outer shell in a helical pattern and finally around the pressure head on the other end of the chamber, as shown in Figure B–3.

The system to circulate the water to the DCVD is shown schematically in Figure B–4. The temperature controlled reservoir was a Haake N2-R Digital cryostat. It was comprised of a 15 liter reservoir, which contained a compressor for a constant rate of cooling, and a control unit mounted atop the reservoir which handled the temperature control by use of a heating coil. The specifications for this unit claim a temperature control of ±0.1° C with their internal hardware feedback circuit.

The water from this reservoir was pumped out to the chamber using a Liquiflo 3 gallon per minute (gpm) gear pump. The maximum output pressure of the pump was 100 psi. Typically, the flow rate out to the DCVD would be about 1 gpm, a value which was chosen so that the flow through the 0.25 inch tubing would be on the onset of turbulence for better heat transfer. The supply and return lines to and from the chamber were 0.5 inch insulated aluminum tubing to reduce the pressure drop in these lines. To keep the water in the closed system clean, a UV sterilizer, a de-ionizer and several particulate filters were employed. A hardware alarm system

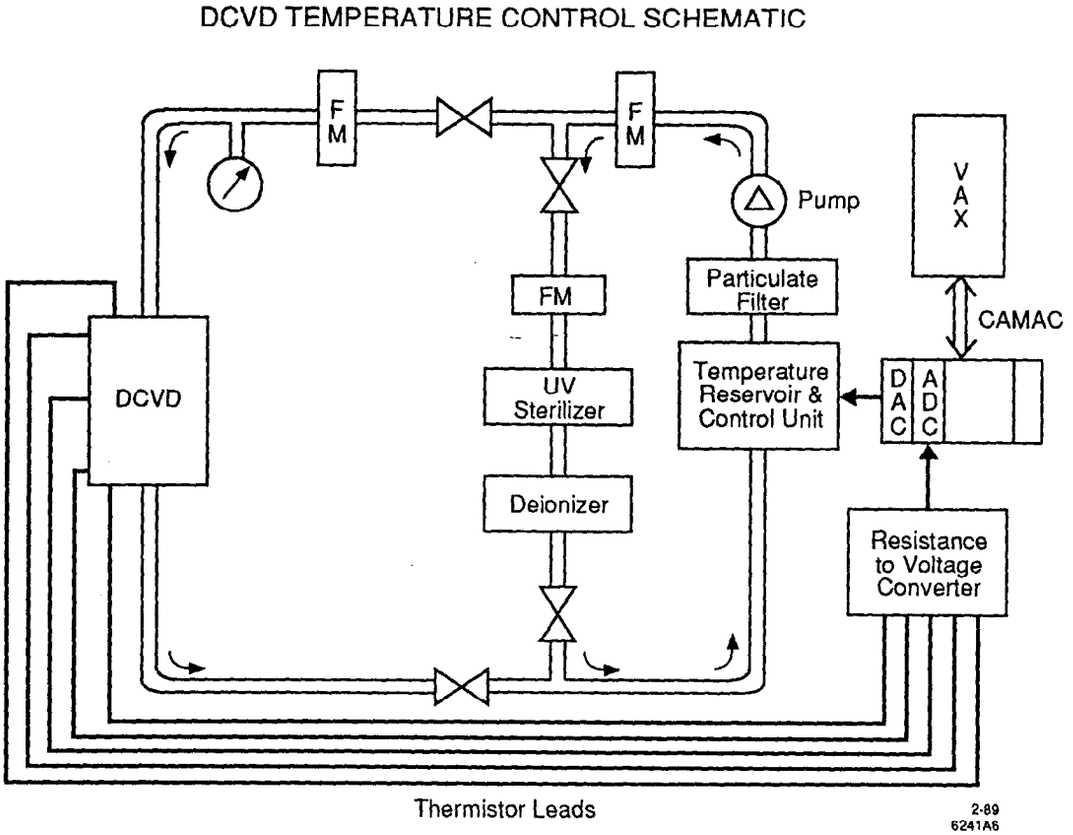

Figure B–4 A schematic diagram of the water circulating temperature control system for the DCVD. The devices labelled FM are flowmeters.

monitored the pressure in the supply line to the chamber and the water level in the reservoir. If an out of tolerance condition was detected, this system would trip an interlock which supplied power to the pump.

The active temperature control was achieved by software which interacted with the Mark II environmental monitoring. Both routines ran on the VAX host computer. With each 12 second interval, the new temperatures would be analyzed and the temperature of the water circulating out to the DCVD appropriately adjusted. This adjustment was made using a 16-bit DAC to which the temperature control unit was adjusted.

The algorithm used to maintain a constant temperature used the two thermistors in the water lines just before and just after the outer shell (thermistors B and C in Figure B–3). The variable to which the temperature feedback system reacted was the average of these two thermistors. These were chosen because the outer shell has the largest surface area in the chamber exposed to the gas volume,

and thus would most substantially affect the gas temperature. The feedback algorithm was quite straightforward. If a temperature adjustment was required, it would vary the temperature voltage signal sent to the temperature controller by the amount of the desired change and then wait for a time period to allow the system to come to thermal equilibrium. This time period would depend on the temperature change which was requested. The hardware alarm system would also check that the voltage signal generated by the DAC corresponded to a reasonable temperature range. If this were not the case the alarm system would substitute a default safe voltage and notify the persons on shift. As the check of last resort, this system also used a thermistor to check the temperature of the water being sent to the DCVD, and if it were out of range the pump interlock would be activated, shutting off water circulation to the chamber.

B.3.3 Temperature Stability and Uniformity

The performance achieved by this system during the 1990 run was quite good. The thermal environment in which the DCVD ran is illustrated in Figure B–5 which shows the temperature outside the chamber yet still inside the central core of the CDC. It is seen that during the 1990 run, the temperature variation spanned a full range of almost 4° C due to external environmental factors. There are clear diurnal variations of about 0.25° C if this temperature is plotted as a function of

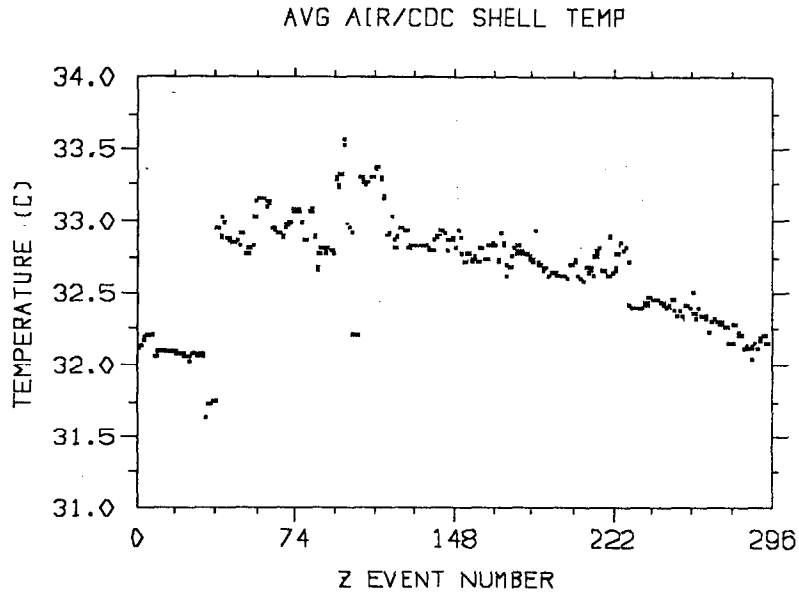

Figure B–5 Temperature in region inside the CDC but outside of the DCVD.

time as well as larger variations corresponding to various systems turning on and off (these systems include the Mark II solenoid, the DCVD high voltage and the SSVD). The chamber temperature as measured by the average of three thermistors placed on the aluminum support for the Macor foundations is shown in Figure B–6. The width of the central peak can be characterized as having an rms width of about 0.02° C. Outside this central peak there are a number of spurious points which were caused by known malfunctions in the temperature control system.

The temperature of the other major surfaces in the chamber, the outer shell and the inner core are shown in Figure B–7. The outer core temperature was very stable, which is expected because the water tubing was connected directly to this surface and the temperature control algorithm used the thermistors before and after the shell for temperature determination. The inner core was not actively temperature controlled and consequently exhibits significant temperature variation. There is virtually no diurnal variation in the inner core. However, temperature changes of ~0.3° C would occur when the SSVD was turned on and off, indicating that, as one might expect, the SSVD is the dominant contributor to the inner core temperature.

Finally there is the question of the temperature uniformity inside the chamber. Figure B–8 illustrates the temperature difference between the ends of the chamber and the temperature difference from the inner core to the outer cylinder. The temperature difference between the ends of the chamber, as measured by the thermistors mounted on the aluminum supports for the Macor wire-foundations, is about 0.12° C with a variation of less than 0.02° C for closely spaced events. This temperature difference is just a consequence of the water temperature warming as it passed from one pressure head to the other due to the heat load of the chamber. The radial temperature difference is larger. Typically the inner core was about 0.5° C warmer than the outer cylinder. Furthermore, as noted previously this temperature difference will vary because the inner cylinder had no active temperature control. This is the largest temperature difference and corresponds to about 0.17%. However, over local blocks of events the variation in this temperature difference is only about 0.1° C.

B.4 Gas Property Studies

A series of studies were done to measure some properties of the CO_2-based gas mixtures. In particular, these investigated the drift velocity dependence on the temperature and the electron lifetime with various chamber additives such as

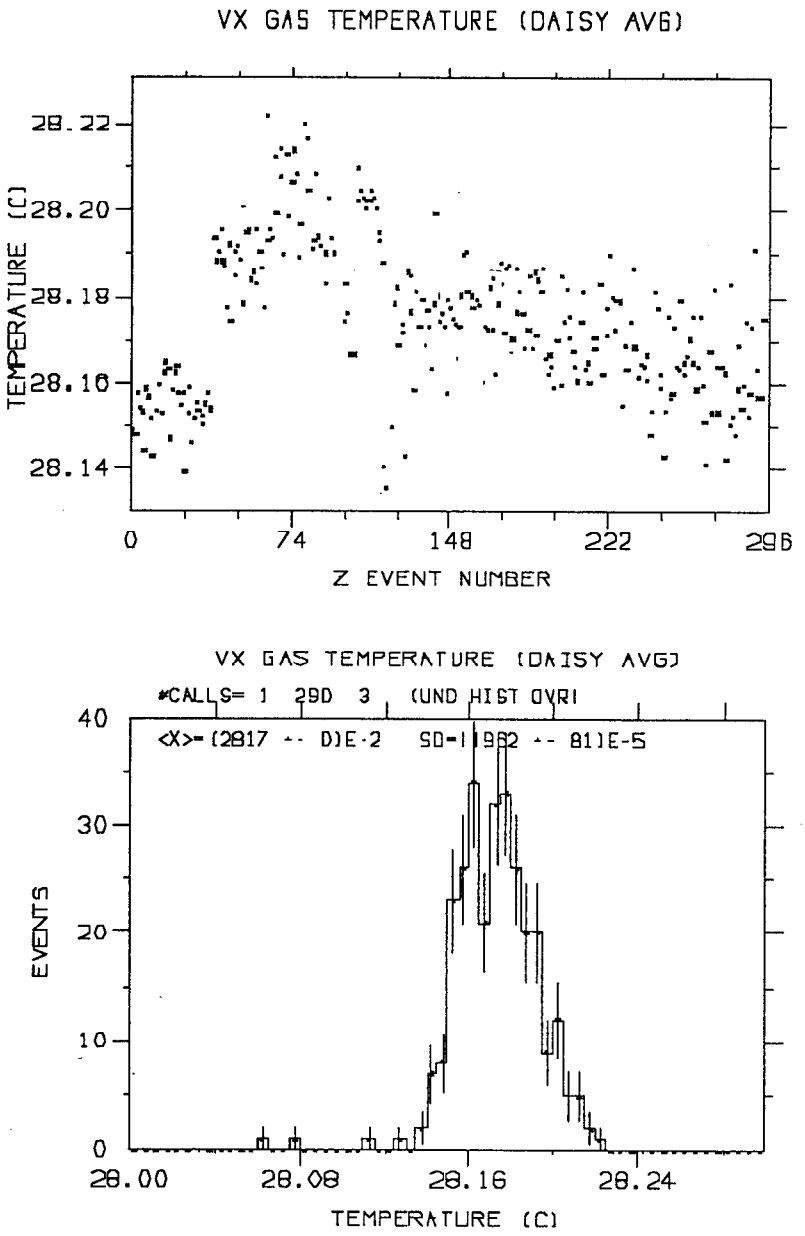

Figure B–6 The nominal temperature inside the DCVD as measured by thermistors placed on the aluminum support for the Macor foundations (the "daisy").

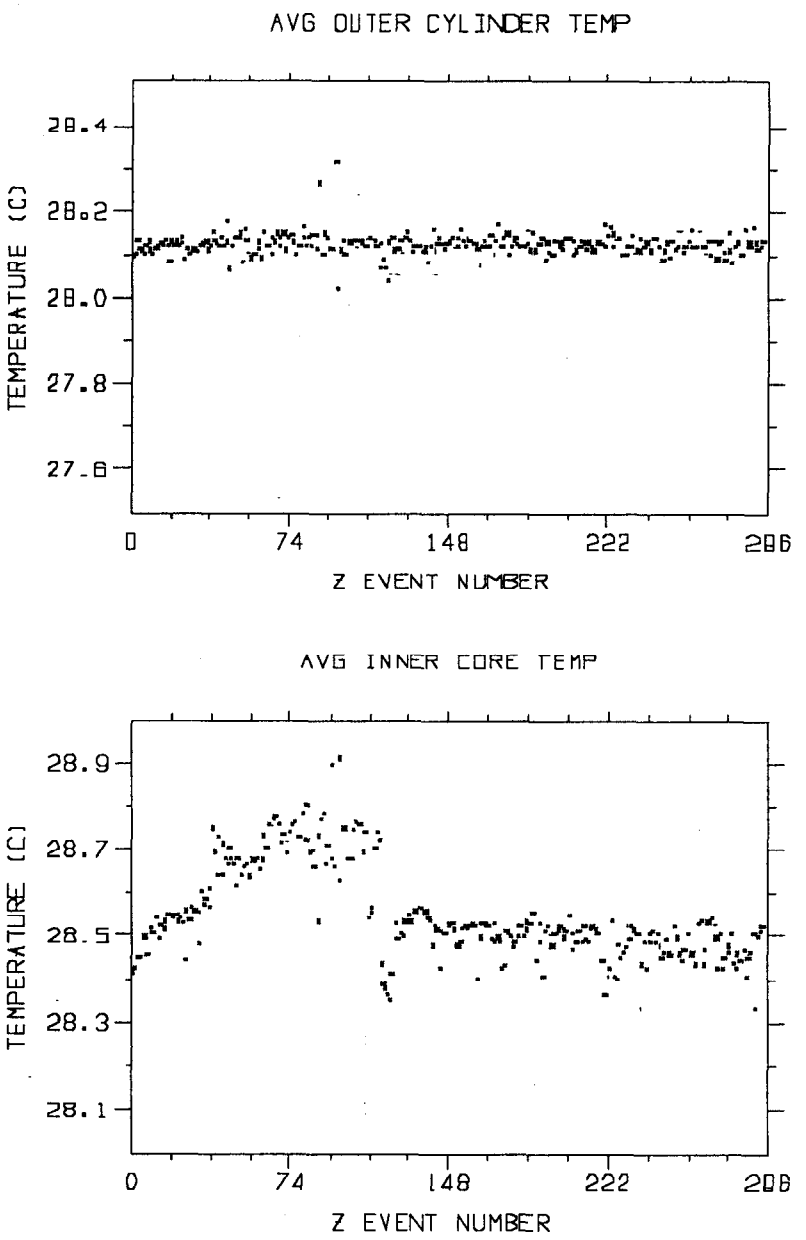

Figure B–7 Temperatures of the outer cylinder and inner core as determined by an average of the thermistors mounted on these surfaces.

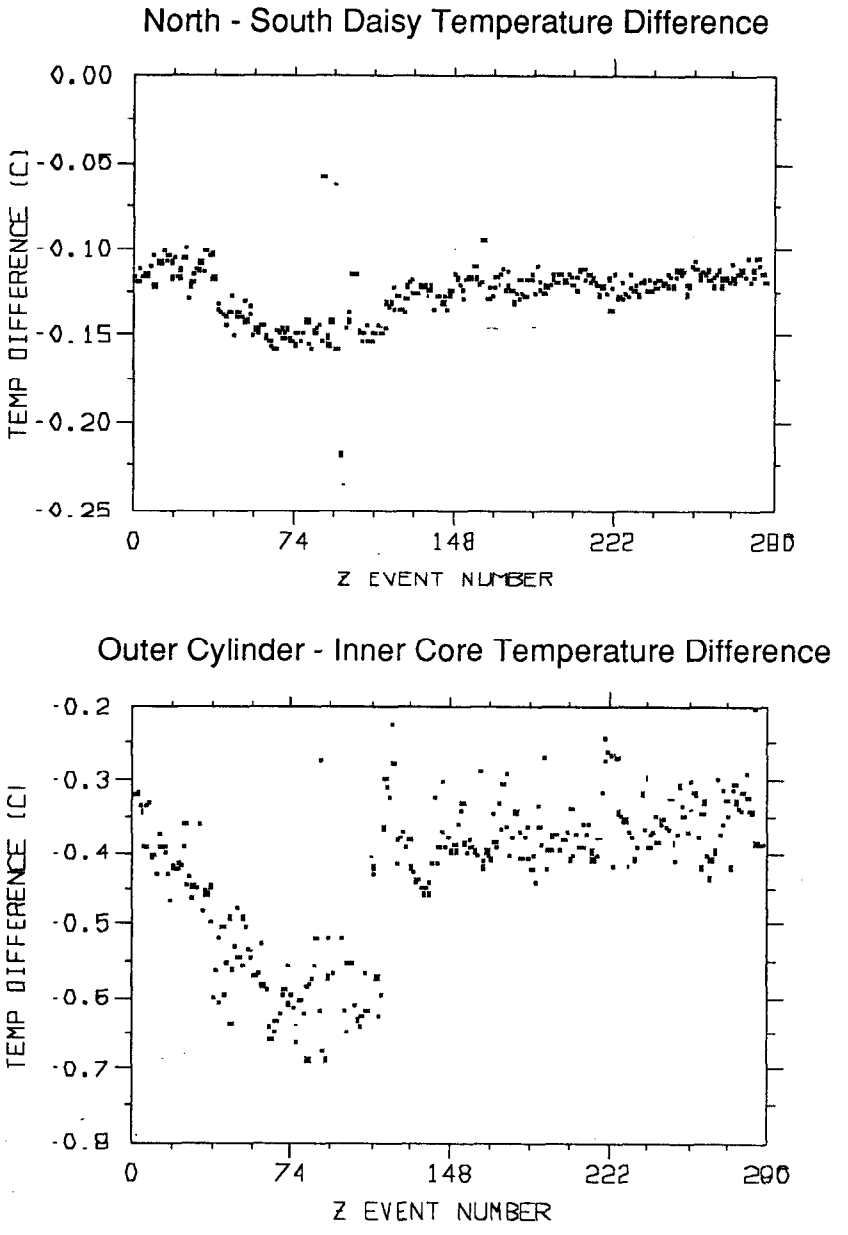

Figure B-8 Temperature differences between the aluminum supports for the Macor on each end of the chamber and between the inner core and outer cylinder.

isopropanol, and most importantly, oxygen. These studies were carried out largely with a small chamber called the Drift Velocity Monitor (DVM). Tests were also done on the tolerance of the gas to radiation. These tests were done in another device, the Radiation Test Chamber (RTC).

B.4.1 Drift Velocity Monitor

The DVM consists of a single 5.08 cm long drift cell, bordered by edge field wires with graded voltages to maintain a uniform electric field in the drift region (see Figure B–9). Electrostatic simulation indicated that the field is uniform to within 0.25% at the center of the cell. Two 1.0 mCi ^{106}Ru were placed within collimators to produce thin beams of 39.4 keV β^-. The β's would produce ionization at two fixed distances from the sense wire and the drift velocity could be obtained from the time difference between their known spatial separation.

The data acquisition electronics for this chamber were quite simple. The pulse from the photomultiplier fed into a discriminator then through a gate-and-delay generator. This signal was then sent to the start input on a Lecroy Model 3001 Multichannel Analyzer ('qVt'), operating in the t-mode. This particular qVt was

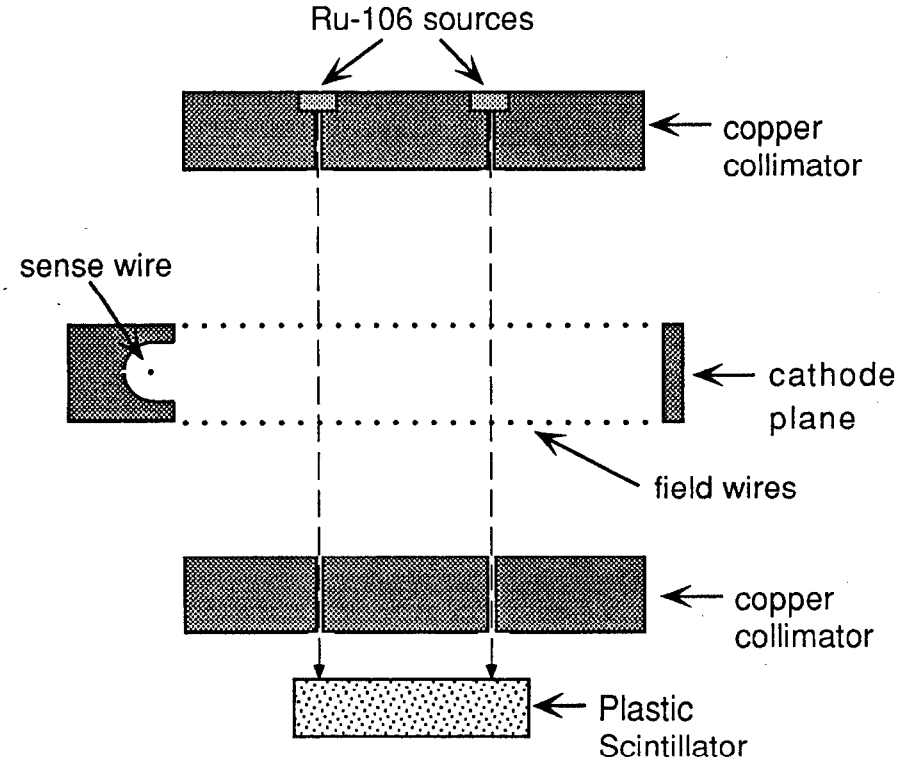

Figure B–9 A schematic illustration of the Drift Velocity Monitor. The paths of the 39.4 keV β^- are shown by the dotted lines.

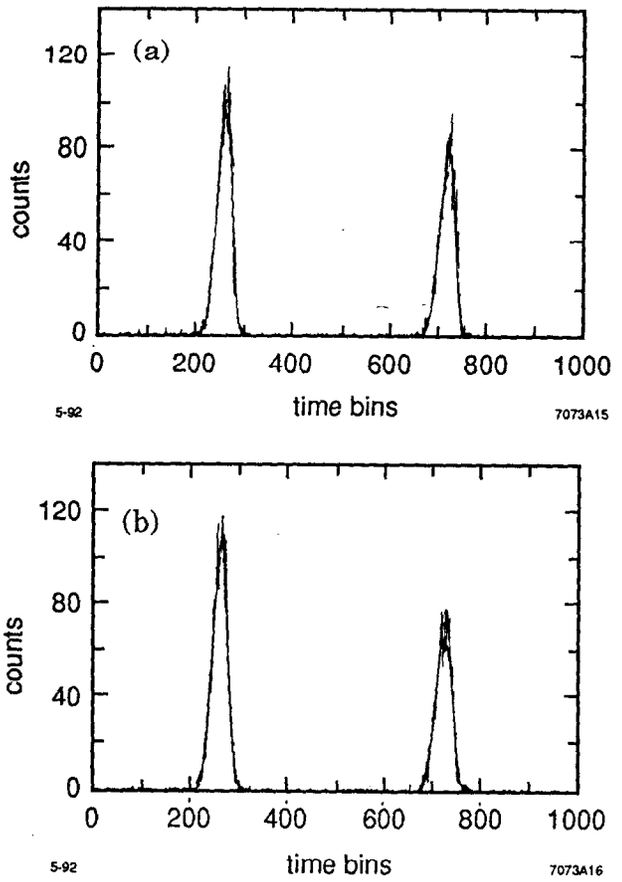

Figure B–10 Drift time spectra recorded on the qVt. Each LeCroy time bin is equivalent to 0.0187 μs. These plots are with different amounts of oxygen in the gas: (a) 0.2 ppm, and (b) 3.4 ppm. The ratio of the areas under the later to earlier peak is 0.80 and 0.70, respectively.

modified to increase the maximum time scale to about 18 μs. The signal from the sense wire of the drift cell was fed through a preamplifier, a 10X amplifier, a discriminator and finally into the stop input of the qVt. Both discriminators were set quite low to minimize the effect from time slewing due to the pulse heights. The qVt was read out via CAMAC to a VAX computer using a LeCroy Model 2301 CAMAC Interface.

Typical time distributions are shown in Figure B–10. The time spectrum is fit with a 8-parameter double Gaussian plus linear background function. The fit Gaussian means are used to determine the drift velocity. Comparing these spectra, recorded with different levels of oxygen in the gas, illustrate how the DVM is sensitive to the electron lifetime of the gas by looking at the ratio of the area in the

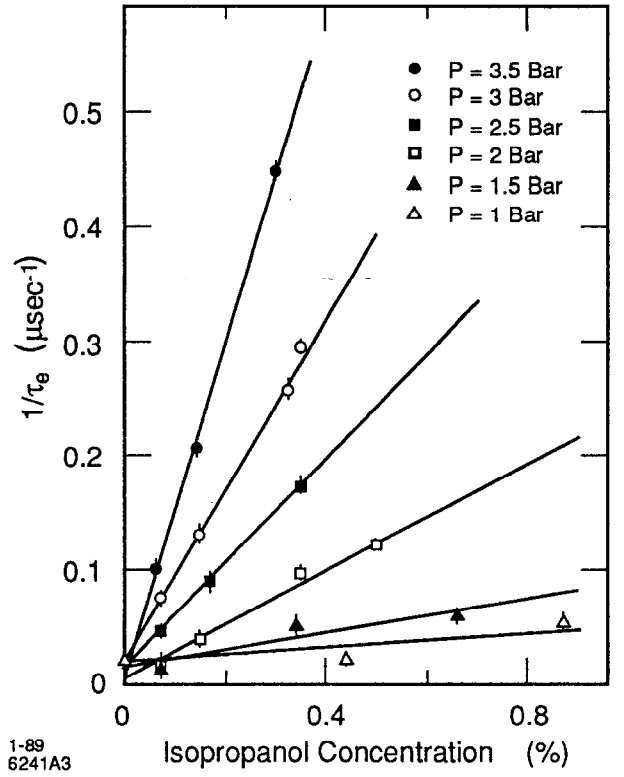

Figure B–11 The electron lifetime in the nominal CO_2/C_2H_6 gas with a small admixture of isopropanol.

earlier and later peaks. Note that the ^{106}Ru sources were not necessarily the same strength, so this also was taken into account, which can be done, for instance, by exchanging the positions of the two sources.

The electron lifetimes in the gas were measured by the DVM for the nominal CO_2/C_2H_6 gas mixture with different amounts of isopropanol, a common proportional chamber gas additive which has the effect increasing the radiation tolerance of a gas, as discussed in the following section. The isopropanol was mixed into the gas using a bubbler which was held at a constant temperature to control the isopropanol vapor pressure. The resulting electron lifetimes are shown in Figure B–11. With a drift velocity of about 5.7 mm/μs and a maximum drift length of about 50 mm in the DCVD, the maximum drift time is about 9 μs. Thus an electron lifetime of 30 μs corresponds to a 25% loss in pulse height, and at an operating pressure of 2 atm this limits the amount of isopropanol which should be used to less than ~0.1%.

The electron lifetime was also measured as a function of the oxygen level in the gas. This was done simply by using gas bottles supplied by the commercial gas

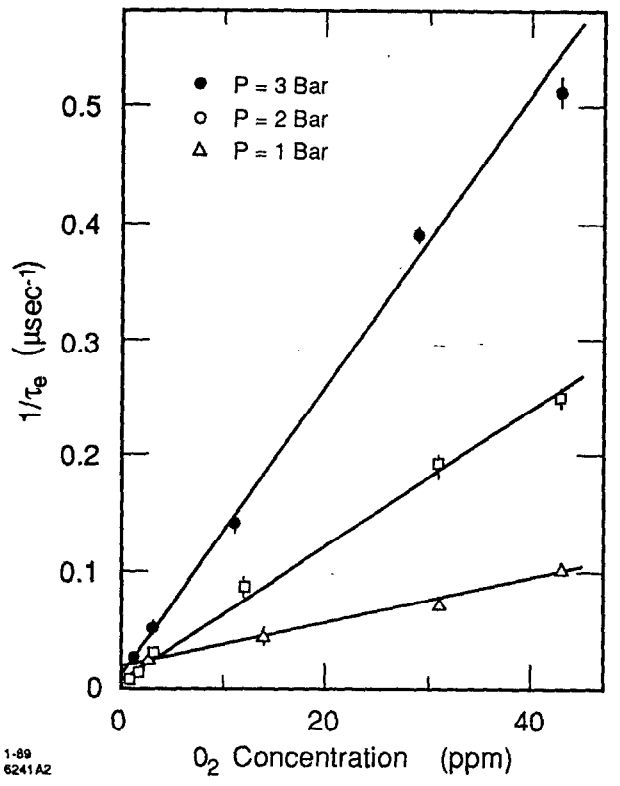

Figure B–12 Electron lifetimes as a function of the oxygen concentration in the standard CO_2/C_2H_6 gas mixture.

vendor which (unintentionally) had high levels of oxygen present. The gas sources were as high as 35 ppm of O_2. The electron lifetimes as a function of the oxygen concentration are shown in Figure B–12 and demonstrate that a very low oxygen level is required to produce reasonable electron lifetimes. These levels were routinely achievable in the actual system by keeping the system very leak-tight and by the use of Oxisorb to remove virtually all of the oxygen from the gas just prior to sending it into the chamber (see Section B.2.3). It is also interesting to note that these measurements of the electron lifetime confirm that the process of electron attachment is a three-body process, namely

$$O_2 + X + e^- \rightarrow O_2^- + X + \text{energy}.$$

In Reference [142] it is shown that the electron attachment frequency, $\nu_a = 1/\tau_e$, is given for a 2-body process ($O_2 + e^- \rightarrow O_2^- + \text{energy}$) by:

$$\nu_a = k_2 [O_2] \text{ (2-body)},$$

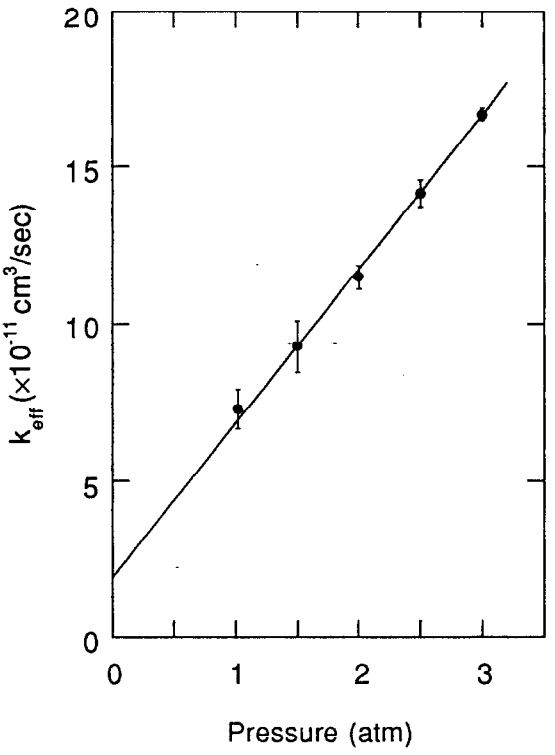

Figure B–13 k_{eff} as a function of the pressure of the CO_2/C_2H_6 mixture, demonstrating that the electron attachment process in this gas is a 3-body process.

where $[O_2]$ is the oxygen concentration and k_2 is the 2-body coefficient. For a 3-body process, the relation becomes,

$$\nu_a = k_3 [O_2] [X] \text{ (3-body)},$$

where [X] is the concentration of the other component in the gas (in our case CO_2), and k_3 is the coefficient for this process. If one forms the quantity

$$k_{eff} = \nu_a / [O_2] = 1/\tau_e [O_2],$$

then as a function of the concentration or pressure of the main component of the gas, k_{eff} can distinguish between the 2 and 3-body processes. A two body process will not exhibit any pressure dependence (since $k_{eff} = k_2$), whereas a three body process will have a linear dependence (because $k_{eff} = k_3 [X]$). The result, shown in Figure B–13, clearly demonstrates the three body nature of the interaction in our gas mixture.

The drift velocity dependence on temperature was also investigated using the DVM. The pressure chamber for the DVM had the same type of 0.25 inch tubing

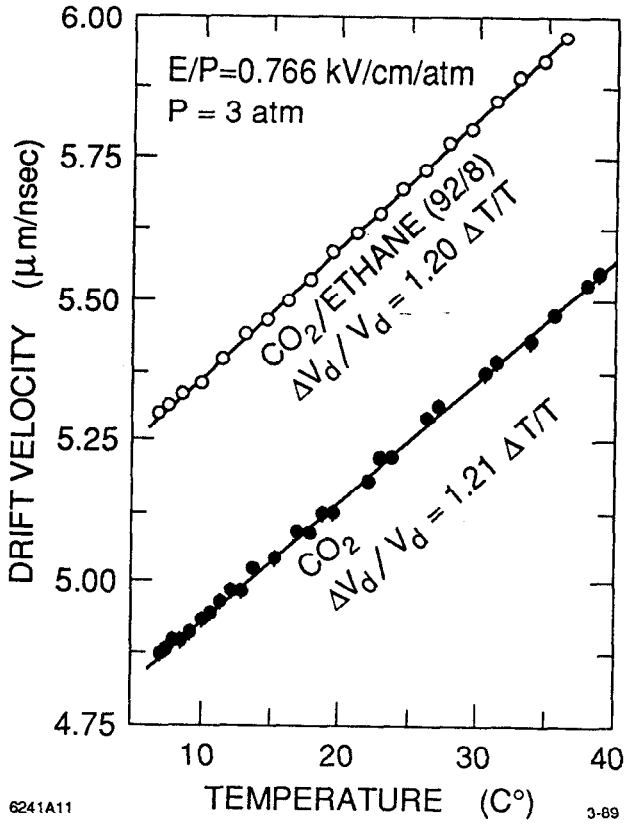

Figure B–14 The drift velocity dependence on temperature for CO_2/C_2H_6 and pure CO_2.

wound around it, as did the outer shell of the DCVD (see Figure B–3), which allowed active temperature control of the DVM. Using a prototype version of the temperature control routines used in the DCVD, the DVM was stepped through a range of temperatures, pausing to measure and read out the drift velocity through the CAMAC interface to the qVt module. The results are shown in Figure B–14. The temperature dependence of the drift velocity was characterized phenomenologically by $v_d \propto T^{\alpha}$. The dependence appears to be slightly stronger than a linear dependence, with a value of α which is about 1.2 for the CO_2/C_2H_6 gas mixture and for a pure CO_2 sample.

B.4.2 Radiation Test Chamber

Radiation damage to wire chambers has received a substantial amount of study, but this is still an imprecise science at best. Nonetheless, there are many ideas about the various mechanisms which contribute to the radiation damage.[143] Carbon dioxide and most nobel gases require the use of a gas additive (*quencher*) to absorb the copious number of photons emitted during the electron avalanche at the

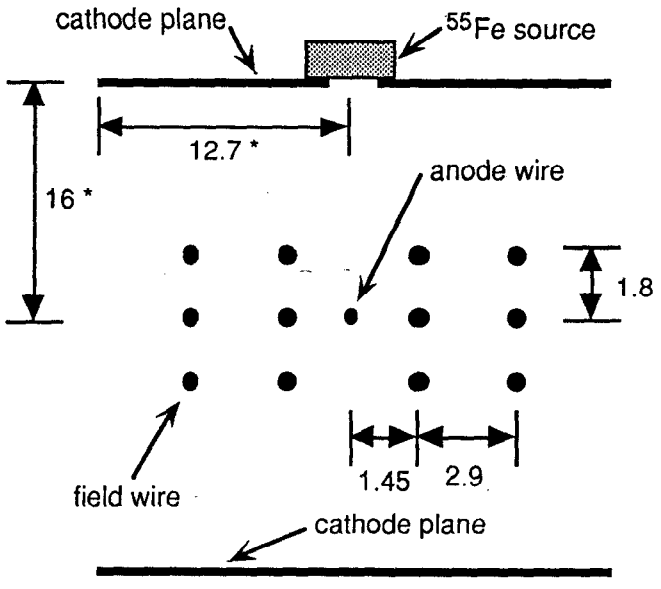

Figure B–15 Radiation Test Chamber cell design.

anode. Typically, organic gases such as ethane or isobutane, have been used. Without these quenchers, the photons tend to produce effects such as photoemission of electrons from the cathode. During the avalanche process, these quencher molecules can be dissociated into radical molecules which typically have a large dipole moment and are thus attracted toward the anode surface. These radicals can then polymerize and form deposits on the electrodes. In later avalanches, these polymers can receive a positive charge and drift toward the cathode. On the anode, these deposits can appear as gain loss, whereas on the cathode these can lead to the production of dark current (Malter Effect). One way to reduce this polymerization is to add a non-polymerizing gas, such as an alcohol, with a lower ionization potential. A very efficient charge transfer mechanism will cause the alcohol to neutralize the polymerizable molecules, thus reducing the organic deposits.

A very simple test cell was built to study the radiation damage for various gases and gas mixtures.[144] The cell design used in the last series of tests is shown in Figure B–15. To irradiate the cell, a ^{55}Fe source (either 300 or 1000 μCi) was used to provide 0.59 keV x-rays from the electron capture process. The gain in the cell was measured by the output voltage from the anode wire, after an RC integrating circuit. The gain as a function of the radiation exposure is illustrated in

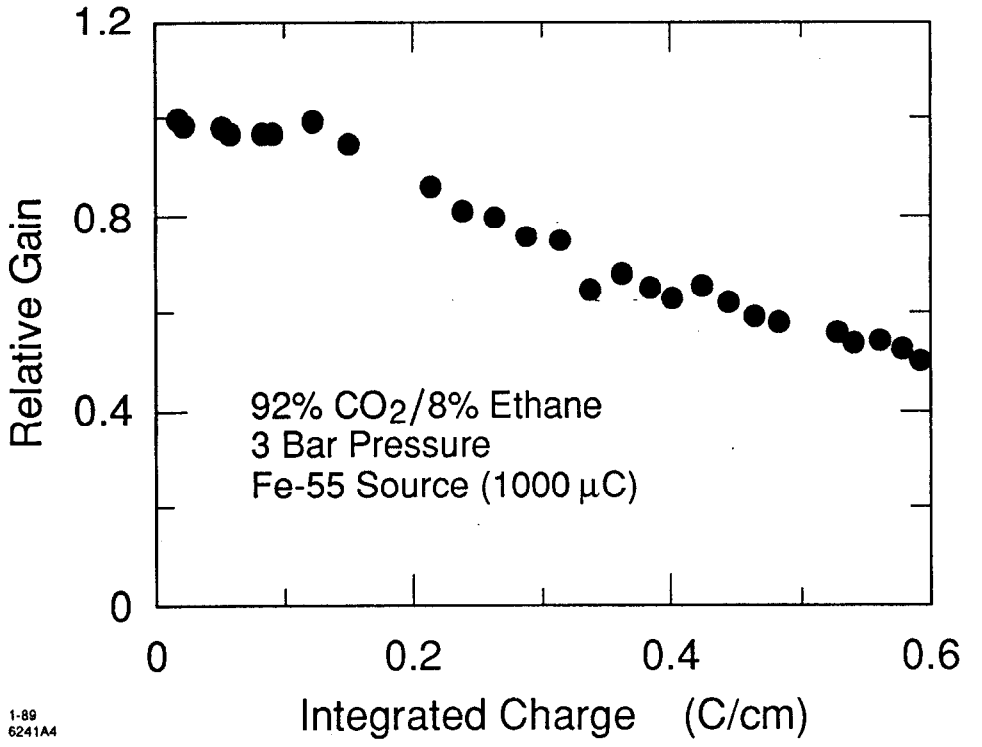

Figure B–16 Relative gain as a function of the total integrated charge for the nominal CO_2/C_2H_6 gas mixture.

Figure B–16 for the standard 92%/8% CO_2/C_2H_6 gas mixture. The summary of the tests on several gas mixtures are given below.

1. 92%/8% CO_2/iso-C_4H_{10}: The observed gain loss was minimal (similar to the CO_2/C_2H_6) except that very high current draw began and the test had to be terminated after about 0.2 C/cm of integrated charge. A possible explanation for this behavior is the Malter Effect, whereby an insulating material builds up on a field or cathode wires. After some irradiation this layer becomes charged and tends to emit electrons spontaneously. A potential cause of the low lifetime with this gas is that the gas used was not of the highest quality, and consequently could have contained impurities which were responsible for the development of the Malter Effect symptoms.
2. 92%/8% CO_2/C_2H_6: The radiation tolerance with this gas mixture was observed to be quite good. The gain was reduced only to about half after an integrated charge of 0.6 C/cm and no excess current draw developed. Upon the conclusion of the test, the anode wire was analyzed using x-ray spectroscopy and the deposits were found to contain silicon. The potential sources of this silicon include the G-10 wire frame, and to this

end a cell was made using Macor. This cell, however, repeatedly suffered premature high current draw and was never operated beyond 0.15 C/cm during which it behaved similar to the previous tests.

3. 92%/8% CO_2/C_2H_6 + 0.1% isopropanol: The addition of some alcohol was done in the hope of improving the tolerance to radiation. No difference was discernible from the CO_2/C_2H_6 test. Of course if the deposits on the anode which cause the gain loss are due to silicon impurities from components in the cell, it is unlikely that the alcohol would have any affect.

4. 50%/50% Ar/C_2H_6: This gas was observed to have a poor radiation lifetime in our tests, with the gain being reduced by half before an integrated charge of 0.15 C/cm. It has been suggested that our results were the consequence of using gas of insufficient purity, because other tests have observed much better lifetimes.[145] The purity in our gas was not known. Another possibility is that Ar/C_2H_6 gas mixtures perform better in chambers without grid or cathode wires, but rather only cathode surfaces, such as a straw chamber.[146] This is the case because the lack of grid and cathode wires would make the chamber much less susceptible to the development of Malter Effect problems.

B.5 Summary

This appendix has described the systems used to very accurately control the environmental conditions in the DCVD during its operation. With only sporadic exceptions due to various malfunctions, these systems performed adequately, maintaining a pressure stability of better than 0.01 psi and temperature stability of 0.02° C. The temperature differences inside the chamber were 0.12° C from end to end and 0.5° C from the inner to outer shells.

Some studies done on the properties of the 92%/8% $C0_2/C_2H_6$ gas mixture, as well as some related gas mixtures, were also presented. These studies measured the sensitivity of the electron lifetime to the presence of isopropanol and oxygen, the temperature dependence of the drift velocity and the radiation tolerance of the gas.

References

Chapter 1

[1] F. Close, Michael Marten and Christine Sutton, *The Particle Explosion*, Oxford University Press (1987);
J. E. Dodd, *The Ideas of Particle Physics*, Cambridge University Press, Cambridge (1984);
D. H. Perkins, *Introduction to High Energy Physics*, Addison-Wesley, Menlo Park, California (1987);
F. Halzen and A. D. Martin, *Quarks and Leptons: An Introductory Course in Modern Particle Physics*, John Wiley & Sons, New York, 1984.

[2] S. L. Glashow, "Partial-Symmetries of Weak Interactions", *Nucl. Phys.* **22** (1961) 579;
A. Salam and J. C. Ward, "Electromagnetic and Weak Interactions", *Phys. Lett.* **13** (1964) 168;
A. Weinberg, "A Model of Leptons", *Phys. Rev. Lett.* **19** (1967) 1264.

[3] G. Arnison *et al.* (UA1 Collaboration), "Experimental Observation of Isolated Large Transverse Energy Electrons with Associated Missing Energy at $\sqrt{s}$ = 540 GeV", *Phys. Lett.* **B122** (1983) 103;
M. Banner *et al.* (UA2 Collaboration), "Observation of Single Isolated Electrons of High Transverse Momentum in Events with Missing Transverse Energy at the CERN $p\bar{p}$ Collider", *Phys. Lett.* **B122** (1983) 476;

G. Arnison *et al.* (UA1 Collaboration), "Experimental Observation of Lepton Pairs of Invariant Mass around 95 GeV/c^2 at the CERN SPS Collider", *Phys. Lett.* **B126** (1983) 398;
M. Banner *et al.* (UA2 Collaboration), "Evidence for $Z^0 \to e^+e^-$ at the CERN $p\bar{p}$ Collider", *Phys. Lett.* **B129** (1983) 130.

[4] S. Schael, "Measurements of $\sin^2\theta_W$ from the Charge Asymmetry of Hadronic Events at the Z^0 Peak", Talk presented at the Lepton Photon Symposium, Geneva, Switzerland, 1991, IEKP-KA/91-12.

[5] M. Kobayashi and T. Maskawa, "CP Violation in the Renormalizable Theory of Weak Interaction", *Progress of Theoretical Physics* **49** (1973) 652.

[6] J. F. Kral, "Measurement of the Z-Boson Branching Fraction into Hadrons Containing Bottom Quarks", LBL-29485, Ph.D. Thesis (1990).

[7] J. Schwinger, *Particles and Fields, Volume II*, Addison-Wesley, New York (1973);
J. Jersak, E. Laermann and P. M. Zervas, "QCD Corrected Forward-Backward Asymmetry of Quark Jets in e^+e^- Annihilation", *Phys. Lett.* **B98** (1981) 363;
T. H. Chang, K. J. F. Gaemers and W. L. van Neerven, "QCD Corrections to the Mass of the Intermediate Vector Bosons", *Nucl. Phys.* **B202** (1982) 407.

[8] J. J. Hernandez *et al.* (The Particle Data Group), "Review of Particle Properties", *Phys. Lett.* **B239** (1990) 1.

[9] B. A. Kniehl and J. H. Kühn, "QCD Corrections to the Axial Part of the Z Decay Rate", *Phys. Lett.* **B224** (1989) 229;
M. Dine and J. Sapirstein, "Higher-Order Quantum Chromodynamic Corrections in e^+e^- Annihilation", *Phys. Rev. Lett.* **43** (1979) 668;
S. G. Gorishny, A. L. Kataev and S. A. Larin, "Next-Next-to-Leading $O(\bar{\alpha}_s^3)$ QCD Correction to $\sigma_{tot}(e^+e^- \to \text{hadrons})$: Analytical Calculation and Estimation of the Parameter $\Lambda_{\overline{MS}}$", *Phys. Lett.* **B212** (1988) 238;
B. A. Kniehl and J. H. Kühn, "QCD Corrections to the Z Decay Rate", *Nucl. Phys.* **B329** (1990) 547.

[10] W. J. Marciano and D. Wyler, "W-production via Z-decay", *Z. Phys.* **C3** (1979) 181;
D. Albert, W. J. Marciano, Z. Parsa and D. Wyler, "Decays of Intermediate Vector Bosons, Radiative Corrections and QCD Jets", *Nucl. Phys.* **B166** (1980) 460.

[11] D. C. Kennedy and B. W. Lynn, "Electroweak Radiative Corrections with an Effective lagrangian: Four Fermion Processes", *Nucl. Phys.* **B322** (1989) 1.

[12] W. Beenakker and W. Hollik, "The Width of the Z Boson", *Z. Phys.* **C40** (1988) 141.

[13] W. Hollik, "Radiative Corrections in the Standard Model and Their Role for Precision Tests of the Electroweak Theory", *Fortschr. Phys.* **38** (1990) 165–260.

[14] A. A. Akhundov, D. Yu. Bardin and T. Riemann, "Electroweak One-Loop Corrections to the Decay of the Neutral Vector Bosons", *Nucl. Phys.* **B276** (1986) 1.

[15] A. Djouadi *et al.*, "$b\bar{b}$-Production on the Z-Resonance: A Challenge to the Standard Model", *Nucl. Phys.* **B349** (1991) 48.

[16] M. Boulware and D, Finnell, "Radiative Corrections to $B\,(Z \to b\bar{b})$ in the Minimal Supersymmetric Standard Model", *Phys. Rev.* **D44** (1991) 2054.

[17] See, for example, B. Boudjema, F. M. Renard and C. Verzennassi, "A Selection Rule for Genuine New Physics in Combined High-Precision Measurement", *Nucl. Phys.* **B314** (1989) 301.

[18] C. Albajar *et al.* (UA1 Collaboration), "Studies of Intermediate Vector Boson Production and Decay in UA1 at the CERN Proton-Antiproton Collider", *Z. Phys.* **C44** (1989) 15;
R. Ansari *et al.* (UA2 Collaboration), "Search for Exotic Processes at the CERN $p\bar{p}$ Collider", *Phys. Lett.* **B195** (1987) 613;
T. A. Fuess (for the CDF Collaboration), "Search for W' and Z' at CDF", *Proc. of the Vancouver Meeting Particles and Fields '91*, Vancouver, B. C., Canada, August 18–22, 1991, p. 349.

[19] See, for example, M. C. Gonzalez-Garcia and J. W. F. Valle, "Constraints on Additional Z' Gauge Bosons from a Precise Measurement of the Z Mass", *Phys. Rev.* **D41** (1990) 2355.

[20] See, for example, B. W. LeClaire, "A Search for Supersymmetric Electrons with the Mark II Detector at PEP", SLAC-REPORT-321, Ph. D. Thesis October 1987; V. D. Barger and R. J. N. Phillips, Collider Physics, Addison-Wesley, Redwood City, California (1987).

[21] J. Carter (ALEPH, DELPHI L3 and OPAL Collaborations), in *Proc. EPS-High Energy Physics Conf. 91*, Geneva, July, 1991.

[22] D. Decamp *et al.* (The ALEPH Collaboration), "Heavy Flavor Production in Z Decays", *Phys. Lett.* **B244** (1990) 551.

[23] B. Adeva *et al.* (The L3 Collaboration), "Measurements of $Z^0 \to b\bar{b}$ Decays and the Semileptonic Branching Ratio $BR\,(b \to l + X)$", *Phys. Lett.* **B261** (1991) 177.

[24] M. Z. Akrawy *et al.* (The OPAL Collaboration), "A Study of heavy flavour production using Muons in Hadronic Z^0 Decays", *Phys. Lett.* **B263** (1991) 311.

[25] D. Decamp *et al.* (The ALEPH Collaboration), "Measurement of the B Hadron Lifetime", *Phys. Lett.* **B257** (1991) 492;
P. Abreu *et al.* (The DELPHI Collaboration), "Measurement of the Average Lifetime of B Hadrons", CERN-PPE/91-131, submitted to *Z. Phys.* **C**;
B. Adeva *et al.* (The L3 Collaboration), "Measurement of the Lifetime of B-Hadrons and a Determination of $|V_{cb}|$", L3 Preprint #32, *Phys. Lett.* **B270** (1991) 111.
P. D. Acton *et al.* (The OPAL Collaboration), "Measurement of the Average B Hadron Lifetime in Z^0 Decays", CERN-PPE/91-201, submitted to *Phys. Lett. B*;
G. Alexander *et al.* (The OPAL Collaboration), "Observation of the J/ψ Production in Multihadronic Z^0 Decays", *Phys. Lett. B*, **B226** (1991) 485.

[26] R. Fulton *et al.* (The CLEO Collaboration), "Observation of B-Meson Semileptonic Decays to Noncharmed Final States", *Phys. Rev. Lett.* **64** (1990) 16;
H. Albrecht *et al.* (The ARGUS Collaboration), "Reconstruction of Semileptonic $b \to u$ Decays", Phys. *Lett.* **B255** (1991) 297.

[27] J. F. Kral *et al.* (The Mark II Collaboration), "Measurement of the $b\bar{b}$ Fraction in Hadronic Z Decays", *Phys. Rev. Lett.* **64** (1990) 1211.

[28] W. Braunschweig *et al.* (The TASSO Collaboration), "Measurement of the Average Lifetime of B Hadrons", *Z. Phys.* **C44** (1989) 1.

[29] P. Abreu *et al.* (The DELPHI Collaboration), "A Measurement of the Partial Width of the Z^0 Boson to b Quark Pairs", CERN-PPE/90-118, *Phys. Lett.* **B252** (1990) 140.

[30] P. Weber, "Separated Vertex Search and Measurement of the B hadron Lifetime in e^+e^- Annihilation at $\sqrt{s}$ = 29 GeV", Ph. D. Thesis, University of Colorado, 1990.

[31] W. Braunschweig *et al.* (The TASSO Collaboration), "A Study of Jets from b Quarks Produced in e^+e^- Annihilations at $\sqrt{s}$ = 35 GeV", *Z. Phys.* **C42** (1989) 17.

[32] P. Henrard *et al.* (The ALEPH Collaboration), presented at the 4th Symposium on Heavy Flavour Physics, Orsay, June 1991;
P. Henrard *et al.* (The ALEPH Collaboration), presented at the Workshop on Neural Networks in High Energy Physics, Isola d'Elba, June 1991.

[33] C. De la Vaissiere and J. Palma-Lopez *et al.*, (The DELPHI Collaboration), CERN 89–5 PHYS 5 (Geneva 1989).

[34] C. Bortolotto, *et al.*, (The DELPHI Collaboration), presented at the Workshop on Neural Networks in High Energy Physics, Isola d'Elba, June 1991.

[35] B. Adeva *et al.* (The L3 Collaboration), "Measurement of Electroweak Parameters from Hadronic and Leptonic Decays of the Z^0", *Z. Phys.* **C51** (1991) 179.

[36] K. R. Schubert, in "Review of B-Meson Decay Results, 1989 International Symposium on Heavy Quark Physics", editors P. S. Drell and D. L. Rubin, AIP Conf. Prod., Vol. 196 (American Institute of Physics, New York, 1989) p. 79.

[37] P. C. Rowson *et al.*, (The Mark II Collaboration), "Charged Multiplicity of Hadronic Events Containing Heavy-Quark Jets", *Phys. Rev. Lett.* **54** (1985), 2580, and P. C. Rowson "Properties of Heavy Quark Jets Produced by e^+e^- Annihilation at 29 GeV", LBL-20463, Ph.D. Thesis, October 1985.

[38] A. V. Kisselev, V. A. Petrov and O. P. Yushchenko, "Average Charged Multiplicities in $Q\overline{Q}$ events $(Q = c, b, t)$ at LEP Energies", *Z. Phys.* **C41** (1988) 521.

[39] M. Sakuda *et al.*, (The DELCO Collaboration), "Properties of Bottom Quark Jets in e^+e^- Annihilation at 29 GeV", *Phys. Lett.* **B152** (1985) 339.

[40] H. Aihara *et al.*, (The TPC Collaboration), "Pion and Kaon Multiplicities in Heavy Quark Jets from e^+e^- Annihilation at 29 GeV", *Phys. Lett.* **B184** (1987) 299.

[41] W. Braunschweig, *et al.*, (The TASSO Collaboration), "A Study of Jets from b Quarks Produced in e^+e^- Annihilations at $\sqrt{s} = 35 - 46$ GeV", *Z. Phys.* **C42** (1989) 17.

[42] J. Chrin, "Upon the Determination of Heavy Quark Fragmentation Functions in e^+e^- Annihilation", *Z. Phys.* **C36** (1987) 163.

[43] C. Peterson, D. Schlatter, I. Schmitt and P. M. Zerwas, "Scaling Violations in Inclusive e^+e^- Annihilation Spectra", *Phys. Rev.* **D27** (1983) 105.

Chapter 2

[44] R. B. Neal (General Editor), "The Stanford Two-Mile Accelerator", W. A. Benjamin, Inc., New York, 1968.

[45] The Nobel Lectures in Physics for 1990 are good sources for information on the deep inelastic scattering experiments are:
R. E. Taylor, "Deep Inelastic Scattering: The Early Years", *Rev. Mod. Phys.* 63 (1991) 573;
H. W. Kendall, "Deep Inelastic Scattering: Experiments on the Proton and

Observation of Scaling", *Rev. Mod. Phys.* 63 (1991) 597;
J. I. Friedman, "Deep Inelastic Scattering: Comparisons with the Quark Model", *Rev. Mod. Phys.* 63 (1991) 615.

[46] J. E. Augustin *et al.*, (The Mark I Collaboration), "Discovery of a Narrow Resonance in e^+e^- Annihilation", *Phys. Rev. Lett.* **33** (1974) 1406.

[47] M. L. Perl *et al.*, (The Mark I Collaboration), "Evidence for Anomalous Lepton Production in $e^+ - e^-$ Annihilation", *Phys. Rev. Lett.* **35** (1975) 1489.

[48] John Rees, "The Stanford Linear Collider", Sci. Am. **261** no. 4 p. 8 (1989).
"SLAC Linear Collider Conceptual Design Report", SLAC Report No. 229, June 1990.

[49] B. Richter, "Very High Energy Electron-Positron Colliding Beams for the Study of Weak Interactions", *Nucl. Instr. and Meth.* **136**, 47 (1976).

[50] S. Hong *et al.*, internal Mark II memo (28 January 1991).

[51] G. Abrams, *et al.* (The Mark II Collaboration), "The Mark II detector for the SLC", *Nucl. Instr. and Meth.* **A281**, (1989) 55.

[52] G. Hanson, "The New Drift Chamber for the Mark II Detector at the SLAC Linear Collider", *Proc. of the Wire Chamber Conference*, Vienna, Austria, February 25-28, 1986.

[53] R. Fernow, "Introduction to Experimental Particle Physics", Cambridge University Press, Cambridge (1986);
W. R. Leo, "Techniques for Nuclear and Particle Physics Experiments", Springer-Verlag, Berlin (1987);
G. Charpack and F. Sauli, "High Resolution Electronic Particle Detectors", An. Rev. Nucl. Part. Sci. **34** (1984) 285.

[54] F. Sauli, "Principles and Operation of Multiwire Proportional and Drift Chambers", CERN 77-09 (1977).

[55] D. Briggs *et al.*, "The SLAC Mark II Upgrade Drift Chamber Front End Electronics", *IEEE Trans. on Nucl. Sci.*, **NS-32**, No. 1 (1985) 653.

[56] A. Peisert and F. Sauli, "Drift and Diffusion of Electrons in Gases: A Compilation", CERN 84-04, 13 July 1984; See Figure 63 for gas mixtures similar to HRS gas.

[57] D. Bernstein *et al.*, Proc. of Nucl. Sci. Symposium, San Francisco, 1985, SLAC-PUB-3806.

[58] H. Brafman *et al.*, "The SLAC Scanner Processor: A Fastbus Module for Data Collection and Processing", *IEEE Trans. on Nucl. Sci.*, **NS-32**, No. 1 (1985) 336.

[59] J. Perl *et al.*, "Track Finding with the Mark II/SLC Drift Chamber", *Nucl. Instr. and Meth.* **A252** (1986) 616.

[60] The definitive descriptions of the Mark II track fitting routines are:
A. D. Johnson and G. H. Trilling, "Orbit reconstruction Program for SPEAR Mark II Detector: ARCS", LBL Memo TG-301, September 15, 1978;
G. H. Trilling, "Tracking with PARC6, ADDTC, PARCV", LBL Memo TG-360, December 8, 1982.

[61] R. L. Gluckstern, "Uncertainties in track Momentum and Direction due to Multiple Scattering and Measurement Errors", *Nucl. Instr. and Meth.* **24** (1963) 381.

[62] K. F. O'Shaughnessy, "Properties of Hadronic Decays of the Z Boson", SLAC-360, Ph.D. Thesis, June 1990.

[63] R. J. Van Kooten, "Searches for New Quarks and Leptons in Z Boson Decays", SLAC-367, Ph.D. Thesis, June 1990.

[64] J. Alexander *et al.*, "Prototype results of a High Resolution Vertex Drift Chamber for the Mark II SLC Upgrade Detector", SLAC-PUB-3889, *Proc. of the Wire Chamber Conference*, Vienna, Austria, February 25–28, 1986.

[65] J. P. Alexander *et al.*, "The Mark II Vertex Drift Chamber", SLAC-PUB-4852, *Proc. of the Wire Chamber Conference*, Vienna, Austria, February 13–17, 1989.

[66] D. Durrett *et al.*, "Calibration and Performance of the Mark II Drift Chamber Vertex Detector", SLAC-PUB-5259, *Proc. of Vth International Conference on Instrumentation for Colliding Beam Physics*, Novosibirsk, USSR, March 15–21, 1990.

[67] L. Barker, "A FASTBUS Flash ADC System for the Mark II Vertex Chamber", SLAC-PUB-4757, Presented at the *Nuclear Science Symposium*, Orlando, Florida, November 9–11, 1988.

[68] The development and testing of the DCVD hit finding algorithms was done primarily by Bruce Schumm.

[69] The first stage of the track finding algorithm was developed by Don Fujino and added to the original track finder, now the second stage, developed by Bill Ford. For more information on the former algorithm, see Don Fujino's Ph.D. thesis, to be published as a SLAC Report.

[70] The detailed studies of the DCVD time-distance relation were done by Jim Smith and Bill Ford, and are discussed in detail in Reference [66].

[71] M. T. Elford, "The Drift Velocity of Electrons in Carbon Dioxide at 293° K", *Aust. J. Phys.* **19** (1966) 629;

R. A. Sierra, H. L. Brooks and K. J. Nygaard, "Electron Drift Velocities in N_2, CO_2 and N_2+CO_2) Laser Mixtures", *Appl. Phys. Lett.* **35** (1979) 764.

[72] C. Adolphsen *et al.*, "The Mark II Silicon Strip Vertex Detector", *Nucl. Instr. and Meth.* **A313** (1992) 63.

[73] R. G. Jacobsen, "A Measurement of the Branching Ratio of the Z Boson to Bottom Quarks Using Precision Tracking", Ph.D. Thesis, SLAC-Report-381, July 1991.

[74] J. Walker *et al.*, "Development of High Density Readout for Silicon Strip Detectors", *Nucl. Instr. and Meth.* **266** (1984) 200.

[75] M. Briendenbach *et al.*, "Semiautonomous Controller for Data Acquisition: The Brilliant ADC", SLAC-PUB-2032 and *IEEE Trans. Nucl. Sci.*, **NS-25**, No. 1 (1978) 706.

[76] A. Breakstone *et al.*, "Design of a Capactitive Displacement-Measuring System for Vertex Detectors at Colliding Beam Machines", *Nucl. Instr. and Meth.* **A 281** (1989) 453;
A. Breakstone, "Performance of the capactitive Displacement Measuring System of the Mark II Detector at the SLC", *Nucl. Instr. and Meth.* **A305** (1991) 39.

[77] C. Adolphsen *et al.*, "An Alignment Method for the Mark II Silicon Strip Vertex Detector Using an x-ray Beam", *Nucl. Instr. and Meth.* **A228** (1990) 257.

[78] C. Field *et al.*, "A Compact Beam Profile Probe Using Carbon Fibers", *Nucl. Instr. and Meth.* **A281** (1989) 453.

[79] J. Kent *et al.*, "Precision Measurements of the SLC Beam Energy", SLAC-PUB-4922, Presented at the *IEEE Particle Accelerator Conference*, Chicago, IL, March 20-23, 1989.

[80] R. Aleksan *et al.*, *Proceedings of the International Conference on the Impact of Digital Microelectronics and Microprocessors on Particle Physics*, World Scientific (1988) 38.

Chapter 3

[81] S. Komamiya *et al.* (The Mark II Collaboration), "Determination of α_s from a Differential-Jet-Multiplicity Distribution in e^+e^- Collisions at $\sqrt{s}$ = 29 and 91 GeV", *Phys. Rev. Lett.* **64** (1990) 987.

[82] A. Ali *et al.*, "QCD Predictions for Four-jet Final States in e^+e^- Annihilation", *Nucl. Phys.* **B167** (1980) 454;
K. Fabricius *et al.*, "Higher Order Perturbative QCD Calculation of Jet Cross Sections in e^+e^- Annihilation", *Z. Phys.* **C11** (1982) 315.

[83] T. Sjöstrand, "Status of Fragmentation Models", *Int. J. of Mod. Phys.* **A 3** (1988) 751;
T. Sjöstrand, "QCD Generators", CERN 89-08 Vol. 3, 21 September 1989 (the final report of the Workshop on Z Physics at LEP);
B. Foster, "Electron-Positron Annihilation Physics", Adam Hilger, Bristol, England (1990).

[84] T. Sjöstrand, *"The Lund Monte Carlo for Jet Fragmentation in e^+e^- Physics – JETSET Version 6.2", Comput. Phys. Commum.* **39** (1986) 347;
T. Sjöstrand and M. Bengtsson, *"The Lund Monte Carlo for Jet Fragmentation in e^+e^- Physics – JETSET Version 6.3 – An Update", Comput. Phys. Commum.* **43** (1987) 367.

[85] M. Bengtsson and T. Sjöstrand, "A Comparative Study of Coherent and Non-coherent Parton Shower Evolution", *Nucl. Phys.* **B289** (1987) 810.

[86] M. Bengtsson and T. Sjöstrand, "Coherent Parton Showers Versus Matrix Elements – Implications of PETRA / PEP Data" *Phys. Lett.* **B185** (1987) 435.

[87] G. Altarelli and G. Parisi, "Asymptotic Freedom in Parton language", *Nucl. Phys.* **B 126** (1977) 298.

[88] B. Andersson *et al.*, "Parton Fragmentation and String Dynamics", *Phys. Rep.* **97** (1983) 31.

[89] B. Andersson *et al.*, "A Model for Baryon Production in Quark and Gluon Jets", *Nucl. Phys.* **B197** (1982) 45.

[90] B. Andersson *et al.*, "Baryon Production in Jet Fragmenation and Υ-Decay", *Phys. Scripta* **32** (1985) 574.

[91] B. Andersson *et al.*, "A General Model for Jet Fragmentation", *Z. Phys.* **C20** (1983) 317.

[92] M. Suzuki, "Fragmentation of Hadrons from Heavy Quark Partons", *Phys. Lett.* **B71** (1977) 139;
J. D. Bjorken, "Properties of Hadron Distributions in Reactions Containing Very heavy Quarks", *Phys. Rev.* **D17** (1978) 171.

[93] S. Bethke, "Experimental Studies on the Heavy Quark Fragmentation Functions", *Z. Phys.* **C29** (1985) 175.

[94] D. Decamp *et al.* (The ALEPH Collaboration), "Production and Decay of Charmed Mesons at the Z Resonance", *Phys. Lett.* **B266** (1991) 218.

[95] G. Alexander *et al.* (The OPAL Collaboration), "A Study of $D^{*\pm}$ -Production in Z^0 Decays", *Phys. Lett.* **B262** (1991) 341.

[96] C. Peterson *et al.*, "Scaling Violations in Inclusive e^+e^- Annihilation Spectra", *Phys. Rev.* **D27** (1983) 105.

[97] A. Petersen *et al.* (The Mark II Collaboration), "Multihadronic Events at $E_{c.m.}$ = 29 GeV and Predictions of QCD Model from $E_{c.m.}$ = 29 GeV to $E_{c.m.}$ = 93 GeV", *Phys. Rev.* **D37** (1988) 1.

[98] G. S. Abrams *et al.* (The Mark II Collaboration), "Measurement of Charged-Particle Inclusive Distributions in Hadronic Decays of the Z Boson", *Phys. Rev. Lett.* **64** (1990) 1334.

[99] G. Marchesini and B. R. Webber, "Simulation of QCD Jets Including Soft Gluon Interference", *Nucl. Phys.* **B238** (1984) 1.
B. R. Webber, "A QCD Model for Jet Fragmentation Including Soft Gluon Interference", *Nucl. Phys.* **B238** (1984) 492.

[100] T. D. Gottschalk and D. A. Morris, "A New Model for Hadronization and e^+e^- Annihilation", *Nucl. Phys.* **B288** (1987) 729.

[101] W. Bartel *et al.*, (JADE Collaboration), "Experimental Studies on Multijet Production in e^+e^- Annihilation at PETRA Energies", *Z. Phys* **C33**, 23 (1986); S. Bethke, Habilitationschrift, University of Heidelberg (1987) (unpublished).

[102] M. Z. Akrawy *et al.* (The OPAL Collaboration), "A Measurement of Global Event Shape Distributions in the Hadronic Decays of the Z^0", *Z. Phys.* **C47** (1990) 505.

[103] See p. III.14 of Reference [8] for information of multiple scattering.

[104] G. Molière, *Z. Naturforschung* **2a** (1947) 133; **3a** (1948) 78;
H. A. Bethe, "Molière's Theory of Multiple Scattering", *Phys. Rev.* **89** (1953) 1256;
W. T. Scott, "The Theory of Small-Angle Multiple Scattering of Fast Charged Particles", *Rev. Mod. Phys.* **35** (1963) 231;
J. B. Marion and B. A. Zimmernam, "Multiple Scattering of Charged Particles", *Nuc. Instr. and Meth.* **51** (1967) 93.

[105] T. Lindelof, editor. "CERN Program Library", 1987 .03.01, page 6.537.

Chapter 4

[106] E. Fahri, "Quantum Chromodynamics Tests for Jets", *Phys. Rev. Lett.*, **39** (1977) 1587.

[107] T. Sjöstrand, "The Lund Monte Carlo for e^+e^- Jet Physics", *Comput. Phys. Commum.* **28** (1983) 227.

[108] B. Rossi and K. Greisen, "Cosmic Ray Physics", *Rev. Mod. Phys.* **13** (1941) 240.

[109] V. L. Highland, "Some Practical Remarks on Multiple Scattering", *Nuc. Instr. and Meth.* **129** (1975), 497.

[110] G. R. Lynch and O. I. Dahl, "Approximations to Multiple Coulomb Scattering", LBL-28165-Rev (November 1990).

[111] R. K. Bock *et al.* (editors) "Formulae and Methods in Experimental Data Evaluation with Emphasis in High Energy Physics", published by the European Physical Society, Volume 1, page 136 (January 1984).

[112] The development of the interaction point finding algorithm used in this analysis and the study of the interaction point motion in the data was done by Steve Wagner.

[113] G. S. Abrams *et al.* (The Mark II Collaboration), "Measurements of Charged-Particle Inclusive Distributions in Hadronic Decays of the Z^0", *Phys. Rev. Lett.* **64** (1990) 1334.

[114] D. Decamp *et al.* (The ALEPH Collaboration), "Measurement of the Charged Particle Multiplicity Distribution in Hadronic Z Decays", CERN-PPE/91-159.

[115] P. D. Acton *et al.* (The OPAL Collaboration), "A Study of Charged Particle Multiplicities in Hadronic Decays of the Z^0", CERN-PPE/91-176.

[116] P. Abreu *et al.* (The DELPHI Collaboration), "Charged Particle Multiplicity Distributions in Z^0 Hadronic Decays", *Z. Phys.* **C50** (1991) 185.

[117] B. Adeva *et al.* (The L3 Collaboration), "Measurement of the Inclusive Production of Neutral Pions and Charged Particles on the Z^0 resonance", *Phys. Lett.* **B259** (1991) 199.

Chapter 5

[118] The fine-point was brought to my attention by Morris Swartz.

[119] R. Fulton *et al.* (The CLEO Collaboration), "Observation of B-Meson Semileptonic Decays to Noncharmed Final States", *Phys. Rev. Lett.* **64** (1990) 16;
H. Albrecht *et al.* (The ARGUS Collaboration), "Observation of Semileptonic Charmless B Meson Decays", *Phys. Lett.* **234** (1990) 409;
H. Albrecht *et al.* (The ARGUS Collaboration), "Reconstruction of Semileptonic $b \rightarrow u$ Decays", *Phys. Lett.* **255** (1991) 297.

[120] K. Hayes, "B Tagging at the SLC", Mark II/SLC Note #73, May 8, 1984.

[121] B. A. Schumm, "High Precision Tracking and the Measurement of $B(Z \rightarrow b\bar{b})/B(Z \rightarrow hadrons)$ with the Mark II at the SLC", LBL-30709, to be published in the proceedings of the 26th Recontre de Moriond, Les Arcs, France, March 10-17, 1991.

Chapter 6

[122] The LEP Collaborations (ALEPH, DELPHI, L3 and OPAL), "Electroweak Parameters of the Z^0 Resonance and the Standard Model", *Phys. Lett.* **B276** (1992) 247.

[123] A. Bean, *et al.* (The CLEO Collaboration), "Limits on $B\overline{B}$ Mixing and τ_{B^0}/τ_{B^+}", *Phys. Rev. Lett.* **58** (1987) 183.

[124] H. Albrecht *et al.*, (The ARGUS Collaboration), "A Measurement of $\tau(B^+)/\tau(B^0)$ from Lepton and Dilepton Rates in $\Upsilon(4s)$ Decay", DESY 91-056, June 1991.

[125] S. Wagner *et al.* (The Mark II Collaboration), "Measurement of the B^0 Meson Lifetime", *Phys. Rev. Lett.* **64** (190) 1095.

[126] M. Danilov, "Heavy Flavour Physics (Non-LEP)", Talk presented at the Lepton Photon Symposium, Geneva, Switzerland, 1991.

[127] P. Roudeau, "Heavy Flavour Physics at LEP", LAL 91-49, November 1991 (presented at the Lepton Photon Symposium, Geneva, Switzerland, 1991).

[128] R. Morrison and M. Witherell, "D Mesons", UCSB-HEP-89-01, to appear in Annual Review of Nuclear and Particle Science, Volume #39.

[129] P. Abreu *et al.* (The DELPHI Collaboration), "Measurement of the Partial Width of the Decay of the Z^0 into Charm Quark Pairs", *Phys. Lett.* **B252** (1990) 140.

[130] B. Gittelman and S. Stone, "*B* Meson Decay", published in A. Ali and P. Söding (editors), "High Energy Electron Positron Physics", World Scientific Publishing Co., (1988) 273.

[131] H. Albrecht *et al.*, (The ARGUS Collaboration), "Measurement of R and Determination of the Charged Particle Multiplicity at $\sqrt{s}$ around 10 GeV", DESY-91-092, August 1991.

[132] M. S. Alam *et al.* (The CLEO Collaboration), "Charged Multiplicities in *B*-Meson Decay", *Phys. Rev. Lett.* **49** (1982) 357.

[133] M. S. Alam *et al.*, CLNS-81-513 (1981) 14;
P. Drell and D. Besson for the CLEO Collaboration, private communication.

[134] D. Bertoletto, *et al.* (The CLEO Collaboration), "Inclusive *B*-Meson Decays to Charm", *Phys. Rev.* **D35** (1987) 19.

[135] A full discussion of this nuclear scattering generator can be found in the Mark II/SLC Memo No. 268 by Bruce Schumm (9 July 1991).

Chapter 7

[136] M. Z. Akrawy *et al.*, "A study of Jet Production rates and a Test of QCD on the Z^0 Resonance", *Phys. Lett.* **B235** (1990) 389.

[137] See p. III.15 of Reference [102] for information on estimating the photon conversion cross section.

[138] C. Bacci *et al.* (The ADONE Collaboration), "Total Cross Section for Hadronic Production by e^+e^- Annihilation in the Total CM Energy range 1.42–3.09 GeV", *Phys. Lett.* **B 86** (1979) 234;
L. Siegrist *et al.* (The Mark I Collaboration), "Hadronic Production by e^+e^- Annihilation at Center-of-Mass Energies between 2.6 and 7.8 GeV. I. Total Cross Section, Multiplicities and Inclusive Momentum Distributions", *Phys. Rev.* **D26** (1982) 969;
B. Niczyporuk *et al.* (The LENA Collaboration), "Charged Hadron Production in e^+e^- Annihilation in the Υ and Υ' Region", *Z. Phys.* **C 9** (1981) 1;
M. S. Alam *et al.* (The CLEO Collaboration), "Charged-Particle Multiplicities in the B-Meson Decay", *Phys. Rev. Lett.* **49** (1982) 357;
Ch. Berger *et al.* (The PLUTO Collaboration), "Multiplicity Distribution in e^+e^- Annihilations at PETRA Energies", *Phys. Lett.* **B95** (1980) 313;
W. Bartel *et al.* (The JADE Collaboration), "Charged Particle and Neutral Kaon Production in e^+e^- Annihilations at PETRA", *Z. Phys.* **C20** (1983) 187;
M. Althoff *et al.* (The TASSO Collaboration), "Jet Production and Fragmentation in e^+e^- Annihilation at 12-43 GeV", *Z. Phys.* **C22** (1984) 307;
M. Derrick *et al.* (The HRS Collaboration), "Study of Quark Fragmentation in e^+e^- Annihilations at 29 GeV: Charged Multiplicity and Single Particle Rapidity Distributions", *Phys. Rev.* **D34** (1986) 3304;
H. Aihara *et al.* (The TPC Collaboration), "Charged Hadron Production in e^+e^- Annihilation at 29 GeV", *Phys. Rev. Lett.* **52** (1984) 577;
H. W. Zheng *et al.* (The AMY Collaboration), "Charged-Particle Multiplicities in e^+e^- Annihilations at $\sqrt{s}$ = 50-61,4 GeV", *Phys. Rev.* **D42** (1990) 737.

[139] For more information on the LLA-inspired form for the multiplicity dependence on center-of-mass energy, see for example,
A. H. Mueller, "On the Multiplicity of Hadrons in QCD Jets", *Phys. Lett.* **B104** (1981) 161; "Multiplicity and Hadron Distribution in QCD Jets, (II.) A General Procedure for all Non-leading Terms", *Nuc. Phys.* **B228** (1983) 351.

[140] The PEP and PETRA collaborations which have measured the total charged multiplicity measurements around 30 GeV are the Mark II (see Reference [97]) and PLUTO, JADE, TASSO and HRS (see Reference [138]).

Appendices

[141] For general information on $B\overline{B}$ mixing, see for example,
H. Schröder, "$B\overline{B}$ Mixing", DESY 91-139, November 1991. To be published in S. Stone (editor) "B Decays", World Scientific, Singapore;
I. I. Bigi, "B°-$\overline{B}^{\circ}$ Mixing – A Theoretical Evaluation After ARGUS", Proceedings of the Fifteenth SLAC Summer Institute, (SLAC Report 328), August 1987

[142] H. S. W. Massey, *Electronic and Ionic Impact Phenomena, Volume II*, Oxford University Press (1969), p. 1009.

[143] For example, see J. Kadyk (Workshop Organizer), *Proceedings of the Workshop on Radiation Damage to Wire Chambers*, LBL-21170, Lawrence Berkeley Laboratory, University of California, Berkeley, California, January 16-17, 1986; Two particularly good overviews contained the above proceedings are:
F. Sauli, "When Everything Was Clear", and
J. Va'vra, "Review of Wire Chamber Aging".

[144] These tests were initiated by P. Drell and carried on by S. Wagner, J. Smith and myself. Some of P. Drell's results are summarized in the workshop proceedings of Reference [143].

[145] J. Kadyk, personal communication.

[146] S. Wagner, personal communication.